

Bubble, Drop and Particle Unit (BDPU)

Oscillatory Thermocapillary Instability

Principal Investigator:

Dr. Jean-Claude Legros
Université Libre de Bruxelles
Brussels, Belgium

MICROGRAVITY RESEARCH CENTER

The Life and Microgravity SpaceLab Mission

Oscillatory Thermocapillary Instability

Overview of the Preliminary Results, August 1997

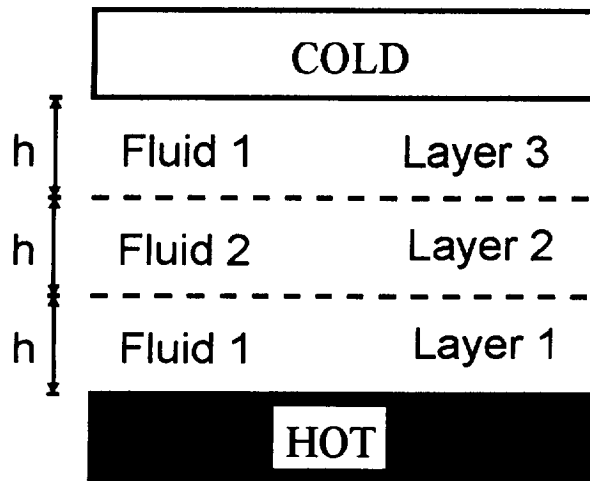
J.C. Legros and Ph. Georis

Service de Chimie Physique E.P., CP165
Université Libre de Bruxelles; 50 Av. F.D Roosevelt,
1050 Bruxelles, Belgium.

Objectives

Investigation of the behaviour of liquids bounded by free interfaces is of prime importance for containerless material processing in microgravity. Crystal growing and purification of high added value multi-component electronic crystal such as GaAs could be one day, an economically profitable space activity. Containerless boundaries around the melt reduce the problems of wall corrosion and contamination. Also eliminated are the structural stresses associated with the separation of the container from solidified material. However, the convection induced by surface tension gradients along the free surface of the melt remains a potential cause for structural and concentrational inhomogeneities as it can induce time dependent flow. The float zone refining method is a containerless technique used on ground for many years to produce high quality silicon crystals for electronic industry. For a high density material such as GaAs, ground based processing is restricted to small crystal since the stabilising effect of the surface tension forces is small with respect to the gravity effect. In microgravity, the maximum diameter of the crystal is much larger and effectively limited by the electrical power needed to melt the sample.

The liquid crystal encapsulation of the GaAs by B_2O_3 has been suggested as an improved method for single crystal processing. The encapsulation of the melt reduces the evaporation of As and helps thus to control the stoichiometry of the GaAs single crystal processed. Moreover, the encapsulant is expected to reduce the intensity of Marangoni convection and also to suppress time dependent flow. This promising idea has recently motivated theoretical and experimental investigations on thermocapillary convection in superposed layers of immiscible liquids. The model case where the temperature gradient is applied perpendicularly to the free interfaces as in the central zone of the melted region of a sample, has been examined on the LMS mission.



The configuration depicted here is a natural extension of the Marangoni Bénard instability studied on ground for about 100 years. However the mechanism leading to the Marangoni-Bénard instability is very different when both phases adjacent to the interface are taken into account. In the single layer case, the instability results from the competition between dissipation (viscous and thermal) and surface tension forces generated along the free surface by the fluctuations.

When both layers are taken into account, convective motions in the cold layer ($d\sigma/dT < 0$) are stabilising because they are damping thermal gradients at the interface.

In this case, the development of the instability will mainly depend on the relative efficiency of heat transfer towards the interface in both layers determined by the heat diffusivity of the liquid. The main consequence of this mechanism is the possibility of oscillatory convection at the threshold. For the symmetrical three layer system, the existence of the oscillatory mode is governed by one parameter: the heat diffusivity of the two liquids have to be close to each other. This criterion for the existence of time dependent flow is so simple that it could be relevant for many practical applications in space or on ground. This experiment aimed at proving the existence of this type of oscillatory mechanism in the configuration of the three layer system that was theoretically predicted so far.

This experiment on the LMS mission on oscillatory convection is a follow up of the IML2 mission where steady convection in a three layer system has been successfully investigated.

Experiment description

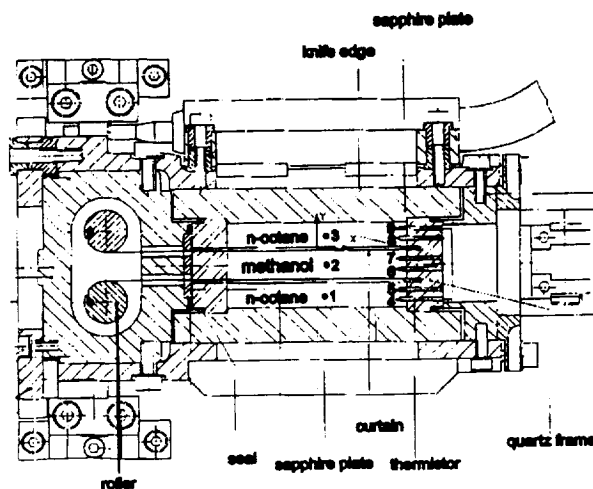
The fluids selected for this experiment are n-octane for the external layers (1&3) and methanol for the central one (2). These fluids are transparent, liquid at the ambient temperature, meet the safety requirements and form an interface insensitive to contamination where Marangoni convection can be easily observed. Methanol and n-octane are partially miscible and their miscibility is increasing with temperature. To reduce the mass transfer between the layers, the experiment is operated below the ambient temperature as far as possible. The properties of liquids are listed in table 1.

Table 1 : Fluid properties

	n-octane (1&3)	methanol (2)	(1)/(2)
ν ($\text{m}^2 \text{s}^{-1}$)	$7.0 \cdot 10^{-7}$	$8.0 \cdot 10^{-7}$	0.875
μ ($\text{kg m}^{-1} \text{s}^{-1}$)	$5.51 \cdot 10^{-4}$	$5.62 \cdot 10^{-4}$	0.98
λ ($\text{W m}^{-1} \text{K}^{-1}$)	$2.15 \cdot 10^{-1}$	$1.50 \cdot 10^{-1}$	1.43
κ ($\text{m}^2 \text{s}^{-1}$)	$1.09 \cdot 10^{-7}$	$1.02 \cdot 10^{-7}$	1.07
ρ (kg m^{-3})	703	787	0.897
Pr	6.42	7.84	0.82
$\sigma_{\text{n-oct. - meth}}$ (N m^{-1})	$4.0 \cdot 10^{-3}$		
$d\sigma_{\text{n-oct. - meth}}/dT$ ($\text{N m}^{-1} \text{K}^{-1}$)	$-1.9 \cdot 10^{-5}$		

The heat diffusivities of the liquids are nearly equals, the primary condition for the onset of the oscillatory instability is thus perfectly fulfilled. $d\sigma_{\text{meth - n-oct}}/dT$ has been measured in the laboratory using the maximum drop weight method described by Harkins (1952).

Fluid container

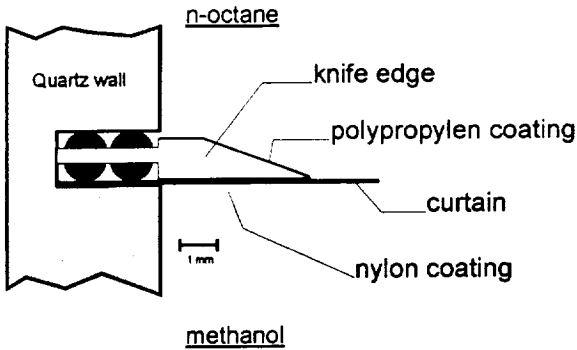


The fluid container is closed on two sides by one centimetre thick sapphire windows. The internal dimensions of the fluid container are 50 mm x 35 mm x 24 mm. Initially, the 8 mm high layers are separated by two stainless steel curtains preventing any mixing before the beginning of the experiment. The boundaries between the layers are maintained leak tight by Chemraz seals moulded on an antiwetting a knife edge. At the beginning of the experiment the curtains are pulled out and slowly wounded (0.25 mm s^{-1}) on rollers creating two free liquid - liquid interfaces subjected to the Marangoni effect. The temperature difference between the

sapphire is then increased step by step until the onset of convection is reached.

Stability of the three layer configuration

In microgravity, the static shapes of connected liquid phases are governed by the interfacial forces only. In the absence of walls, a three layer configuration such as depicted in fig. 1. would be unstable. Indeed, the surface tension forces would act to minimise the surface with respect to the volume of the layers, curving the free interfaces and leading supposedly to connected spherical phases. In a container, the situation is different because the layers may keep a flat shape provided their edges are properly anchored on the solid walls.



Here, the anchorage is achieved using two stainless steel frames coated on one side with a polypropylen film and with a nylon film on the other side (fig 3). Nylon is wetted preferentially by methanol rather than by n-octane while polypropylen is wetted by n-octane rather than by methanol.

Besides controlling the wetting of the walls, one must ensure that the experimental set up is such that the interfacial tension counterbalances the density difference of the

liquids effectively (this is important because of the residual gravity level in the space shuttle). This condition must be fulfilled taking into account that the liquid layers are enclosed in a fixed volume. In the simplified case of the Rayleigh-Taylor instability - the residual gravity is normal to the interfaces - the surface tension stabilises the arrangement for sufficiently short wavelengths.

The critical wavelength λ_m for the onset of the Rayleigh-Taylor instability for two liquids is given by the capillary length (Chandrasekhar 1961). The maximum gravity level acceptable \hat{g} is estimated to $10^{-2} g_0$ knowing that when λ_m is larger than the length of the interface, the Rayleigh-Taylor instability cannot start. In the space shuttle, the mean microgravity level being lower than $10^{-4} g_0$, the Rayleigh-Taylor instability mechanism will be inactive for the geometry chosen here and indeed has not been observed.

Theoretical and numerical approach

Linear stability analysis

The linear stability analysis is used to compute the critical Marangoni number (or ΔT) for the onset of convection. The linear stability analysis gives also the spatial and the temporal frequencies of the instability at the onset. The linear stability curve is shown on fig. 4; The validity of these results is restricted to system of infinite extension in the horizontal plane. Also, these results do not apply to the supercritical region where the non linear terms in the energy and in the Navier Stokes equations cannot be neglected. The non dimensional and dimensional values of the critical values are given in table 2. The period of the oscillation is about 5 min and is compatible with the time slice allocated to the experiment (20 hours).

Table 2 : Results of the linear stability analysis

Ma_c	k_c	w_c	ΔT_c	L_c (cm)	Period (s)
1625	1.96	1.53	1.65	2.57	328

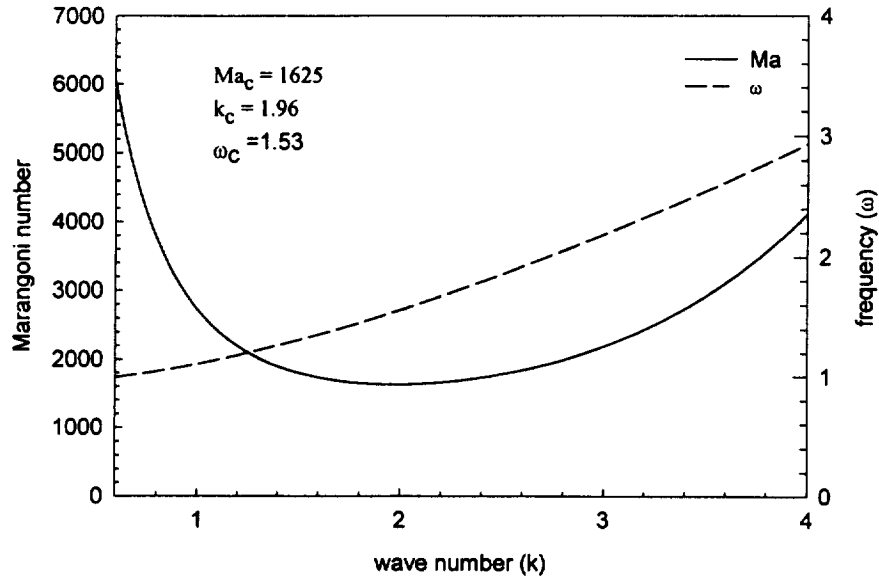


Fig. 4: linear stability analysis

The Marangoni is defined with respect to the parameters of the n-octane layer :

$$Ma = \frac{\frac{d\sigma}{dT} \Delta T h_1}{\kappa_1 \mu_1}$$

2D Finite difference simulations

The non-linear Navier Stokes and the energy equations are solved numerically in 2D for the actual set-up. In each layer l , the dimensionless governing equations expressed in terms of stream function and vorticity are:

$$\partial_t \phi + \partial_z \psi \partial_x \phi - \partial_z \phi \partial_x \psi = \frac{\nu_l}{\nu_1} \Delta^2 \phi$$

$$Pr (\partial_t T + \partial_z \psi \partial_x T - \partial_z T \partial_x \psi) = \frac{\kappa_l}{\kappa_1} \Delta^2 T$$

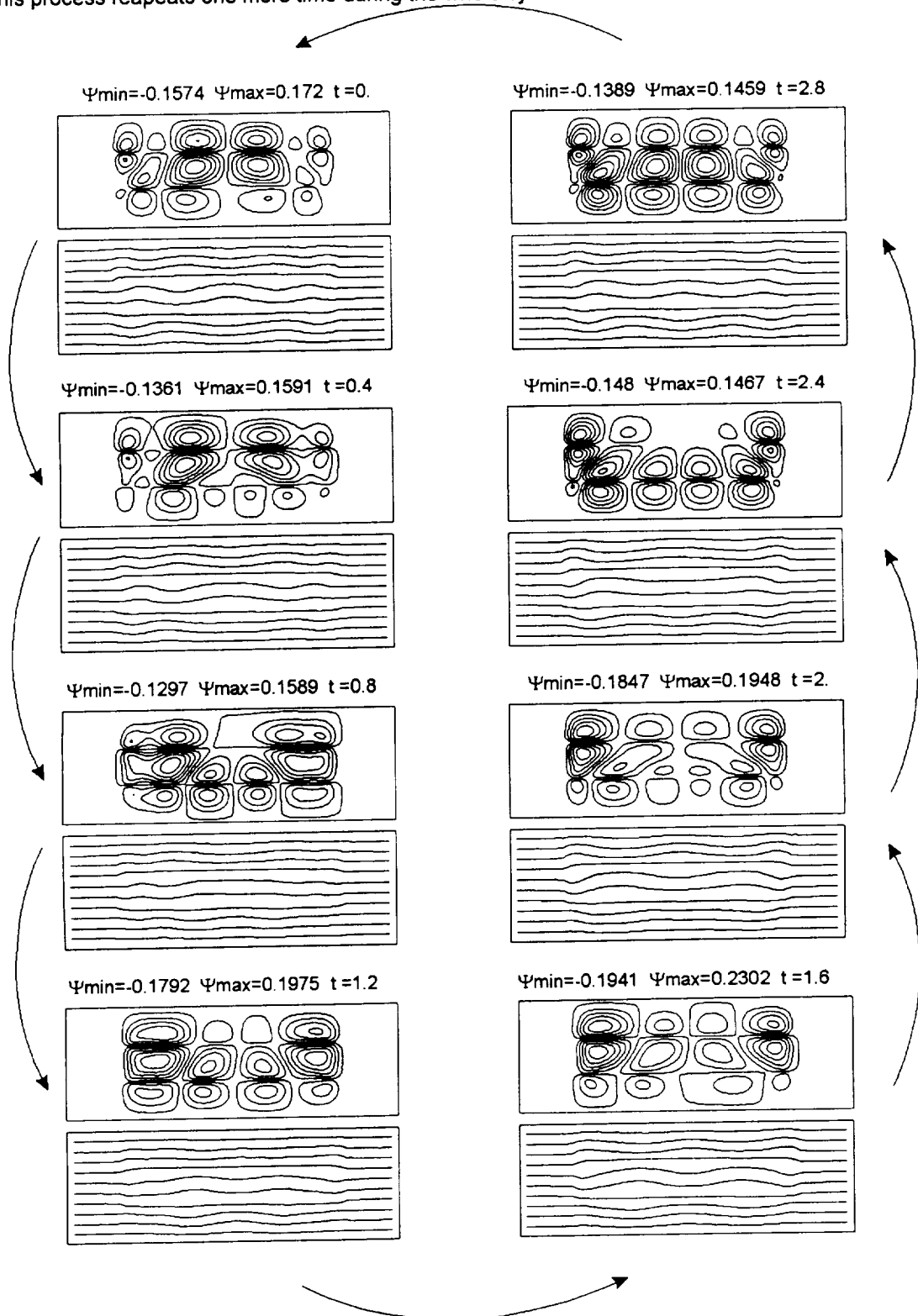
where: $\frac{\partial \psi}{\partial z} = v_x$ and $-\frac{\partial \psi}{\partial x} = v_z$, $\Delta^2 \psi = \phi$

with $Pr = \frac{\nu_1}{\kappa_1}$

The equations are discretised on a uniform rectangular mesh using the centred difference technique and solved using ADI scheme. The Poisson's equation is solved using the Gauss-Seidel relaxation technique. The Navier Stokes, energy and Poisson's equations are solved for the internal nodes in each layer independently then the boundary conditions are applied to compute the value of the vorticity and temperature on the boundary nodes.

Numerical results

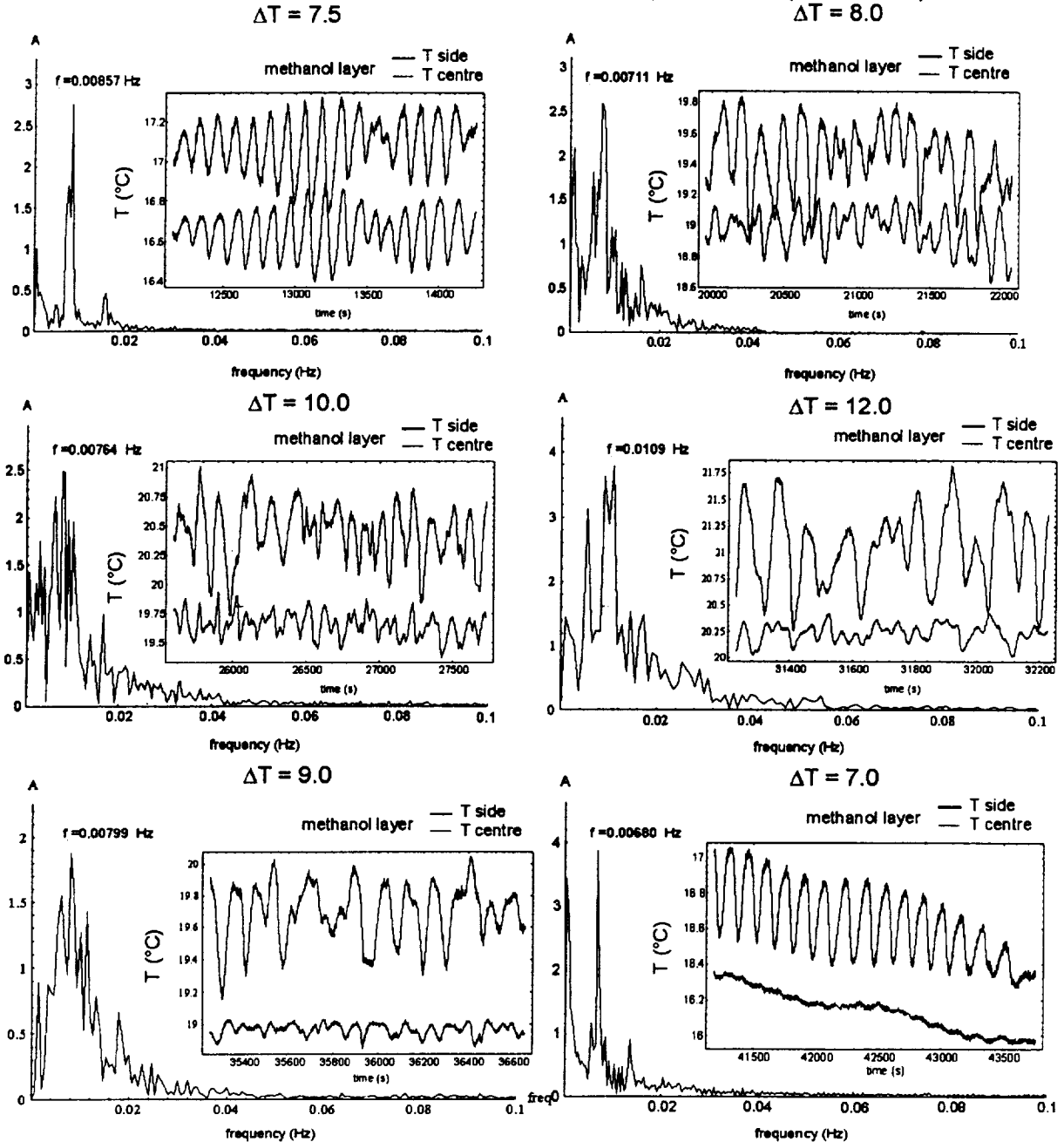
Numerically, the onset for the convection is found at $\Delta T = 2.2$ °C. The convection is oscillatory at the threshold as predicted by the linear stability analysis. The evolution of the flow pattern (isostream lines and isotherms) for $\Delta T = 2.3$ °C is shown here below. The flow pattern presents a nearly perfect left-right mirror symmetry. The oscillations proceed as follow: two small rolls appear in the centre region of the cell ($t = 0.8$), they grow while squeezing on the lateral wall the side rolls ($t = 1.6$); this process repeats one more time during the whole cycle from $t = 2$.



Experimental Results

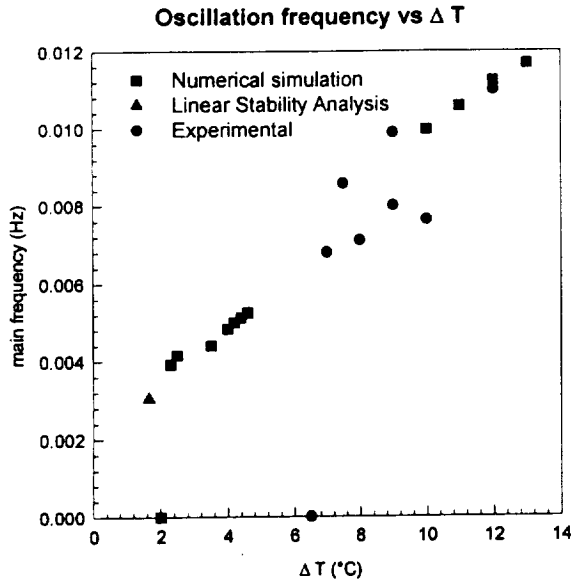
Temperature

The evolution of temperature recordings inside the methanol layer and the corresponding frequency spectrum are shown here below. At the onset of convection ($\Delta T = 7.5^\circ\text{C}$), the oscillation pattern is simple although the amplitude is not regular. The amplitude of the temperature oscillation recorded on the side thermistor and on the centre one are of the same order of magnitude. The frequency spectrum is composed of a dominant peak at $f = 0.00857\text{ Hz}$. When ΔT is increased, the oscillation pattern becomes more and more complex and the spectrum composed



of multiple peaks. After the onset, the main frequency tends to increase as ΔT increased. When ΔT is decreased back to the threshold value, the oscillations slow down and become very regular

as at the beginning of the experiment. As the experiment goes on, the amplitude of the signal recorded with the side thermistors is decreasing continuously. The reason for this unexpected behaviour is still under investigation.



The next figure allows the comparison between the main oscillation frequency for the experimental, numerical and linear stability analysis values. The frequency of oscillations tends to increase as ΔT is increased. Although the critical ΔT for the experiment is much larger than for the numerical one, the oscillation frequencies are of the same order of magnitude. There is also a nice agreement between the linear stability analysis and the numerical computations. It is important to note that no main frequency may be determined in the numerical computation for $5^\circ\text{C} < \Delta T < 10^\circ\text{C}$ because the frequency spectrum is continuous.

The discrepancy between experimental and theoretical ΔT is so large that it cannot be attributed to the imprecision on the physical parameters of the liquids. The interface could be eventually blocked by some impurities but in such a case, the agreement between the experimental and numerical oscillatory frequencies cannot be explained. The large difference observed could be explained by 3D effects. In the 2D approximation, one of the dimensions of the fluid cell is not considered. In the y direction, the fluid cell is only 35 mm long. It is possible that the lateral walls are exerting a strong stabilising effect on the onset of the instability preventing the development of convective mode relying on 3D travelling waves. Once the critical temperature difference becomes large enough, convective mode compatible with restricted geometry will be able to start with a frequency determined by ΔT . This hypothesis has to be checked in the future performing for example 3D computations.

The discrepancy between experimental and theoretical ΔT is so large that it cannot be attributed to the imprecision on the physical parameters of the liquids.

Velocity fields

The quality of the images and the 3D nature of the flow does not allow to visualise the evolution of the velocity field during the whole experiment. More than 1000 velocity maps have been computed using a digital particle image velocimeter developed by ESA. Tracer particles are mainly visible in the central layer and partially visible in the cold methanol layer. An example of the evolution of the velocity field for $\Delta T = 7^\circ\text{C}$ during 3 min. is shown on the last page figure. Two successive fields are separated by 25 s. The convection is unsteady and driven by both interfaces as predicted by the theory and the numerical simulations. The detailed analysis of the velocity field evolution has not been achieved yet.

Conclusions and future plans

This report provides a preliminary overview of the experimental results obtained during the LMS mission. This experiment can be considered as very successful. The current concept of the fluid cell has proven to be very efficient. Mechanically stable three layers configurations could be achieved in microgravity playing on the differential wetting properties of the liquids.

For the first time, oscillatory thermocapillary convection has been observed at the onset of the Marangoni-Bénard instability. This experiment demonstrates the existence of an oscillatory mechanism that is a specific feature of multilayer systems. The oscillations are robust, tend to accelerate when the thermal constraint is increased and become complex very close to the threshold. The condition for the existence of these oscillations is very simple and can be fulfilled in many physical systems of practical interest. In the future, this experiment will be proposed for a

new flight if such an opportunity is presented. A reply would allow to investigate in details all the features of this oscillatory mode and also to determine the 3D structure of the flow.

Acknowledgements

The authors are thankful to all the persons, agencies and companies who participated to the success of the LMS mission in general and to the development of the experimental hardware.

The preparation of this experiment has been supported by the SSTC (Services du Premier Ministre, Affaires Scientifiques Techniques et Culturelles) through the PRODEX programme of ESA

Selected bibliography

Bénard, H. 1900 Les tourbillons cellulaires dans une nappe liquide. *Rev. Gén. Sciences Pure Appl.*, **11**, 1261-1271.

Block, M.J. 1956 Surface tension as the cause of the Bénard cells and surface deformation in a liquid film. *Nature* **178**, 650 - 651.

Chandrasekhar, S. 1961 *Hydrodynamic and Hydromagnetic Stability*, Oxford University Press, 652 p.

Colinet, P., Géoris, Ph., Legros, J.C. & Lebon, G. 1996 Spatially quasiperiodic convection and temporal chaos in two-layer thermocapillary instabilities. *Phys. Rev. E*, **54**, 514-525.

Géoris, Ph., Hennenberg, M., Simanovskii, I.B., Nepomniaschy, A., Wertgeim, I. & Legros, J.C. 1993 Thermocapillary convection in a multilayer. *Phys. Fluids A*, **5**, 1575 - 1582.

Harkins, W.D. 1952 *The Physical Chemistry of Films*. Reinhold Publishing Corporation, 413 p.

Koschmieder, E.L. 1992 *Bénard Cells and Taylor Vortices*. Cambridge University Press, 337 p.

Pearson, J.R. 1958 On convection cells induced by surface tension. *J. Fluid Mech.* **4**, 489-500.

Scriven, L.E. & Sterling, C.V. 1963 On cellular convection driven by surface tension gradients : effects of mean surface tension and surface viscosity. *J. Fluid Mech.* **19**, 321-340.

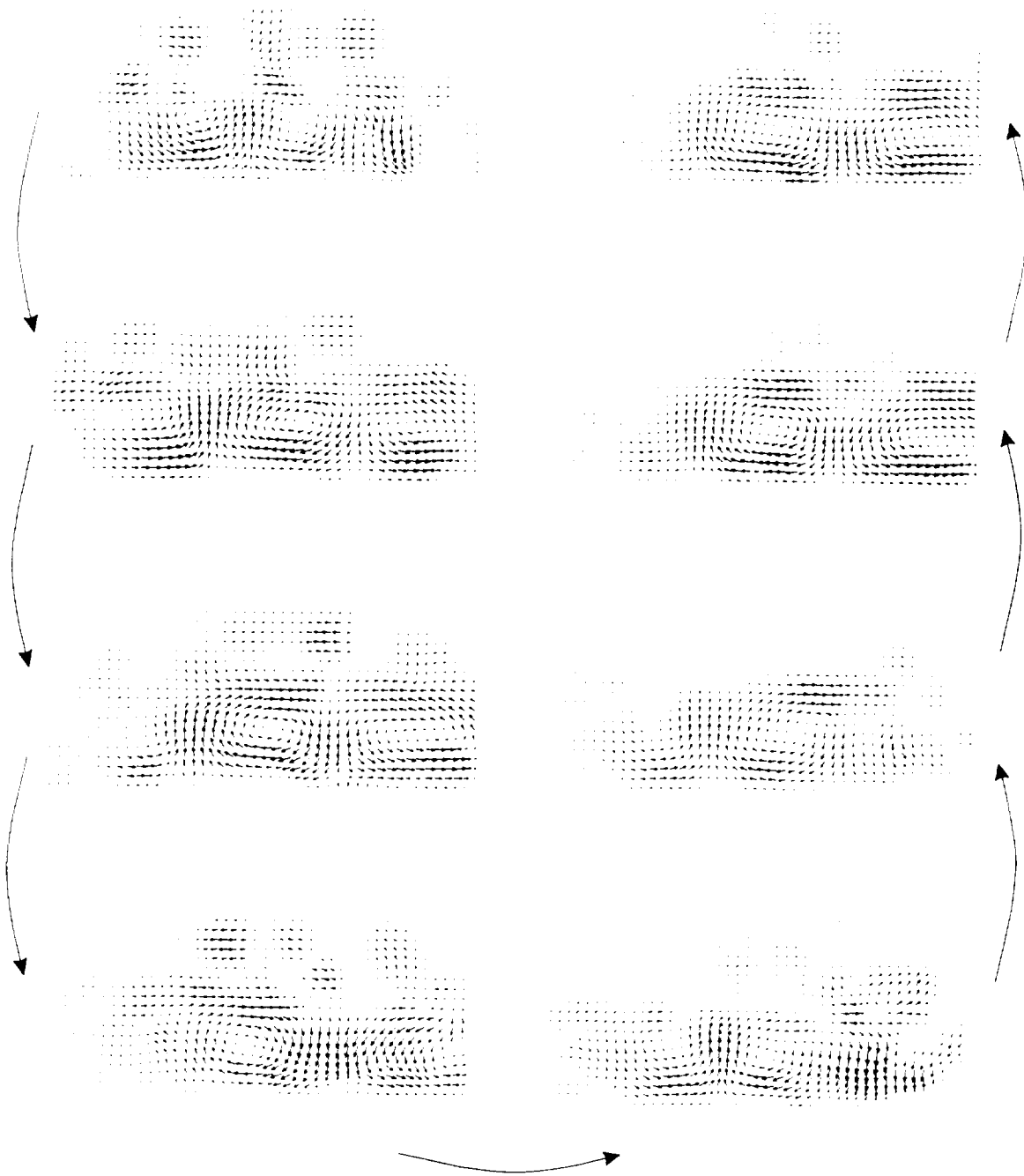
Scriven, L.E. & Sterling, C.V. 1956 Interfacial Turbulence: Hydrodynamic Instability and the Marangoni Effect. *A.I.Ch.E. Journal* **6**, 514-523.

Simanovskii, I.B. and Nepomniaschy A. A. 1993 *Convective instabilities in systems with interface*. Gordon and Breach Science Publishers, 276 p.

Wahal, S. & Bose, A. 1988 Rayleigh-Bénard and interfacial instabilities in two immiscible liquid layers. *Phys. Fluids* **31**, 3502 - 3510.

Zeren, W. & Reynolds, W. 1972 Thermal instabilities in two-fluid horizontal layers. *J. Fluid Mech.* **53**, 305-327.

Evolution of the velocity field in the central layer for $\Delta T=7^\circ\text{C}$; Two successive fields are separated by 25 s.



Bubble, Drop and Particle Unit (BDPU)

Thermocapillary Convection in Multilayer Systems

Principal Investigator:

Dr. Jean-Claude Legros
Université Libre de Bruxelles
Brussels, Belgium

MICROGRAVITY RESEARCH CENTER

The Life and Microgravity SpaceLab Mission

Thermocapillary Convection in Multilayer Systems

Overview of the Preliminary Results, August 1997.

J.C. Legros and Ph. Georis

Objectives

This experiments aims to observe and measure the features of thermocapillary convection in multilayer systems heated parallel to the interfaces. In the absence of the buoyancy mechanism, heat, mass and momentum transfer inside and between connected liquid phases are due to the interfacial tension gradients along the interfaces. Interfacial tension depends on the temperature and on the composition. For practical reasons in model experiments like this one, interfacial tension gradients are generated imposing different temperature set points on the boundary of the fluids. When one of the fluid phase is a gas, its influence on the flow pattern is neglected because of its low dynamical viscosity. More interesting are the cases wher multiple liquid layers are superposed and submitted to temperature gradients. In such configurations, the specificity of the thermocapillary effect cannot be assessed on the Earth. Indeed, buoyancy and thermocapillary effect will cooperate or compete in the different layers depending on their position. This experiment will provide reliable data set for the validation of the theoretical and numerical models already developed.

The experimental system we are dealing with is shown on fig. 1. The experimental hardware is designed in such a way that both two and three layer configurations may be investigated in the same test container one after each other.

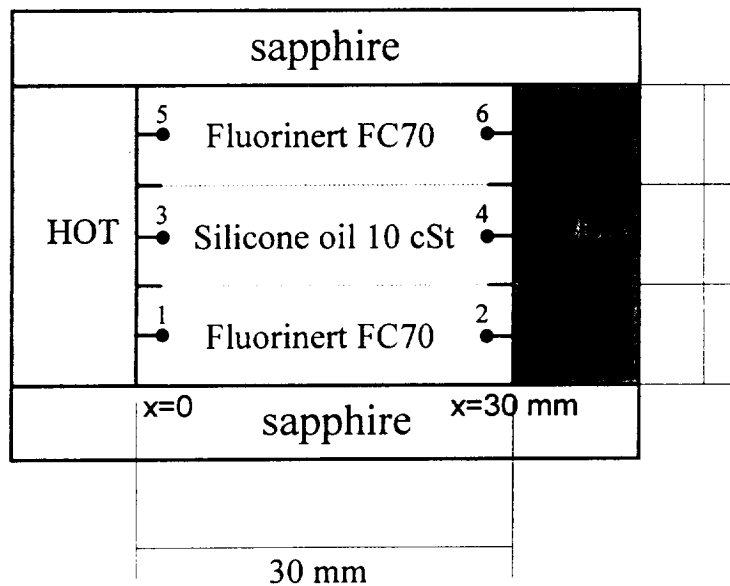


Fig 1. experimental set up

Background

The fluids chosen for this experiment are perfectly immiscible, transparent and inert. Moreover, they form an interface insensitive to contamination. Their properties are summarised in table 1.

Table 1 : Fluids properties

	Fluorinert FC70 (1&3)	Silicone oil 10 cSt (2)	(1)/(2)
ν ($\text{m}^2 \text{s}^{-1}$)	$13.4 \cdot 10^{-6}$	$9.08 \cdot 10^{-6}$ (35 °C)	1.48
μ ($\text{kg m}^{-1} \text{s}^{-1}$)	$2.55 \cdot 10^{-2}$	$8.40 \cdot 10^{-3}$ (35 °C)	3.04
λ ($\text{W m}^{-1} \text{K}^{-1}$)	$7.00 \cdot 10^{-2}$	$1.34 \cdot 10^{-1}$	0.522
κ ($\text{m}^2 \text{s}^{-1}$)	$3.44 \cdot 10^{-8}$	$9.51 \cdot 10^{-8}$	0.362
ρ (kg m^{-3})	1940	934	2.08
Pr	390	95	4.11
$\sigma_{\text{FC70} - \text{Si10cSt}}$ (N m^{-1})	$6.9 \cdot 10^{-3}$		
$\frac{d\sigma_{\text{FC70} - \text{Si10cSt}}}{dT}$ ($\text{N m}^{-1} \text{K}^{-1}$)	$-2.7 \cdot 10^{-5}$		

$\frac{d\sigma_{\text{FC70} - \text{Si10cSt}}}{dT}$ has been measured using the maximum drop weight method described by Harkins (1952). The value obtained is in good agreement with the measurement performed by Burkersroda et al (1994) with the du Noüy ring technique ($2.9 \cdot 10^{-5} \text{ N m}^{-1} \text{K}^{-1}$).

The temperature dependence for the silicone oil - Fluorinert interfacial tension is only half that of the silicone oil - air.

Fluid container

The fluid container is closed on two sides by one centimetre thick sapphire windows. The internal dimensions of the fluid container are 60 mm x 30 mm x 24 mm. Initially, the layers are separated by two stainless steel curtains preventing any mixing before the beginning of the experiment. The boundaries between the layers are maintained leak tight by Viton seals moulded on an antiwetting frame forming a knife edge. At the beginning of the experiment the curtains are pulled out and slowly wounded (0.25 mm s^{-1}) on rollers creating two free liquid - liquid interfaces subjected to the Marangoni effect.

Stability of the three layer configuration

In microgravity, the static shapes of the connected liquid phases are governed by the interfacial forces only. In the absence of walls, a three layer configuration such as depicted in fig. 1. would be unstable. Indeed, the surface tension forces would act to minimize the surface with respect to the volume of the layers, curving the free interfaces and leading supposedly to connected spherical phases. In a container, the situation is different because the layers may keep a flat shape provided their edges are properly anchored on the solid walls. Here, the anchorage is achieved using two stainless steel frames coated on one side with a Teflon film (fig 2) that prevents the creeping of the silicone oil along the quartz wall. Unlike quartz or stainless steel, Teflon is wetted preferentially by Fluorinert rather than by silicone oil. Thus the Teflon coated sides of the frames are oriented towards the Fluorinert layers.

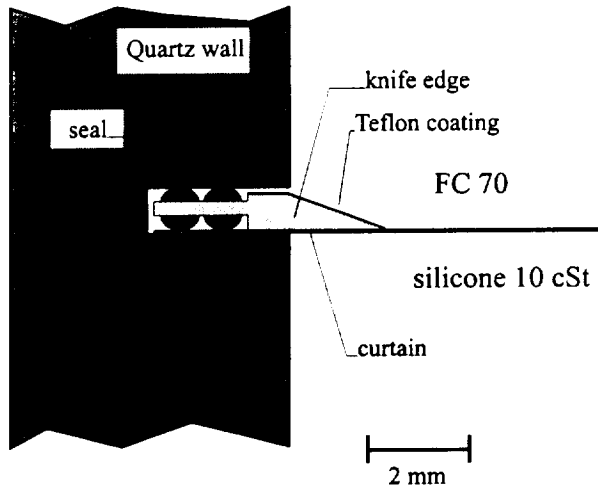


Fig. 2: antiwetting knife edge

Besides controlling the wetting of the walls, one must ensure that the experimental set up is such that the interfacial tension counterbalances the density difference of the liquids effectively (this is important because of the residual gravity level in the space shuttle). This condition must be fulfilled taking into account that the liquid layers are enclosed in a fixed volume.

In the simplified case of the Rayleigh-Taylor instability - the residual gravity is normal to the interfaces - the surface tension stabilises the arrangement for sufficiently short wavelengths. The critical wavelength λ_m for the onset of the Rayleigh-Taylor instability for two liquids of infinite lateral extension is given by the capillary length (Chandrasekhar 1961).

The maximum gravity level acceptable g^* is estimated to $10^{-2} g_0$ knowing that when λ_m is larger than the length of the interface, the Rayleigh-Taylor instability cannot start. In the space shuttle, the mean microgravity level being lower than $10^{-4} g_0$, the Rayleigh-Taylor instability mechanism will be inactive for the geometry chosen here and indeed has not been observed.

Methods of data acquisition and analysis

Thermal data

The temperature of the layers is measured with six thermistors. The signals are recorded continuously. In high Prandtl number fluid, the velocity field is slaved to the thermal field. The temperature measured locally in the layers is thus correlated to the convective field.

Images

The layers are seeded with tracer particles whose diameter range between 30 and 60 μm . Their density is matching the density of the liquids in order to prevent sedimentation due to the residual gravity level. The test container is shaken just before it is inserted inside the facility so the tracer particles are uniformly suspended in the layers.

The particles are visualised in a 1mm laser light sheet parallel to the longest side of the cell. The particles are sufficiently small to follow perfectly the streamlines of the flow. Their position as function of time is directly correlated to the local velocity of the liquid.

The velocity field in the light sheet plane is computed using a dedicated Digital Particle Image Velocimeter (DPIV) running on a workstation. This software is based on a grey level correlation algorithm allowing to determine the displacement of a small particle patterns with a sub pixel accuracy. Two successive images sampled at times t and $t+\Delta t$ are divided in square cells whose scale is smaller than the scale of the flow. The correlation algorithm determines the displacement of each cell within the time interval Δt . the displacements computed in pixels are then converted in $\mu\text{m s}^{-1}$ using a calibration parameter.

Numerical and Theoretical Results

Analytical Approach

A simple analytical expression describing the convective flow may be found for $L/h \rightarrow \infty$. This technique has been used by several authors and will not be described here. The non-

$$\begin{cases} v_{x1} = k z (2 - 3 z) \\ v_{x2} = k (-6 z^2 + 18z - 13) \\ v_{x3} = k (-3 z^2 + 16 z - 24) \end{cases}$$

with $k = \frac{1}{(4 + 6M)} \frac{\text{Ma}}{\text{A Pr}}$

dimensional temperature gradient is assumed constant and equal to the invert of the aspect ratio A^{-1} . The flow being parallel vertical velocity is assumed to vanish everywhere. The horizontal velocity profile along the vertical axis can be computed analytically for the two and the three layer cases.

$$\begin{cases} v_{x1} = l z (2 - 3 z) \\ v_{x2} = l (-3z^2 + 10 z - 8) \end{cases}$$

with $l = \frac{1}{(4 + 4M)} \frac{\text{Ma}}{\text{A Pr}}$

$$\text{where } M = \frac{\mu_2}{\mu_1}, \quad A = \frac{L}{h} \quad \text{and} \quad \text{Ma} = \frac{\frac{d\sigma}{dT} \Delta T h_1}{\kappa_1 \mu_1}$$

The analytical forms of the velocity profiles are plotted versus the vertical coordinate on fig. 3.

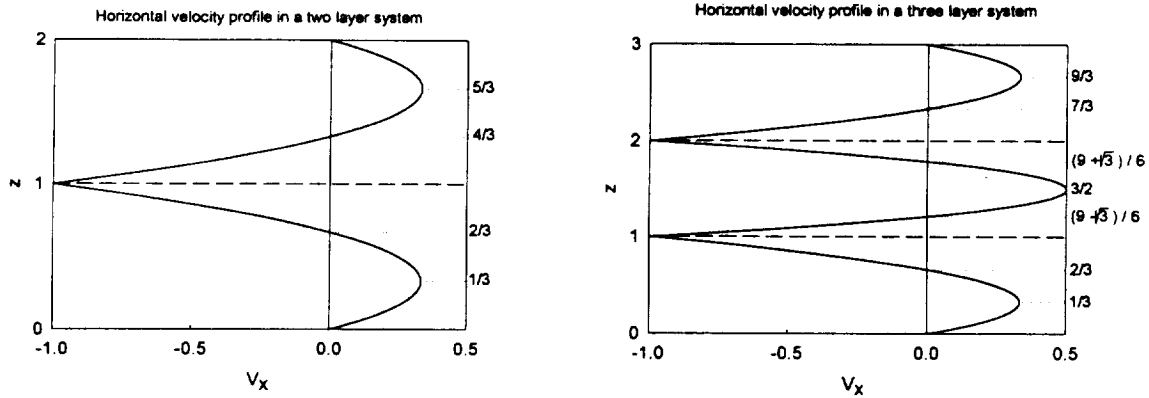


Fig 3: asymptotic velocity profiles for the two and three layer systems

In the two layer system, the velocity profiles in the layers are identical although the configuration is not. In layer 1, the return flow velocity is maximum at $z=1/3$ where it is one third of the interfacial velocity. In the symmetrical three layer system, the velocity profile has the same symmetry as the physical configuration. The velocity profiles in layers 1 and 3 are identical to those observed in the two layer configuration. The intensity of the return flow in layer 2 is half of the interfacial velocity. The shape of the velocity profile identical to the shape determined for the three layer configuration. The velocity vanishes at $h_0=2/3 h$. The maximum velocity which is located at $h_m=1/3$ in the bulk is one third of the velocity at the interface. $l > k$ indicating that the flow is more intense in the 2 layer case than in the 3 layer case. This is explained by the large shear stress imposed in layer 3 by two moving interfaces.

For the fluids used in the experiment, the dimensional value of the velocity may be found from the physical parameters given in table 1:

$$V_x \max (2\text{layer}) = 53.1 \mu\text{m s}^{-1} \text{ } ^\circ\text{C}^{-1} \Delta T$$

$$V_x \max (3\text{ layer}) = 47.3 \mu\text{m s}^{-1} \text{ } ^\circ\text{C}^{-1} \Delta T$$

2D Finite difference simulations

The non-linear Navier Stokes and the energy equations are solved numerically in 2D for the actual set-up. In each layer l , the dimensionless governing equations expressed in terms of stream function and vorticity are:

$$\partial_t \phi + \partial_z \psi \partial_x \phi - \partial_z \phi \partial_x \psi = \frac{\nu_l}{\nu_1} \Delta^2 \phi$$

$$\text{Pr} (\partial_t T + \partial_z \psi \partial_x T - \partial_z T \partial_x \psi) = \frac{\kappa_l}{\kappa_1} \Delta^2 T$$

$$\text{where: } \frac{\partial \psi}{\partial z} = v_x \text{ and } -\frac{\partial \psi}{\partial x} = v_z, \quad \Delta^2 \psi = \phi$$

The equations are discretised on a uniform rectangular mesh using the centred difference technique and solved using ADI scheme. The Poisson's equation is solved using the Gauss-Seidel relaxation technique. The Navier Stokes, energy and Poisson's equations are solved for the internal nodes in each layer independently then the boundary conditions are applied to compute the value of the vorticity and temperature on the boundary nodes.

Numerical results

The convective pattern for increasing temperature differences have been computed for the two (fig. 4) and the three layer (fig 5.) systems.

The flow patterns as shown on fig. 4 for the Fluorinert FC70 – silicone oil 10 cSt systems are very similar in both layers although the fluids have quite different physical properties. The temperature isotherms are highly distorted large velocity of the interface even for a temperature difference as small as 2.5 °C.

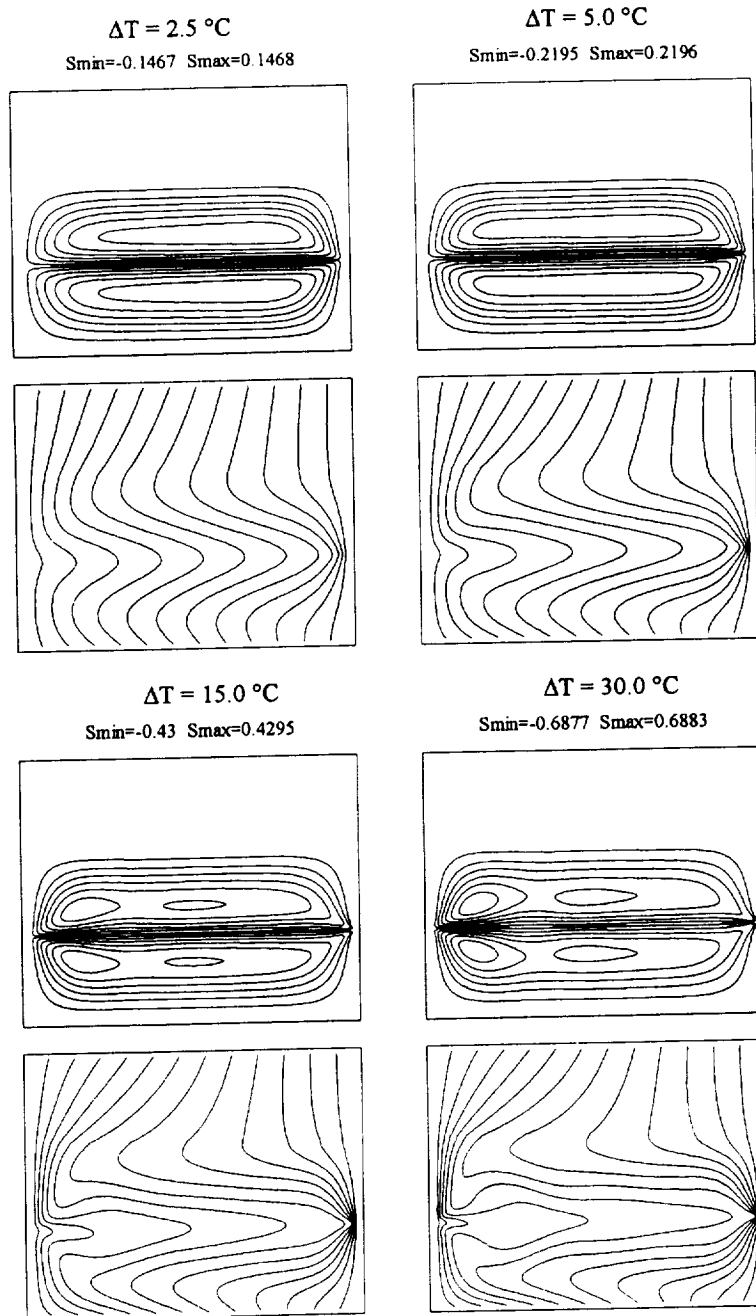


Fig. 4: Steady flow patterns and isotherms in the two layer system FC70 – silicone 10 cSt

For large values of ΔT , recirculation vortices appear in the primary cellular structure. The fluid is strongly accelerated when it reaches the interface near the hot wall. The intense surface tension driven flow is bringing hot liquids near the cold wall where a very steep temperature gradient is created.

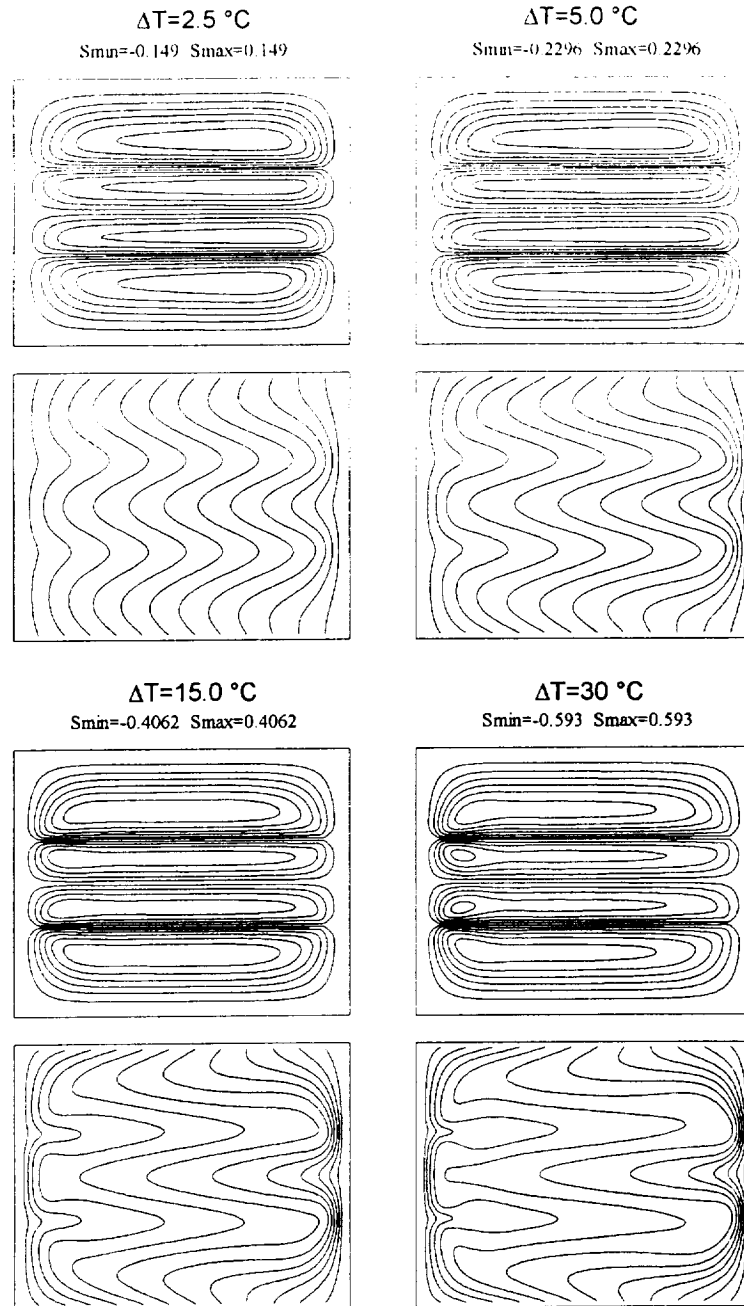


Fig 5: steady flow patterns and isotherms in the three layer system FC70 – si. 10 cSt - FC70.

Steady flow pattern computed for the three layer system are shown on fig. 5. The situation is very different from the two layer case. The flow patterns are reflecting the geometry of the setup. Interfacial motion creates two symmetrical contrarotative vortices in the middle layer. In the lateral layers, the flow pattern is mono cellular with no recirculation even for the largest temperature differences. The deformation of the isotherms is, as compared with the corresponding states of fig. 4, less pronounced.

Experimental Results

The time span allowed to the experiment has permitted to obtain to observe steady flow patterns for five thermal gradient in the two layer and four in the three layer configuration.

Two layer convection

The velocity maps obtained for increasing ΔT are shown on fig. 6. For small ΔT , the flow is mono cellular in both layers. The velocity reaches its maximum value in the central region of the interface. As ΔT is increased, the maximum velocity is found closer and closer to the hot wall. For the largest ΔT , the local vortex located near the hot wall is clearly apparent just as in the numerical simulations

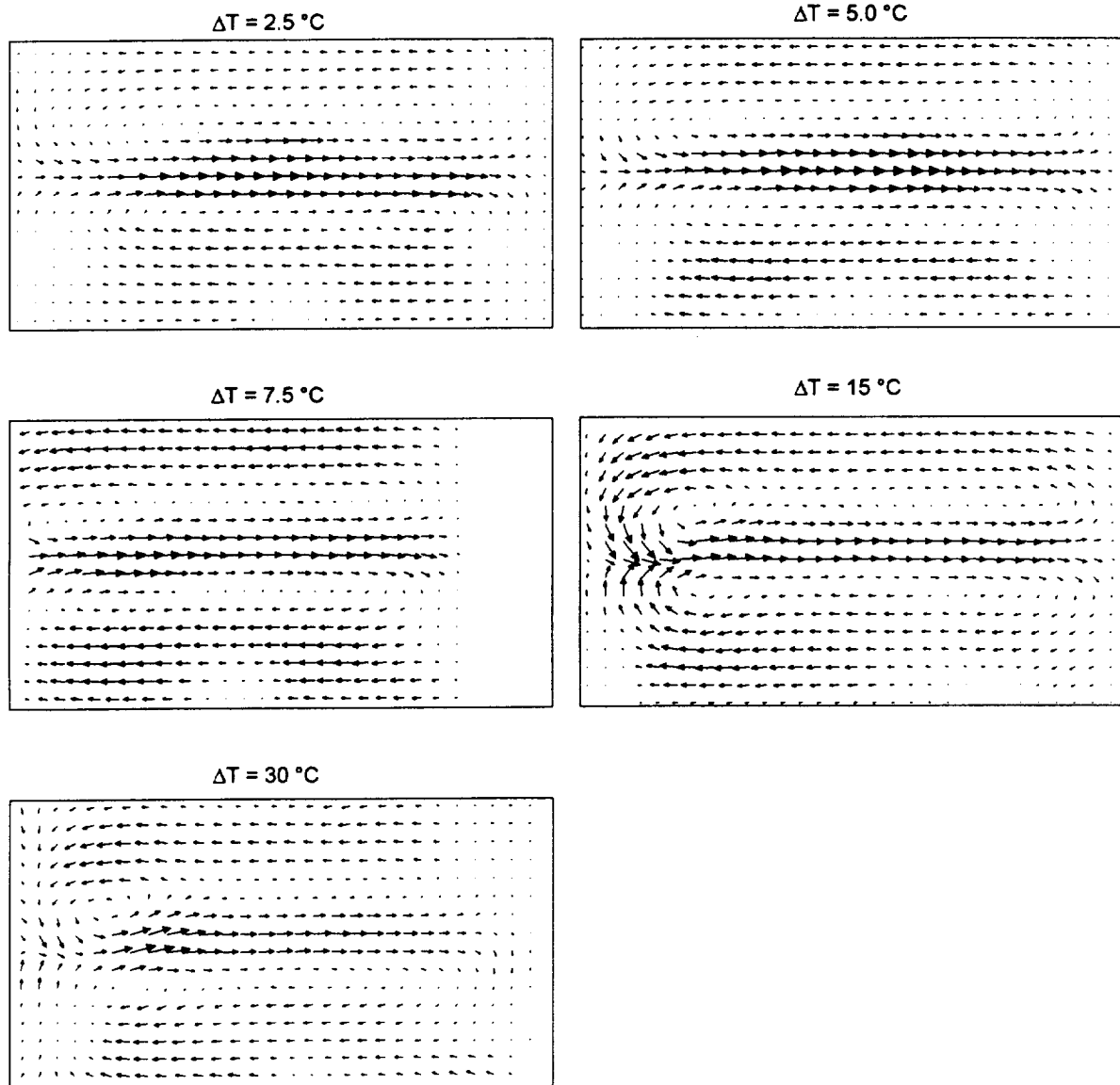


Fig. 6: velocity maps in the two layer system FC70 – silicone 10 cSt

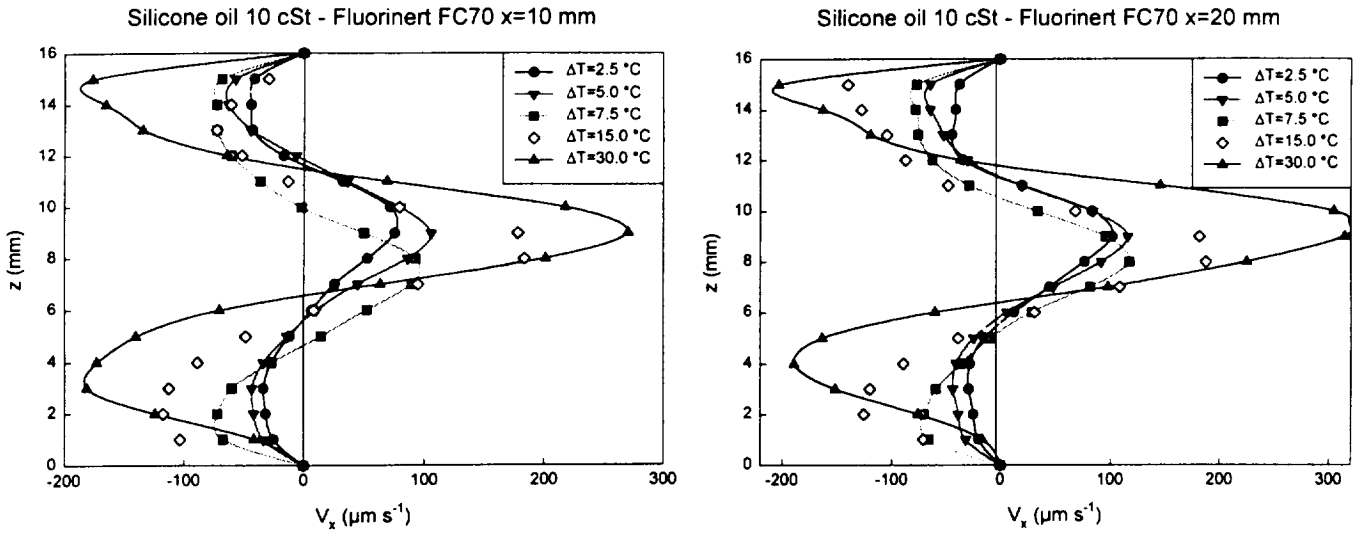


Fig. 7: horizontal velocity profiles at $x= 10$ mm and $x=20$ mm

The horizontal velocity profiles along two vertical axis at $x= 10$ mm and $x=20$ mm are shown on fig. 7. Because of the thickness of the seal (fig. 2), the velocity of the fluids at the interfaces cannot be determined accurately and is probably underestimated. The intensity of the flow is, as expected proportional to ΔT . Also, it appears that the shape and the intensity of the flow is comparable at $x= 10$ mm and $x= 20$ mm.

For the comparison between the asymptotic computation, the numerical simulations and the experimental results, the maximum velocity of the return flow (V_{mrf}) is plotted versus the temperature difference imposed (or the Marangoni number) between the flanges (fig. 8). The experimental data are fitting the following empirical two parameters function:

$$V_{mrf} = V_{\infty} (1 - e^{-a\Delta T})$$

There is a clear discrepancy between the numerical (crossed squares) and the experimental results. For large values of the Marangoni number, V_{mrf} experimental is twice larger than the numerical one. For the sake of verification, the results of the numerical simulations (squares) for large aspect ratio ($A=10$) and small Marangoni number are in good agreement with the results of the asymptotic approach. The reason for the discrepancy between numerical and experimental values has not been identified yet. Two potential reasons have to be investigated:

In the numerical simulations, the viscosity of the layers is assumed constant which is not the case in reality.

The step thermal gradient created at the interface near the cold wall is not perfectly modelled in the case of large ΔT .

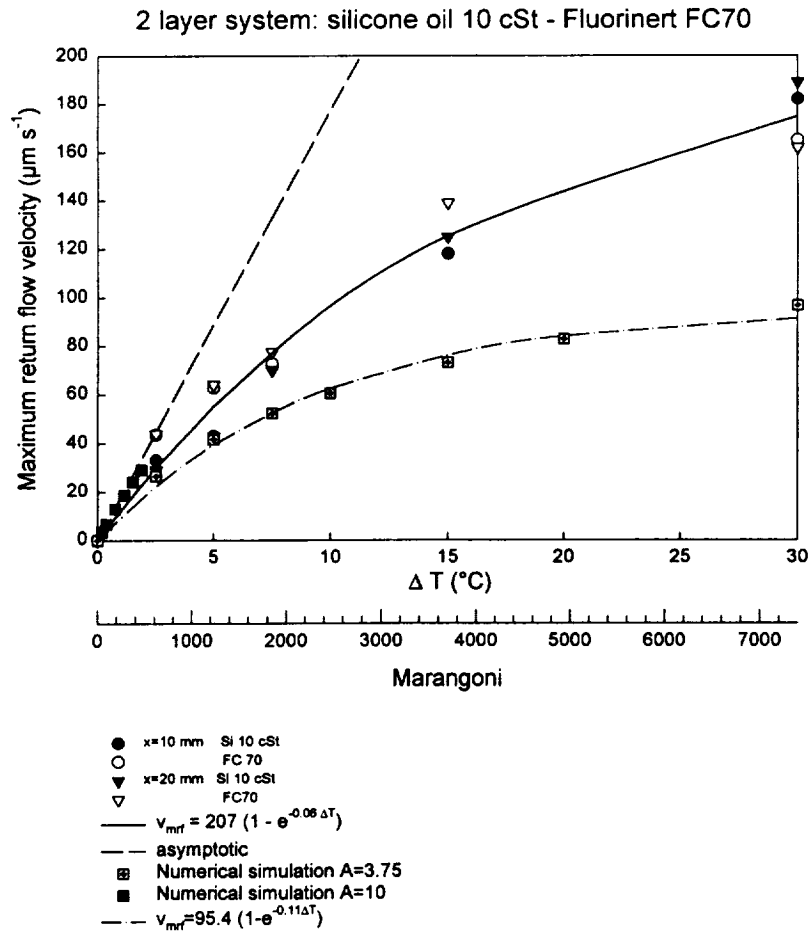


Fig 8 Maximum return flow velocity vs ΔT in the two layer system

Three layer convection

The velocity fields measured for increasing ΔT are shown on fig. 9. As simulated numerically, the flow pattern is symmetrical. There are two convective rolls in the central layer. Visually, the convective patterns compare well with the numerical ones excepted for $\Delta T=15^{\circ}\text{C}$ where the tracer particles are not visible everywhere. In general, the quality of the velocity maps obtained for the three layer experiment is lower than for the two layer one. This is mainly due to the accumulation of tracer particles on the interfaces and on the quartz walls.

The shapes of the velocity profiles at $x=10$ mm and $x=20$ mm shown on fig. 10 compare well with the shape found using the asymptotic theory. The symmetry of the flow pattern is clearly apparent on these profiles.

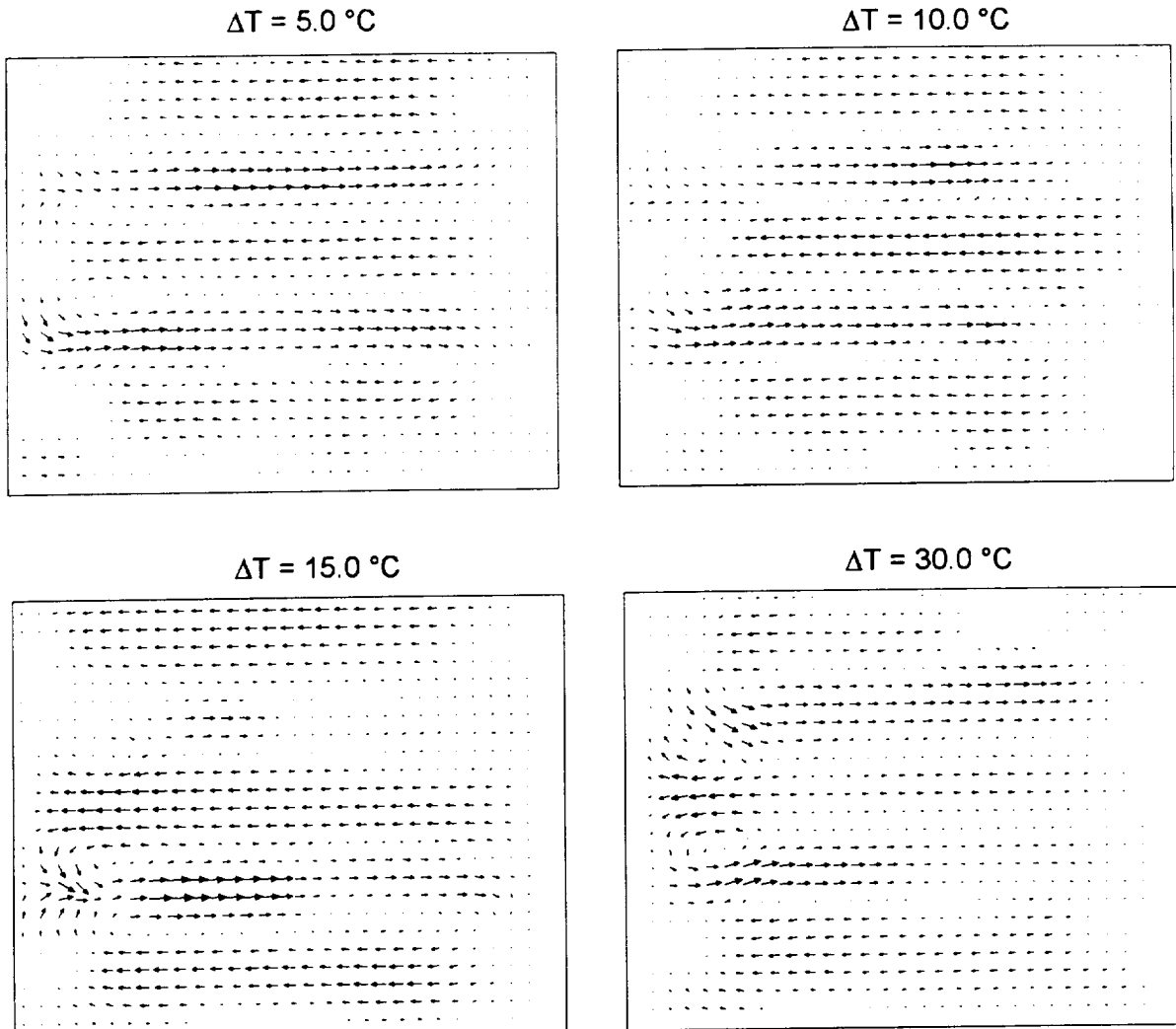


Fig. 9: Velocity maps in the three layer system FC70 – si 10 cSt – FC70

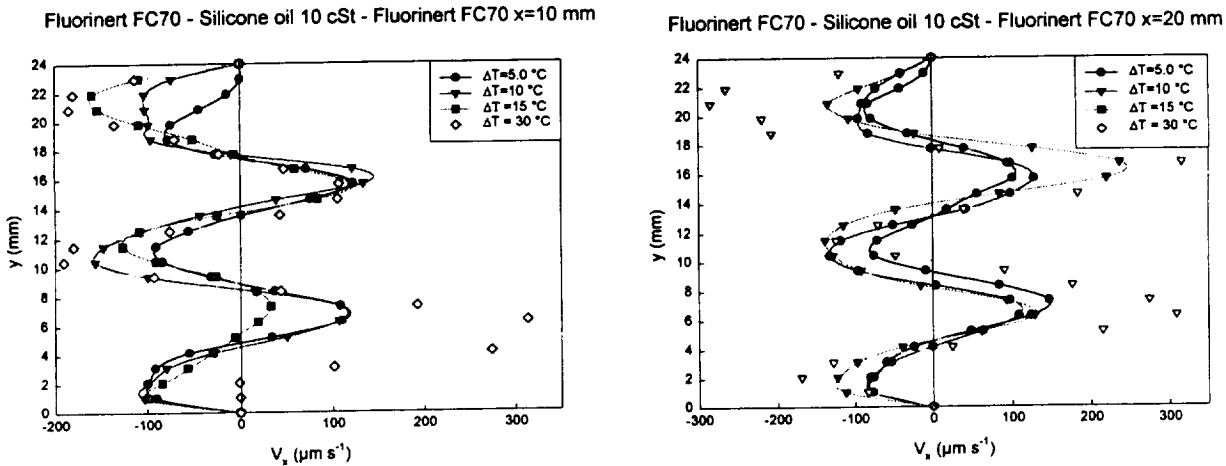


Fig 10: horizontal velocity profiles at $x=10 \text{ mm}$ and $x = 20 \text{ mm}$

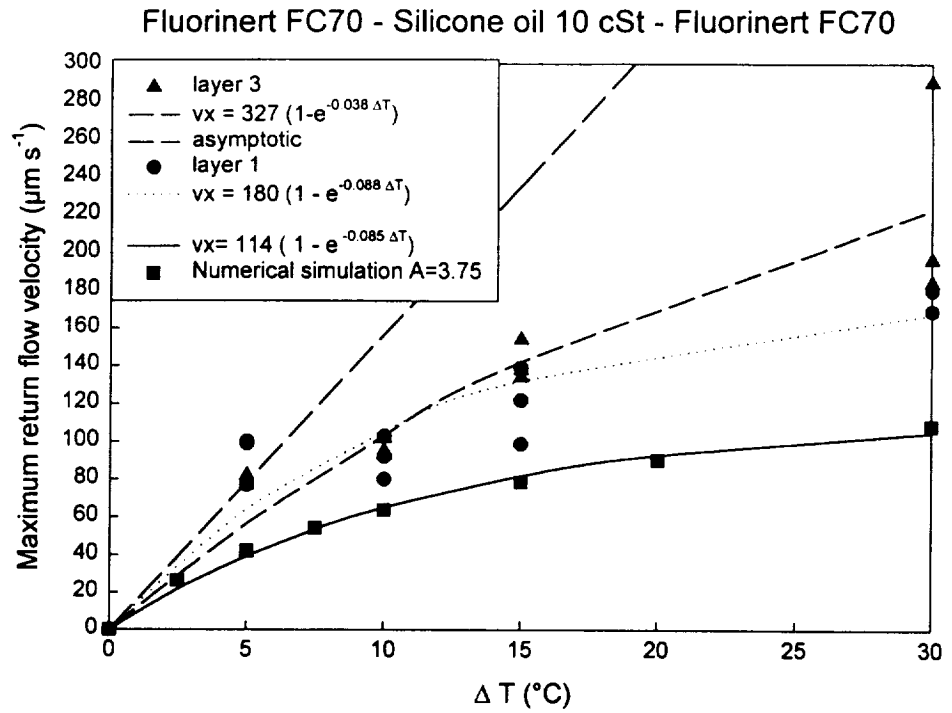


Fig. 11: Maximum return flow velocity in layers 1 and 3 (Fluorinert FC70) vs ΔT

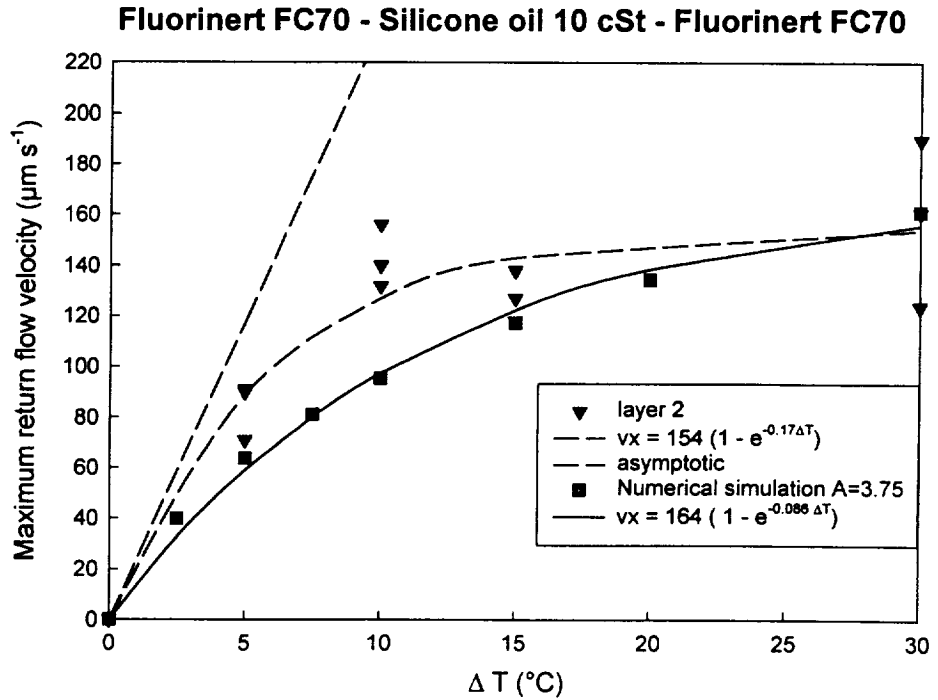


Fig. 12: Maximum return flow velocity in layer 2 (silicone oil 10 cSt) vs ΔT

The plots of the maximum return flow velocity shown on fig. 11 and 12 reveal the same discrepancy between numerical and experimental results. The experimental velocities are significantly larger than the theoretical ones. This is mainly the case in the external layers.

Conclusions and future plans

This report provides a preliminary overview of the experimental results obtained during the LMS mission.

This experiment can be considered as very successful. The curtain concept of the fluid cell has proven to be very efficient. Mechanically stable two and three layers configurations could be achieved in microgravity playing on the differential wetting properties of the liquids.

Quantitative velocity fields on the thermocapillary convection in multilayer systems have been obtained. The flow patterns observed are similar to those obtained by numerical simulations. However, the experimental velocities are significantly larger than the computed ones. The reason for this discrepancy is currently under investigations.

Acknowledgements

The authors are very grateful to Professor J. Koster (Colorado University, Boulder USA) for the use of fluid cell he conceived for the IML2 mission and for the fruitful discussions on thermocapillary convection.

The authors would like also to thank Dr L. Qiu Sheng and Dr B. Roux for their precious advices on the numerical simulation of thermocapillary convection.

The authors are thankful to all the persons, agencies and companies who participated to the success of the LMS mission in general and to the development of the experimental hardware.

The preparation of this experiment has been supported by the SSTC (Services du Premier Ministre, Affaires Scientifiques Techniques et Culturelles) through the PRODEX programme of ESA

Selected bibliography

Burkersroda, C., Prakash, A. & Koster, J. 1994 Interfacial Tension between Fluorinert and Silicone Oils. 1994, *Microgravity Quart.* 4 (2), 93-99.

Chandrasekhar, S. 1961 Hydrodynamic and Hydromagnetic Stability, Oxford University Press, 652 p.

Harkins, W.D. 1952 The Physical Chemistry of Films. Reinhold Publishing Corporation, 413 p.

Peyret, R. & Taylor, D. 1990 Computational Methods for Fluid Flow. Springer Verlag, New-York, 358 p.

Prakash A. and J.N. Koster, "Convection in Multiple Layers of Immiscible Liquids in a Shallow Cavity - I", *Int. J. Multiphase Flow* Vol. 20, n°2, pp 383-396, 1994.

Prakash A. and J.N. Koster, "Convection in Multiple Layers of Immiscible Liquids in a Shallow Cavity —II", *Int. J. Multiphase Flow* Vol. 20, n°2, pp 397-414, 1994.

Qiu Sheng L, " Couplage entre forces interfaciales dans un système multicouche de fluides immiscibles avec ou sans effet des forces thermogravitationnelles", Ph D Thesis, 1994 Université de Marseille.

Villers D., »Couplage entre les convections capillaire et thermogravitationnelle », PhD Thesis, 1989, Université de Mons Hainaut, Belgium.

Bubble, Drop and Particle Unit (BDPU)

Bubble and Drop Interaction with Solidification Front

Principal Investigator:

Dr. Rodolfo Monti
Università degli Studi di Napoli
Naples, Italy

Bubble and drop interaction with solidification front: scientific results obtained during the LMS mission

Raimondo Fortezza, Dario Castagnolo, Enrico Ceglia

MARS Center
via Comunale Tavernola, 80144, Napoli, Italy

Rodolfo Monti

DISIS, University of Naples
P. Tecchio 80, 80126, Napoli, Italy

Objectives

This report deals with the scientific results obtained during the "MONTI" experiment performed in the BDPU facility flown on board of the Spacelab LMS mission. The objective of the experiment was to study the interaction of drops and bubbles with a moving solidification front. This interaction between the bubbles and the solidification/melting front was studied by analysing the bubble sizes and the front velocity. This will provide us with information on the manner in which bubbles are captured by (or pushed away from) a moving solidification/melting front [7].

This is aimed at better understanding the behaviour of the bubbles when released from or approaching the solid front, and from this we could eventually learn how to prevent the presence of bubbles included in solidified products and how to minimize the impact these bubbles have on the final product.

Finally, in the last part of the experiment water droplets were injected within the melted matrix (a paraffine called Tetracosane). Again, the objective was to study the interaction of these droplets with the solidification front, in order to establish whether they were pushed or engulfed by the front. These results are of great importance in the improvement of production of metal alloys, glasses and ceramics on Earth.

Background

The first part of the experiment was devoted to the study of the interaction between pre-formed gas bubbles (see figures 1 (a) and (b)) and a moving melting/solidification front, obtained by heating a solid tetracosane sample. This sample was contained within the Test Container number 8 (TC#8), placed within the Bubble, Drop and Particle Unit (BDPU), which is a facility developed by the European Space Agency (ESA).

The motivation for performing this experiment in a microgravity environment is that buoyancy and sedimentation effects are negligible, which the study of the interaction possible without additional forces acting on the inclusions. One of the negative aspects of the buoyancy effect is that it leads to undesired distortion of the front and an increased velocity of the melting process.

During the initial phase of the experiment the needle side flange was heated up to a temperature of 80°C (greater than the melting temperature $T_{melt} = 51^\circ\text{C}$), while the net side flange was maintained at a temperature of 45°C. This allowed us to study the movement of the melting front, and its interaction with the gas bubbles that were released.

As the bubbles detach themselves from the melting front, they are gradually absorbed by the liquid tetracosane, this allowed us to determine the diffusion coefficient of the gas bubbles in the liquid.

After some time both flanges were brought to a temperature of 90°C, and the tetracosane sample was completely melted. At this point, the tetracosane was re-solidified from the needle side, which gave us the possibility to study the behaviour of bubbles (ie. whether they are pushed or engulfed) as a solidification front approaches.

The aim of the experiment was also to investigate if any thermocapillary migration effects could have been detected in the large temperature gradient.

In the second part of the experiment water droplets were injected into the liquid tetracosane. Some difficulties were encountered during the injection procedure, since the droplets exhibited a strong wetting capability and did not easily detach themselves from the needle. This problem was overcome by increasing the previously selected dimensions of the droplets and the injection velocity. We then observed the interaction of these larger droplets with the solidification front, in order to establish if the front can modify the shape and the position of the droplets.

Analysis of the flight results

- Observation of bubble release

A post flight analysis of the video images recorded during the experiment onboard the LMS Shuttle mission was carried out. During the first melting phase the position and dimensions of the various bubbles were compared to those set during the filling of the test container on the ground prior to the flight. The following unexpected changes were noted: (i) During the first melting experimental phase, in which the tetracosane specimen is initially melted from one side of the test cell only, bubbles are immediately released as the melting/solidification front begins to move away from the heated side. At this point no bubbles had been foreseen, as the first bubbles set within the tetracosane were expected further along the specimen. (ii) As the front approached the various positions along the specimen where bubble release was expected, some bubbles did not appear at all, and others had dimensions that were not the same as those expected (mostly bigger than they should have been). (iii) In the second part of the first melting phase, the cell is also heated from the other side of the solid tetracosane specimen, close to the net of the test container. As the tetracosane near the net begins to melt and the front moves away from the net, a large bubble is visible between the solid tetracosane and the net. This bubble begins to apply pressure to the visible lower end of the solid, causing it to tilt.

The reasons for these changes may be explained by the method that was utilised to fill the test container with the solid tetracosane prior to the flight. The first part of the filling procedure consisted in placing a hollow, truncated-conical mould of solid tetracosane in the test container, such that the flat part of the mould was pressed against the net within the cell. Various slices of solid tetracosane were then successively placed within the hollow part of the mould, until the cell was completely filled with solid tetracosane. These slices contain semi-spherical hollows, that, when placed one against the other, form the desired air bubbles within the tetracosane solid at pre-specified locations. The discrepancies (i) and (iii) described above may be attributed to the fact that at the contact areas between the hollow tetracosane mould and the slices placed within it, small amounts of air were trapped during the filling of the test container, and this air was immediately released in the form of bubbles as the solid regions near the heated flange (i) and the net (iii) in the vicinity of the contact points began to melt. Three reasons can be put forward to try and attempt an explanation for the discrepancies outlined in (ii) above: (a) Air was trapped between the contact areas of the slices placed in the mould during the filling of the test cell. During the experiment, as the tetracosane began to melt near these areas, this air formed micro-bubbles that coalesced in larger ones so that this air was released in the form of unexpected bubbles, or it began to merge with the pre-formed air bubbles to produce bubbles with dimensions larger than that expected. This trapped air may also have caused the pre-formed bubbles to shift from their set positions as the tetracosane began to melt. (b) As the melting front approached the contact areas between the various slices, liquid tetracosane may have flown into these cavities, causing the pre-formed bubbles to shift, and maybe even to merge to form larger bubbles than expected. (c) A combination of (a) and (b). The second reason (b) seems unlikely as no deformation in the melting front where liquid could have flown into the cavities, was noted. As for the explanation of the changes (i) and (iii), (a) above seems to be the more likely reason to explain variation (ii). A video image analysis was also useful in determining the correct orientation of the test cell with respect to the pre-formed bubbles within the tetracosane solid matrix. Figure 2(a) is a video image during the melting phase, upon which a schematic representation of the bubble positions and dimensions (to scale) have been superimposed. It can be clearly seen that the two bubbles being released from the tetracosane solid correspond to the bubbles 10 and 11 in both position and dimension. Eventhough these two bubbles were relatively close to each other they did not coalesce. The larger bubble within the liquid ahead of these two bubbles was not expected, and it probably resulted from the coalescence of bubbles 4 and 7. A further indication of the correct orientation of the test cell is given in figure 2(b). The tetracosane is in the process of releasing two more bubbles, and the superimposed schematic indicates that these bubbles correspond to bubbles 11 and 12. The schematic has been rotated in correspondence to the rotation which the remaining tetracosane solid has undergone as a result of the large bubble pushing against it from the lower part of the cell on the net side. The two larger bubbles in the liquid towards the needle side correspond to bubbles 10 and 11 seen in figure 2(a), while the coalesced bubble of figure 2(b) has moved towards the bottom corner of the needle side.

- Experimental absorption rate of gas bubbles in tetracosane

The next step in the analysis of the video images was to determine the rate of absorption of the gas bubbles within the liquid tetracosane during the melting sequence of the experiment. This was done by utilising a video analysis tool developed at MARS Center, which plays the stored images of the experimental sequence at different speeds. This allows one to easily move backwards and forwards to a desired instant of the experiment at a selected speed. The frame which must be analysed is then identified and "captured", allowing one to carry out measurements of the bubble radius and location. Eighteen different bubbles with initial radii varying between 0.4725 and 4.1125 mm were analysed at various instances using the video images recorded from the CCD cameras, providing a "top" and "lateral" view of the test cell. The initial radii were measured just after the bubbles were released from the solid tetracosane into the liquid, and after an interval of time the final radii were measured, from which the experimental decrease in radius with time (absorption rate) was calculated.

- Theoretical calculation of absorption rate

From reference [1], the volumetric flow rate of a gas bubble for the diffusion of a gas in a liquid, is given by the following :

$$W = \frac{dV}{dt} = kA \left[\frac{X_{A\infty} - X_{Ao}}{1 - X_{Ao}} \right] \quad (1)$$

where V is the volume, t is time, k is the mass transfer coefficient, A is the surface area of the bubble, d is the bubble diameter, X_{Ao} is the concentration of gas at the gas/liquid interface, and $X_{A\infty}$ is the concentration of gas in liquid at a distance far from the bubble. We assume $X_{A\infty}$ equal to zero, since the concentration of air in the tetracosane upon melting is zero, and it is practically negligible compared to the concentration of gas at the gas/liquid interface for the instances in which the eighteen bubbles were analysed. Equation (1) can be re-written as follows :

$$\frac{dr}{dt} = k \left[\frac{X_{Ao}}{X_{Ao} - 1} \right] \quad (2)$$

where dr/dt is the absorption rate, and X_{Ao} is defined as the ratio between the partial pressure of the bubble and Henry's constant (H). By calculating X_{Ao} and substituting into equation (2), we get :

$$\frac{dr}{dt} = -1.15 \times 10^{-5} k \quad (3)$$

In reference [2] the mass transfer coefficient (k) is defined as follows :

$$k = \frac{D_{AB}}{d} \left[2 + 0.31 \left(\frac{d^3 g \Delta \rho}{D_{AB} \rho_l} \right)^{\frac{1}{3}} \right] \quad (4)$$

where D_{AB} is the diffusion coefficient of the gas in the liquid, and g is the gravitational acceleration. Since g in our case is negligible (of the order of $10^{-6}g_o$), equation (4) can be

reduced to the following : $k = \frac{D_{AB}}{r}$ and substituting for k in equation (3), we finally obtain :

$$\frac{dr}{dt} = -1.15 \times 10^{-5} \frac{D_{AB}}{r} \quad (5)$$

Since the value of D for air in tetracosane is unknown, equation (5) has been applied using various values of D, and these results were then fitted to the experimental data. From this analysis it has been concluded that a suitable value of D for air in tetracosane is $4 \times 10^{-5} \text{ m}^2/\text{s}$. This value is comparable to that for air in water which is between 2 and $3 \times 10^{-5} \text{ m}^2/\text{s}$. The theoretical curve is shown plotted versus the experimental data in figure 3.

- Analysis of the interface shape at the bubble/interface contact point

Theoretically it has been shown [3] that the solid/liquid interface can take on one of 3 different shapes at the particle/interface contact point, depending on the thermal conductivity ratio (α). This is the ratio of the thermal conductivity of the particle (K_g) to the thermal conductivity of the

solid (K_s). For $\alpha < 1$, the interface at the contact point is a bump (Figure 4 (a)), for $\alpha = 1$, the interface is planar (Figure 4 (b)), and for $\alpha > 1$, the interface at the contact point is a trough (Figure 4 (c)). Since the thermal conductivity of air (bubble) is $K_g = 0.0257 \text{ W/m}^\circ\text{K}$, and for tetracosane (solid) it is $K_s = 0.1580 \text{ W/m}^\circ\text{K}$, we have an experimental thermal conductivity ratio, $\alpha = 0.163$. In figures 5, it can be seen that, (as is expected theoretically), for $\alpha = 0.163$ (ie. < 1), the interface shape at the bubble/interface contact point is a bump.

- **Comparison between analytical and experimental bubble velocities.**

The experimental bubble velocities measured for various bubble radii were compared to the analytical bubble velocities calculated from [4] for the case of Stokes buoyancy convection, due to the residual gravity obtained from the OARE accelerometer data ($\approx 0.7 \mu\text{g}$). From figure 6 it can be seen that the experimental values are in good agreement with those obtained analytically. We can conclude that the observed bubble migrations are exclusively due to the residual gravity and therefore no Marangoni convection is present. The reason for this is that the non-homogenous liquid contaminates the surfaces of the bubbles preventing a surface tension gradient from forming. This is in accordance with [6], where no Marangoni convection was observed for the case of bubbles in CBr_4 .

The presence of a thermal gradient around the bubble is confirmed by figure 7, where we have superimposed an experimental image with one obtained from numerical simulations. The disturbance of the bubble, (which is the coalesced bubble in figure 2(a)), on the thermal field is evident from the figure.

- **Pushing and engulfing of bubbles by advancing solidification front**

From [5] we get the analytical solution of the velocity of the melting/solidification front :

$$|V_f| = 68 \sqrt{\frac{1}{t}} \text{ microns/sec} \quad (6)$$

Figure 8 compares the analytical solution of the front velocity with that measured experimentally, as well as with that obtained from the numerical simulations, and it can be seen that they are all in reasonably good agreement with one another. The experimental images were studied to see whether any pushing of bubbles by the advancing solidification front, whose velocity was measured to be of the order of $1 \mu\text{m/s}$, could be observed during the re-solidification process. Most of the bubbles that could be clearly observed were engulfed by the advancing solidification front. An exception, in which one bubble was seen to be pushed by the front, is shown in figure 9: bubble 1, which has a radius of 0.9 mm , is pushed by the front as the bubble comes into contact with it, while bubble 2, which is aligned with bubble 1, and has a radius of 1.8 mm , is engulfed as it interacts with the moving front.

- **Drop interaction with solidification front**

In the last part of the experiment, some water droplets (diameters between 5 and 10 mm) were injected into the melted tetracosane. Their interaction with an advancing solidification front was analyzed, and no pushing was observed. During the final stages of the experiment, the liquid tetracosane, which still contained the previously injected droplets, was completely solidified from both sides of the test cell. In the post-flight analysis, the solid tetracosane sample was removed from the experimental test cell, and was sliced in order to observe the positions and the shape of the droplets with respect to the final flight configuration. As expected from this study we can conclude that the advancing solidification front does not push or in any way modify the shape of droplets which have dimensions similar to those used in the experiment.

Conclusions and future plans

This experiment allowed us to study the interaction between a solid/liquid front and gaseous/liquid inclusions. We have been able to make a number of important conclusions from our analysis.

The inclusions with diameters in the range $5 - 10 \text{ mm}$ are engulfed by both the melting and the solidification front.

In spite of the large temperature gradient, no thermocapillary effect was witnessed, because of surface contamination. The observed bubble migration was caused by the residual gravity level.

The absorption of the gaseous particles by the liquid phase and the interface shape at the bubble/interface contact point confirm some of the theoretical expectations.

Future research will be focused on the microscopic interaction between a low melting material solidification front and gaseous inclusions with a much smaller diameter. The intention of this future research is to determine the conditions for which pushing by the front takes place. This is an important point in the fabrication of most composites by melt processing techniques, where the presence of dissolved gas occurs. The management of the insoluble particles is vital to the attainment of the desired physico-mechanical properties.

Also, the solidification regime will be such as to promote either a planar or a non-planar solidification front.

References

1. Bird R, Stewart W, Lightfoot E, "Transport Phenomena", Casa Editrice Ambrosiana, Italy, (1979).
2. Perry R, "Perry's chemical engineers' handbook", Mc Graw-Hill International Editions, (1984).
3. Shanguan D, Ahuja S, Stefanescu D, "An analytical model for the interaction between an insoluble particle and an advancing solid/liquid interface" *Met. Trans. A*, Vol. 23A, Pgs. 669-680, (Feb. 1992).
4. Young N, Goldstein J, Block M, "Motion of bubbles in a vertical temperature gradient" *J. Fluid Mech.*, 6, Pgs. 350- 356, (1959)
5. Carslaw H, Jaeger J, "Conduction of heat in solidification", Oxford and Clarendon Press, (1959).
6. Papazian J, Wilcox W, "Interaction of bubbles with solidification interfaces", *AIAA Journal*, Vol. 16 No. 5, Pgs. 447-451, (May 1978).
7. Fortezza R, Castagnolo D, Ceglia E, Tontodonato V, Verzino G, Monti R, "Bubble interaction with solidification front: scientific results obtained during the LMS mission.", Joint Xth European and Vith Russian Symposium on Physical Sciences in Microgravity, St. Petersburg, Russia, 15-21 June 1997.

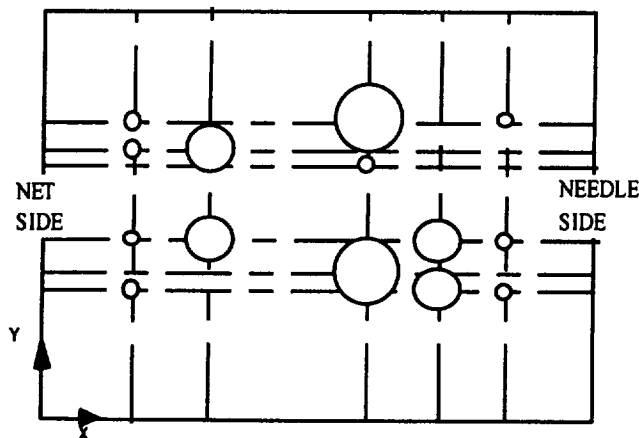


Fig. 1(a) - Initial bubble displacement, view from CCD1 camera.

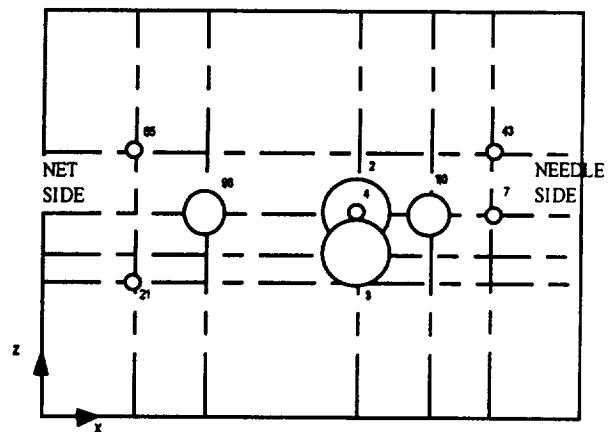


Fig. 1(b) - Initial bubble displacement, view from CCD3 camera.

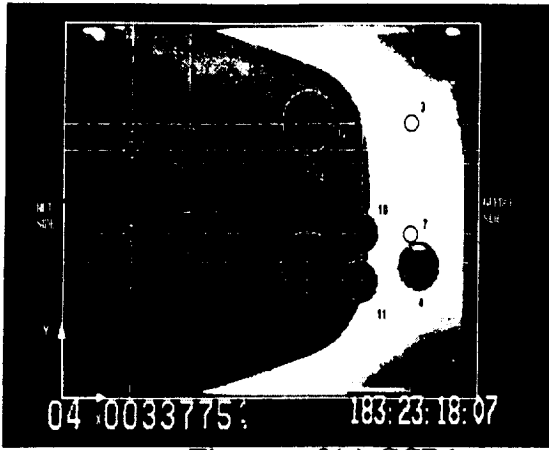


Figure 2(a)-CCD1.

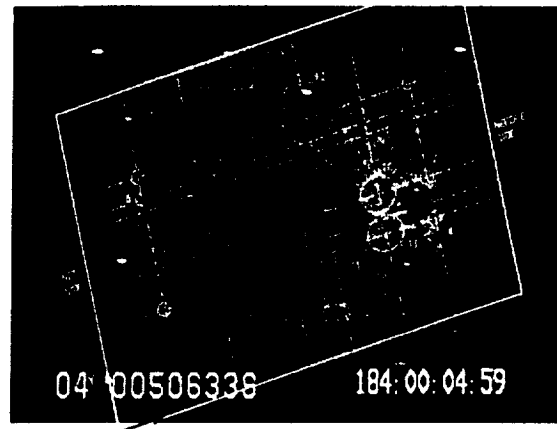


Figure 2(b)-CCD1.

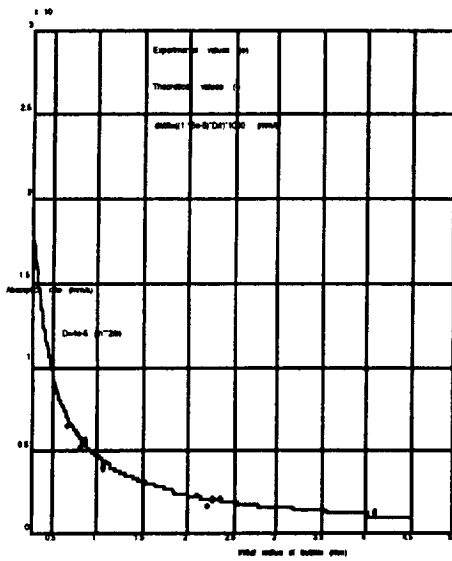


Figure 3. Theoretical vs. Experimental absorption of bubbles in liquid tetracosane.

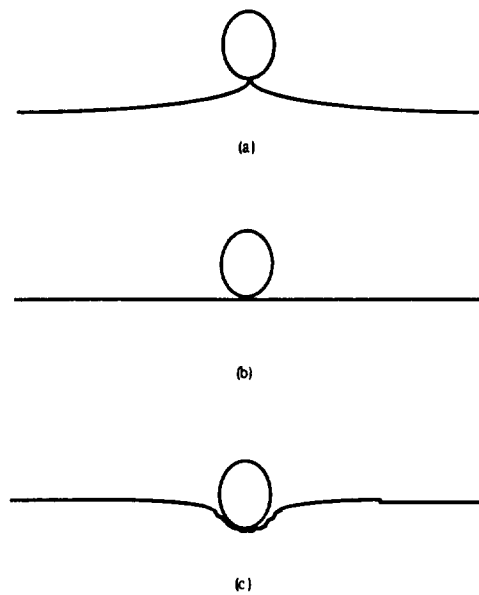


Figure 4. Theoretical interface shape for :(a) $\alpha < 1$, (b) $\alpha = 1$, (c) $\alpha > 1$.

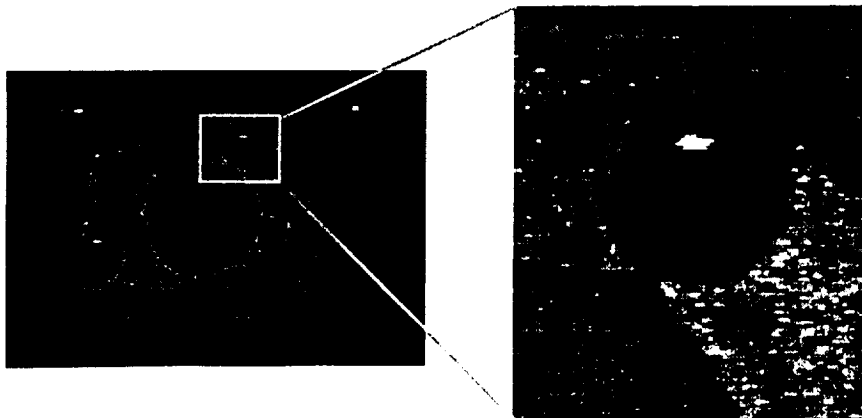


Figure 5. Interface shape at bubble/interface contact point. ($\alpha = 0.163$).

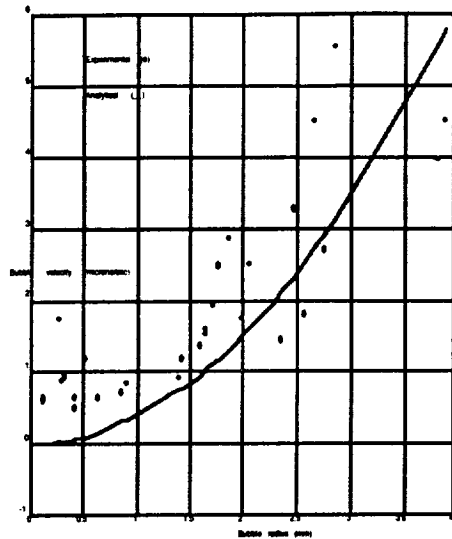


Figure 6. Comparison between analytical and experimental bubble velocities.

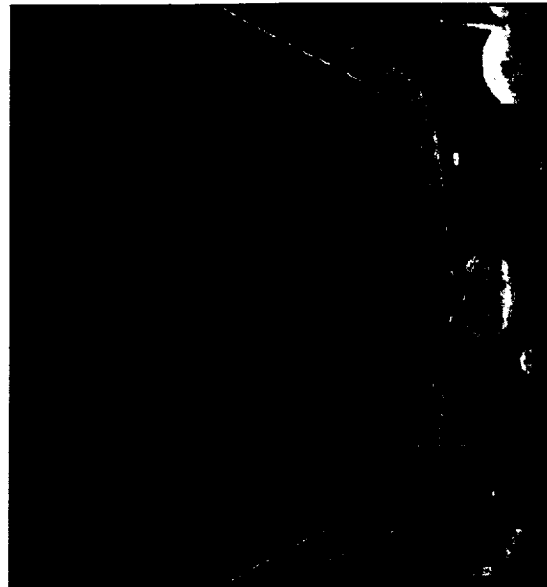


Figure 7. Superimposition of experimental and numerical images.

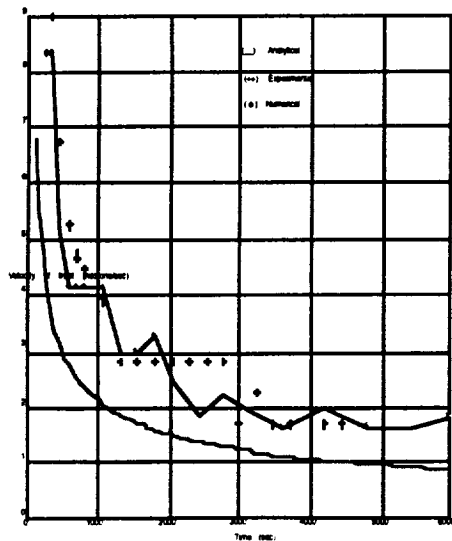


Figure 8. Analytical, experimental and numerical comparisons of front velocity.



Figure 9. Pushing and engulfing of bubbles by advancing solidification front.

Non-technical summary

Several solidification processes on ground used to produce alloys, glasses and composites are affected by the presence of undesired bubbles and droplets, that cannot be easily removed from the melt. The result is that the quality of these products is poor and should be improved. The buoyancy and sedimentation effects on-ground can be beneficial for the phase separation, but, in particular cases they are not sufficient to obtain the required purity. Alternative methods to remove these inclusions from the melt require further analysis. The afore-mentioned was the objective of the "MONTI" experiment performed in the BDPU facility flown on board of the Spacelab LMS mission. In particular the aim was to study water droplets and air bubbles inserted in a paraffine wax (Tetracosane) and to evaluate their interactions with a moving solidification front.

From these results it was possible to determine:

- How to manage the inclusions in a liquid matrix and how to remove them by using the pushing action of a moving solidification front.
- How to generate a thermocapillary force capable of displacing the solid and liquid inclusions in a established direction (called Marangoni migration)
- How to prevent the bubble inclusions in solidifying products and how to minimize the impact these bubbles have on the final product.
- How to improve the production of metal alloys, glasses, ceramics and metal matrices on Earth.

The major motivation for carrying out this experiment in a microgravity environment is that buoyancy and sedimentation effects are negligible, so that interactions between solid fronts and inclusions can be carried out without additional external forces. This environment greatly simplifies this study. An example of the negative aspects of the buoyancy effect is that it leads to an undesired distortion of the melting/solidification front and to the displacement of the inclusions.

The main conclusions drawn by this experiment are the following:

- The bubbles and droplets with diameters between 5 and 10 mm are engulfed by the front during both the melting and solidification phases of the experiment, in agreement with theory.
- Eventhough a large temperature gradient was established in the liquid phase (40°C/cm), no Marangoni thermocapillary bubble migration was observed, probably due to the surface contamination. The bubble migration which did take place was caused by the residual gravity level (0.7 μ g) experienced during the experiment, and measured by the onboard OARE accelerometer.
- The absorption of the gas bubbles by the liquid tetracosane, and the interface shape at the bubble/interface contact point confirm some of the theoretical expectations.

Further studies are required to investigate the interaction between a solid interface (both planar and dendritic) and inclusions (gaseous, liquid and solid) characterized by a very small diameter (order of few microns).

Bubble, Drop and Particle Unit (BDPU)

A Liquid Electrohydrodynamics Experiment

Principal Investigator:

Dr. Dudley Saville
Princeton University
Princeton, New Jersey

ALEX
A Liquid Electrohydrodynamics EXperiment

Report On An Experiment Carried Out On The LMS Mission
June & July 1996

Science Team

C. L. Burcham

S. Sankaran

&

D. A. Saville

(Principal Investigator)

Department of Chemical Engineering
Princeton University
Princeton NJ 08544

I. RESEARCH OBJECTIVES

The experimental foundation of electrohydrodynamics¹ - fluid motions driven by strong electric fields - is weak and the theory proposed by G. I. Taylor² (the leaky dielectric model) is relatively untested. To test the theory, experiments were carried out on the electrohydrodynamic stability of liquid bridges.

II. BACKGROUND

Electrical forces can be used to manipulate fluids by controlling the shape of an interface or exerting a body force on bulk liquid. For example, liquids can be pumped or sprayed by an appropriately shaped electric field. For apolar liquids (such as organic compounds) where the conductivity is low, relatively high field strengths (1000 V/cm) are needed. Controlling the flow of liquids in micron-scale devices is a rapidly emerging technology*. Here, the design of small scale fluid circuits depends, in part, on understanding the electrical forces and their relation to fluid motion; there are many other applications of electrohydrodynamics. Hence the need for a reliable, well-tested theory for designing apparatus. The current theory, the leaky dielectric model, was invented by G. I. Taylor² in the 1960's, but very few quantitative tests have been carried out¹. We used a liquid bridge as a venue for our experiments. One reason for choosing the bridge configuration is it's simple geometry. In addition, studying the electrohydrodynamic stability enabled us to probe aspects of the theory which had not been previously accessible.

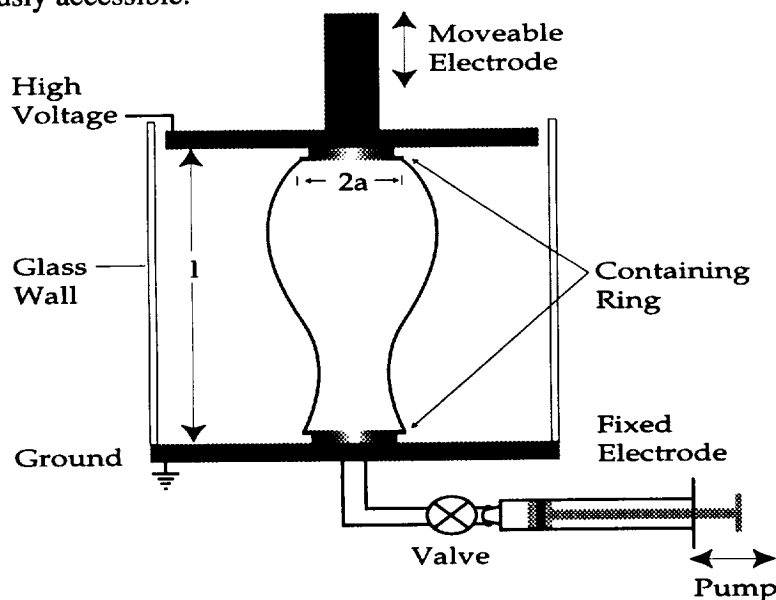


Figure 1. Schematic diagram of a liquid bridge, including features for altering the volume and imposing an electric field.

* A recent newspaper article [*U. S. I.*, January 29, 1997] reports work at Orchid Biocomputer, a company founded by the Stanford Research Institute and SmithKline Beecham. They are developing a technology for carrying out a multitude of chemical reactions on a microchip; fluid management is by electrohydrodynamic pumping.

A liquid bridge is a column of liquid pinned to a flat plate at each end (figure 1). Over a century ago, Plateau found that a neutrally buoyant bridge is stable to small perturbations as long as its length, L , is less than its circumference, πD ($2a = D$, the diameter). Thus, for stability $L/D < \pi$. Interfacial tension plays a dual role. With short bridges, small perturbations are smoothed by the action of interfacial tension. Longer bridges become unstable, also due to interfacial tension. All this derives from the amount of new surface created by a perturbation relative to that in the base configuration. Electrical forces have profound effects. Charging the bridge to bring it to a high potential makes it more unstable since the radially directed electric field opposes surface tension. Conversely, a field aligned with axis of the bridge may stabilize it. The mechanism depends on the presence or absence of free electrical charge.

Fluid bodies composed of perfect dielectric liquids can be maintained in deformed states without motion. A perfect dielectric drop deforms into a prolate spheroid in an applied field; electrical stresses balance interfacial tension on the (static) deformed interface. Non-cylindrical equilibrium bridge configurations are possible, e.g., bridges stressed by an axial field. Bridges with $L/D > \pi$ can be stabilized, up to a point; stability derives from the arrangement of polarization charge induced on the interface.

A leaky dielectric material^{1,2} behaves like a dielectric with a small conductivity. In such materials, free charge is transported by ion migration and these liquids behave as Ohmic conductors. The behavior of leaky dielectrics is quite different from perfect dielectrics because free charge congregates at interfaces due to the steep gradients in electrical properties. Thus, in contrast to the situation with a perfect dielectric, the deformation of droplet placed a steady field depends on the delicate balance of electrical, interfacial tension *and* hydrodynamic forces. A droplet of one fluid suspended in another may deform into a prolate spheroid whereas an oblate deformation ensues upon reversing the arrangement of fluids. Here the deformation and the steady shape are dynamic.

A liquid bridge offers an excellent venue for studying electrohydrodynamic stability since its location is fixed by the pinned contact lines (c.f., figure 1). Following the motion of a droplet is more difficult due to translation in the applied field³. Buoyancy plays a major role in studying phenomena with free surfaces and, in terrestrial environments, often necessitates the use of an isopycnic system with a matrix fluid surrounding the fluid body of interest. Since interfaces play major roles in electrohydrodynamics this complicates matters greatly. For example, the influence of the electrical properties of both fluids and the interface must be understood, especially processes whereby charge crosses the interface. In our LMS experiment we avoided such problems by using a gas, sulfur hexafluoride - SF_6 , as the matrix fluid. At the conditions of the experiment SF_6 behaves as a (very low viscosity) perfect dielectric gas. Neutrally buoyant liquid bridges may take on any one of three configurations: cylindrical, amphora or vase-like, and separated in to two drops. In this experiment, the transitions between these three configurations were studied.

In our experiments the behavior of a given bridge is governed by two dimensionless groups: These are: the aspect ratio, $\beta \equiv L/D$ and $\Delta \equiv a\epsilon\epsilon_0 E^2/\gamma$, which is the ratio of stabilizing electrical forces to destabilizing interfacial tension forces. The new symbols are: ϵ , the dielectric constant of the bridge fluid; ϵ_0 , the permittivity of free space; E , the field strength; and γ , the interfacial tension. The other parameters are ratios of mechanical and electrical properties which are fixed for a given fluid pair.

III. DATA ACQUISITION AND ANALYSIS

Apparatus Design and Fabrication

The LMS experiment ALEX, the acronym for A Liquid Electrohydrodynamics EXperiment was sponsored by the European Space Agency (ESA) with Daimler-Benz Aerospace as the prime contractor. Two Italian companies: Ferrari Engineering and Laben were responsible, respectively, for the mechanical design and fabrication and electrical design, fabrication and integration. Trek Engineering (USA) built the high voltage power supply. Two test containers - TC4A & TC4B were manufactured and used in the Bubble, Drop & Particle Unit (BDPU), under the overall supervision of ESTEC, the scientific and technological arm of ESA. An especially noteworthy aspect of the experiment is that only 18 months elapsed between the science concept review and the flight aboard the space shuttle Columbia. During the LMS Mission, ALEX was operated by remote control from the Marshall Space Flight Center, Huntsville, Alabama. The success of the experiment demonstrates it is possible to carry out meaningful experiments within a short time span.

Test Container Configurations

Each test container was equipped with a carousel apparatus housing three test cells. One test cell in each container contained a 2-phase mixture, similar to that used in terrestrial experiments to serve as a

Table 1: Test Container Configurations

Cell	Number of Phases	TC 4A	TC 4B
1	1	castor oil	1,000 St. silicone oil
2	2	castor oil eugenol in 12,500 St. silicone oil	castor oil in 1,000 St. silicone oil
3	1	10 X castor oil**	100 X castor oil***

* St. stands for the kinematic viscosity of the fluid measured in 'Stokes.'

** Doped with an electrolyte to raise the conductivity to 10 times that of the neat oil.

*** Doped with an electrolyte to raise the conductivity to 100 times that of the neat oil.

tie-in to ground-based work. The other two cells contained a single liquid to be suspended as a bridge in SF₆, a high field strength dielectric gas. Five of the six cells were operated successfully. In the other cell, a 2-phase cell, the bridge spilled from the retainer rings intended to hold the column in place.

Nevertheless, useful video data were obtained. Overall, nearly 20,000 video images were acquired to depict various stages of the behavior of bridges in both dc and ac fields. Analysis of the images was carried out using image analysis software developed by MARS, an ESA subcontractor. Following the mission, the hardware was recalibrated to verify the data. None of the important calibrations changed, indicating that data collected during the mission are reliable.

Experiment Sequence

The liquid bridge electrohydrodynamic experiments were conducted in a dynamic mode. For the two-phase experiments, experience with previous ground studies provided an accurate estimate of the electric fields necessary for stability. However, since there was no theory or experimental data for single-phase configurations, the electric fields necessary for stability were determined via trial and error in flight. Thus, changes in the configuration were not pre-programmed, but determined based upon the progress of the experiment.

Before a stability experiment was performed, it was necessary to form a liquid bridge. In the two-phase experiments, a short bridge (~1 mm) was created when the TC was filled prior to the launch. For the single-phase experiments, the bridge was built in orbit to avoid spilling fluid from the containing rings during the launch. The first step was to inject a drop of fluid into the containing ring on the fixed electrode. Then the movable electrode was positioned 1.5 cm above the fixed electrode and 12 kV applied. At this field strength (8 kV/cm), the drop is pulled into a shape known as a Taylor cone. Electrical forces cause fluid to be ejected from the tip of the cone towards the movable electrode where it collects inside the containing ring on the electrode. As fluid was transferred from the fixed electrode containing ring, additional fluid was added until the movable electrode containing ring was filled and a drop of fluid visible. Then the voltage was removed and the electrodes brought together until the drops on the containing ring touched and coalesced.

From this point, the single- and two-phase experiments proceeded in essentially the same fashion. The aspect ratio of the bridge was changed by moving the electrode and injecting or withdrawing fluid into the bridge at the appropriate volumetric rate so that a perfect cylinder was formed. At the outset, the aspect ratio was increased until it was close to the Plateau limit, π , and the bridge volume checked to ensure that the configuration was cylindrical. Fluid was added or withdrawn as necessary. Then the stability of the bridge at an aspect ratio just below π was investigated.

Next, the aspect ratio was increased using an electric field to maintain a stable configuration. Commands were sent in real time to increase the field since the field needed for stability was not known *a priori*. Once the desired aspect ratio was achieved, the electric field could be lowered in small steps to examine the transition from cylinder to amphora as well as the pinch-off point. Between voltage steps, the bridge was allowed to assume a steady state configuration. After the pinch-off point was identified, the voltage could be increased to re-establish the bridge. Then, further increases in the

field allowed the sequence of configurations leading to a perfect cylinder to be re-studied. Configurations were analyzed in real time using the image analysis program developed by MARS.

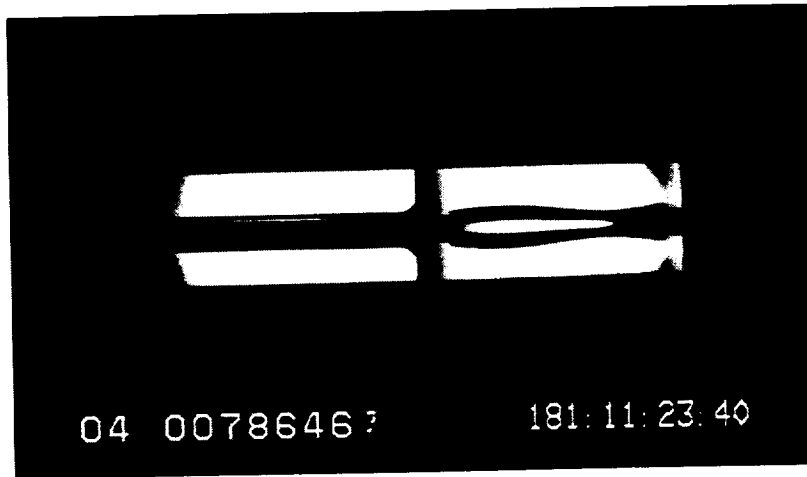


Figure 2: Digitized video image.

The image analysis algorithm produced digitized images (figure 2) and, from the edge coordinates, a trace of the bridge could be reconstructed (figure 3). The edge coordinates were also used to calculate the Fast Fourier Transform (FFT) of the shape and minimum and maximum diameters. The processes of digitization and edge detection proceeded at a rate of 2 to 10 images per second.

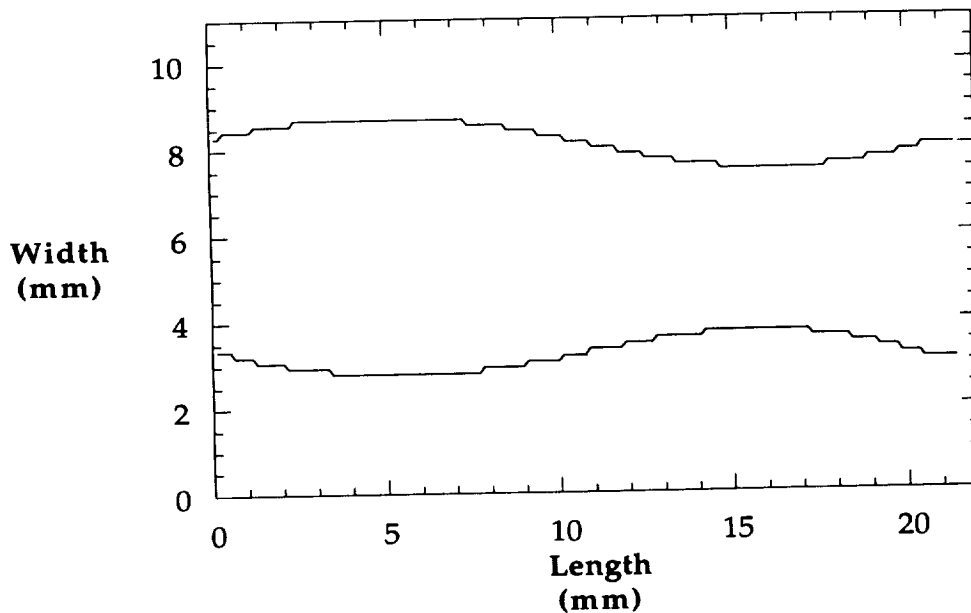


Figure 3: Reconstructed bridge shape.

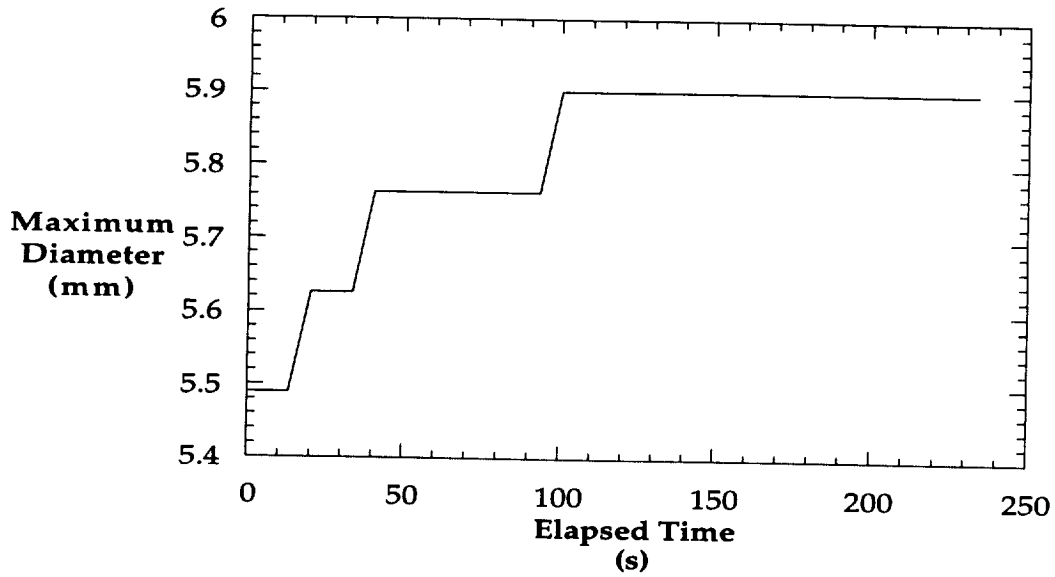


Figure 4: Maximum diameter - time relation during an experiment where the voltage was being lowered.

It was important to observe a sequence of “equilibrium” bridge shapes to identify the various configurations. Once a steady state configuration was established, the voltage was changed and shape changes monitored by following the evolution of the FFT coefficients and maximum or minimum diameter as illustrated in figure 4. A steady state configuration was defined as one which did not change in a certain period. Once steady state is achieved, the voltage was changed again and the process repeated.

Following the mission, all the image analysis was repeated in a more deliberate fashion. First, the telemetry data recorded in the ECIO data file was examined to determine when “events” occurred during the experiment. Events include changes in voltage, frequency, aspect ratio, cell rotation, or pumping. The ECIO file was used instead of the MMI files saved during the mission since they include all of the LOS data. Next, the HRM data was reformatted and saved as a series of TIFF images which were then analyzed with a modified version of the MARS Image Analysis Software. The HRM data was used over the live video recordings since it has an accompanying time stamp allowing for the synchronization of the images with the MMI data. Over 17,000 images from the HRM data were analyzed in the previously described fashion. The results of the analysis are described in the following section.

The experiments conducted during the LMS mission examined the stability of six different liquid bridges for AC and DC fields. A total of 41 different experiments were conducted in two test containers, TC 4A and TC 4B, during two separate on-line periods. The experiments involved the effects of DC and AC field levels and frequencies on the stability of bridge with different aspect ratios. Sixteen experiments were conducted the first night, and 25 the next. Each test container had two

single-phase and one two-phase liquid bridge experiment (Table 1). Four of the liquid bridges were single-phase liquid bridges; one with 1000 St. silicone oil, the other three with different electrical conductivity castor oil. The conductivity was adjusted by adding small concentrations of an organic electrolyte, tetrabutylammonium tetraphenylborate, to the castor oil. The two remaining cells were used for two-phase experiments. One of the two-phase experiments reproduced experiments previously conducted on the ground with a liquid bridge of a mixture of castor oil and eugenol in a bath of 12,500 St. silicone oil. The density of the castor oil and eugenol mixture matched that of the silicone oil to within 0.02%. The other two-phase experiment involved a castor oil bridge in a bath of 1,000 St. silicone oil.

Other than an accidental camera dislocation and a minor problem with a limit switch, the test containers and BDPU hardware performed flawlessly. Also the support teams performed magnificently. Support in the POCC by Dornier, MARS, Alenia, Teledyne Brown, NASA, and ESA was invaluable to the success of our experiment. An additional support team made up of engineers from Laben and Ferrari were on hand in Italy but were not utilized extensively during the mission -- a testament to the job done prior to the launch in fabricating and filling the test containers.

Experiments With TC4A

The first night of experiments (TC4A) occupied a 16 1/2 hour period. Cell 2 was rotated into place and examined first. The stability of the bridge without an electric field was examined at aspect ratios of 2.93 and 3.36 for comparison with ground-based work. These experiments were quite successful and will be discussed in § IV.

Next, the carousel was rotated to put cell 3 in place. The Taylor cone procedure was performed successfully creating the initial liquid bridge. Upon increasing the aspect ratio, a large gas bubble was observed in the bridge. Since the bubble was not formed during the Taylor cone procedure, it must have been trapped in the bridge fluid reservoir during filling. Attempts made to destroy the bubble by rupturing and re-forming the bridge were unsuccessful. Even though the motion of the fluid was very violent, it was not sufficient to rupture the bubble. However, this exercise did demonstrate the effectiveness of the grooved containing rings. A final attempt to break the bubble involved withdrawing fluid from the fixed electrode while the air bubble remained fixed to the movable electrode. Although the initial bubble ruptured, another formed. At this point efforts to work with cell 3 were discontinued to conserve time.

Using cell 1, a number of aspect ratios were examined for both AC and DC fields. Again the Plateau limit was probed at aspect ratios of 2.79 and 2.91. Both were stable without a field. However, at an aspect ratio of 2.96, the bridge was found to be unstable without a field - this was attributed to the fact that the volume of fluid inside the bridge was not enough to form a perfect cylinder. This result shows the importance of the real time image analysis software, which allowed us to determine the volume within a bridge both in the deformed and undeformed shape.

The aspect ratio was further increased to 3.23 where various transitions were observed with a DC field. Starting with the bridge broken at the aspect ratio of 3.23, the electric field was increased incrementally until coalescence occurred at $\Delta = 0.14$. Further increases identified the transition from amphora to cylinder at $\Delta = 0.45$. The sequence is depicted in figure 5.

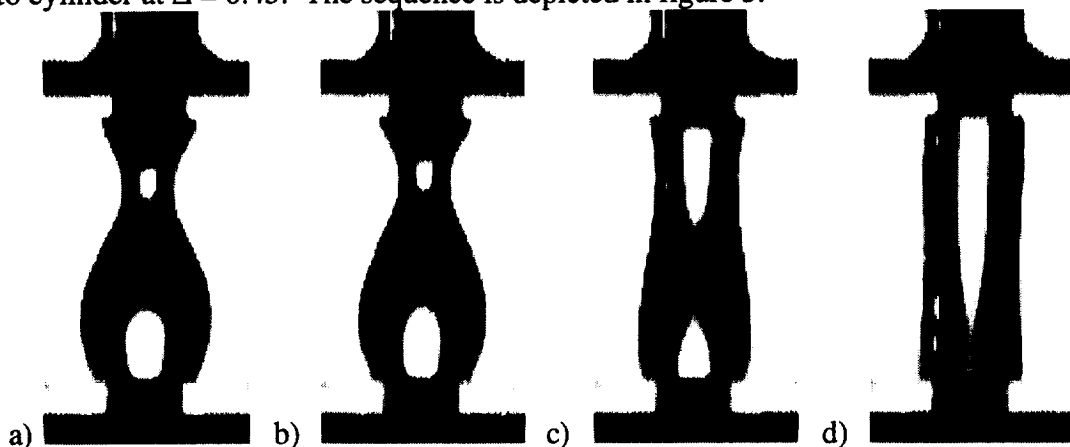


Figure 5a: Deformation of a castor oil bridge in SF_6 with an increasing electric field. Electric field parameter: a) $\Delta = 0.1423$, b) $\Delta = 0.2604$, c) $\Delta = 0.4138$, d) $\Delta = 0.4428$.

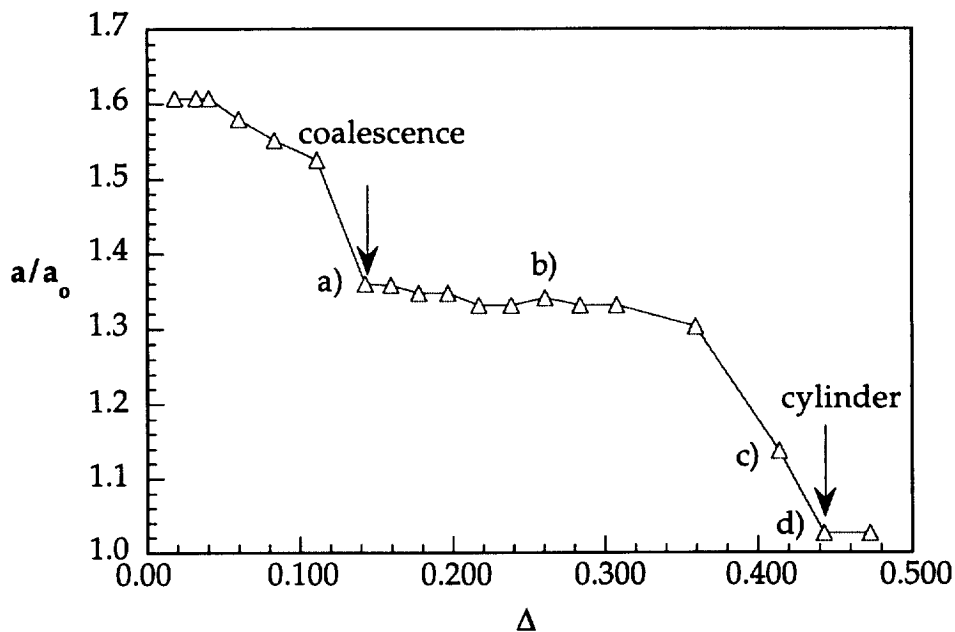


Figure 5b: Maximum bridge radius - electric field parameter relation for an increasing field. The bridge is broken until point 'a' (corresponding to figure 5a) where coalescence occurs. At point 'd', the shape of the bridge becomes a perfect cylinder.

Then, starting from a perfect cylinder, the field was lowered searching for the cylinder-amphora transition. The transition occurred at $\Delta = 0.26$ -- much lower than the transition to a cylinder. The influence of the bridge history on its final geometry was never observed in the ground experiments and was quite unexpected. The pinch-off point occurred at a $\Delta = 0.1$, very close to the coalesce point. This is shown in figure 6.

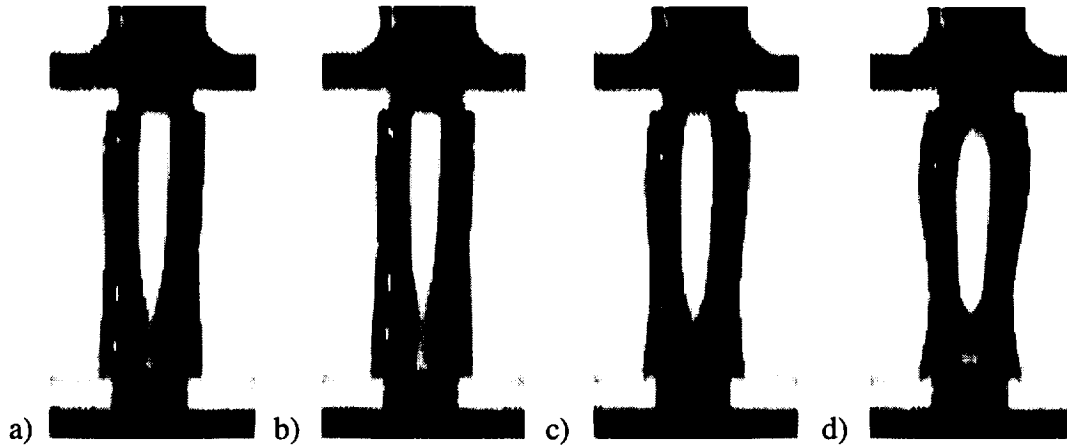


Figure 6a: Deformation of a castor oil bridge in SF₆ with a decreasing electric field. Electric field parameter: a) $\Delta = 0.4138$, b) $\Delta = 0.3325$, c) $\Delta = 0.2374$, d) $\Delta = 0.0961$.

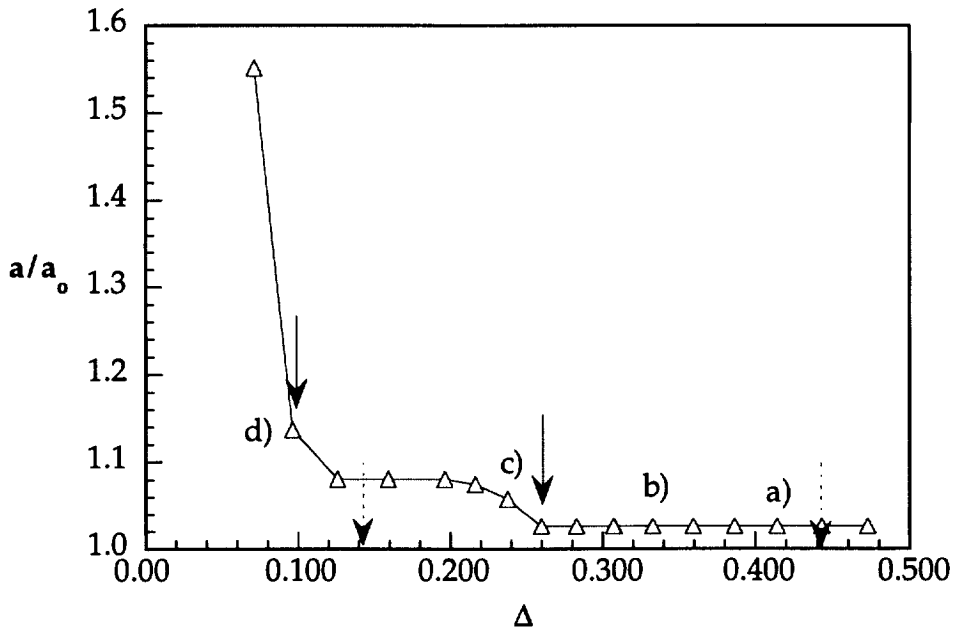


Figure 6b: Maximum bridge radius - electric field parameter relation for a decreasing field. Points correspond to configurations noted in figure 6a.

The aspect ratio was then increased to 4.32, and another DC scan performed. Starting from a broken bridge, coalescence occurred at $\Delta = 0.35$ and the transition to a cylinder at $\Delta = 0.95$. Decreasing the field exhibited the same trend as before, with the amphora transition at $\Delta = 0.6$, and pinch-off at 0.35.

An interesting behavior was observed following pinch-off. After breakup, fluid globules on each retainer ring grew into conical shapes, drew together, and reformed the bridge. Then, the bridge

collapsed and the process repeated itself many times. Such behavior is consistent with the leaky dielectric model since, when a bridge ruptures, the two parts continue to acquire charge owing to the conductivity of the oil. Eventually each globule becomes unstable and coalesces with the other forming a (deformed bridge). However, at this field strength the bridge is unstable so it breaks apart and the process starts anew.

The next set of experiments involved AC fields with the castor oil bridge, cell 3. First a bridge with a aspect ratio of 4.32 was established with a DC field. Upon switching to the AC mode at 20 kV (the highest possible voltage) stable columns could not be maintained at frequencies between 6.6 and 500 Hz. The aspect ratio was then lowered to 3.77 where a stable bridge could not be maintained at 20 kV and 30 Hz. At this point it was necessary to end operations due to time constraints. This behavior in AC fields is quite unexpected since, according to the leaky dielectric model, the bridge should behave as a perfect dielectric at frequencies in excess of the free charge relaxation time.

Experiments With TC4B

The second night of experiments (a 26 hour period) involved TC4B. Cell 1, a single-phase bridge of 1,000 St. silicone oil, was used first. Aspect ratios of 2.3, 2.55, 2.88 and 3.0 were found to be stable without an electric field. However, application of a field at $\beta = 2.88$ caused the bridge to become unstable at $\Delta = 0.8$. With $\Delta > 2.0$ the bridge was intact but oscillated without breaking. Attempts to form a stable bridge with DC fields at $\beta = 3.22$ were unsuccessful. The effects of an AC field were then tested. At $\beta = 2.88$ a broken bridge could not be reestablished using AC fields with frequencies of 200 and 10 Hz. At an aspect ratio of 3.00, increasing the field strength at 200 Hz caused to bridge to deform, but it was not unstable. Finally, a liquid bridge was stabilized with a 500 Hz field at an aspect ratio of 3.22. The transition from cylinder to amphora occurred at $\Delta = 1.55$, and pinch-off at 1.25.

The high conductivity single-phase castor oil bridge (cell 3) was examined next. A stable bridge was observed without a field at an aspect ratio of 2.25. At an aspect ratio of 3.32, the amphora - cylinder transition occurred at $\Delta = 0.45$, coinciding with that observed for the low conductivity castor oil bridge. Unfortunately, the bridge spilled from the contained rings and neither the pinch-off nor the transition from cylinder to amphora was observed. A bridge with $\beta = 3.71$ was briefly examined and found to be a stable amphora at $\Delta = 1.0$. AC experiments at 200 Hz were also conducted at an aspect ratio of 3.71. The column was unstable at 12 kV and broke spilling onto the electrodes in an unrecoverable manner.

The final cell examined was the two-phase cell (cell 2) consisting of a castor oil bridge in 1,000 St. silicone oil. Stable columns were observed at aspect ratios of 2.12, 2.82 and 3.08 without a field. A DC experiment was conducted at an aspect ratio of 3.36. Coalescence occurred at $\Delta = 0.41$. However, just as the transition to a perfect cylinder was occurring at a $\Delta = 0.98$, the column spilled. The spill was recovered, and the aspect ratio increased to 3.54. A scan from $\Delta = 1.0$ to 2.1 found that

the bridge was approaching a cylindrical shape at $\Delta = 2.1$. However, at this point the bridge began to spill again. The aspect ratio was further increased to 3.92. A stable amphora was observed at $\Delta = 11.2$.

A number of AC experiments were also conducted with the two-phase cell. Below the Plateau limit at an aspect ratio of 3.08, a perfect cylinder was observed at 200 Hz for Δ up to 0.5. At an aspect ratio of 3.36 and 10 Hz, a range of Δ 's from 0.5 to 3.1 were not sufficient to stabilize the bridge. Although, at an aspect ratio of 3.54 and 200 Hz the bridge was stabilized at $\Delta = 0.83$. Increasing Δ caused the deformation to grow. The final aspect ratio examined was at 3.92 and 200 Hz. The bridge could not be stabilized at the maximum of 20 kV. The bridge became unstable spilling in an unrecoverable manner.

Final Technical Report - ALEX A Liquid Electrohydrodynamics Experiment
IV. COMPARISON OF FLIGHT AND GROUND-BASED RESULTS

With the two-phase system, TC4A-cell 2, transitions from cylinder to amphora and the pinch-off point were found to agree closely with the results of Sankaran and Saville⁴ after taking account of the difference between the properties of the two system (Figure 7). The transition from cylinder to amphora occurred at $\Delta = 0.195$, and pinch-off at $\Delta = 0.057$. This compares to the values of $\Delta = 0.18$ and 0.03 reported by Sankaran and Saville³ for the transition and pinch-off points respectively. This agreement between μ -g and 1-g experiments validates the performance of the flight system for steady fields.

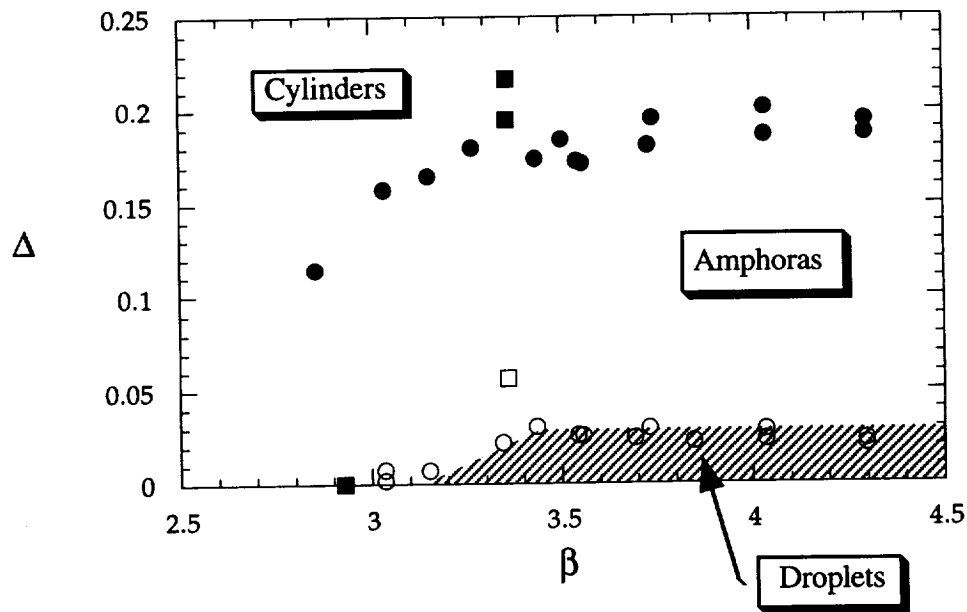


Figure 7. A comparison of flight and ground-based results in a two-phase system.
● & ○ - terrestrial experiments; ■ & □ - μ -g experiments.

V. COMPARISON OF EXPERIMENT AND THEORY

At the time of the experiment the leaky dielectric model had not been used to predict the behavior of a pinned bridge. Since that time, Mr. Chris Burcham has completed calculations⁵ to predict the stability of a liquid, leaky dielectric bridge in a dielectric gas. A comparison between experimental results for a castor oil bridge and theoretical calculations are shown in figure 8. Although the agreement between theory and experiment for pinch-off is encouraging, it is unexpected since the theory presupposes small perturbations. On the other hand, the lack of agreement for the cylinder-amphora transition is vexing. Two causes, other than the approximations involved in linearization, come to mind. First, it is possible that the bifurcation from cylinder to amphora is continuous, rather than abrupt as suggested by the theory. Another possibility is that the leaky-dielectric model itself is flawed. A large number of approximations are inherent in the model¹ and one or more of these may be at fault. These matters remain under investigation.

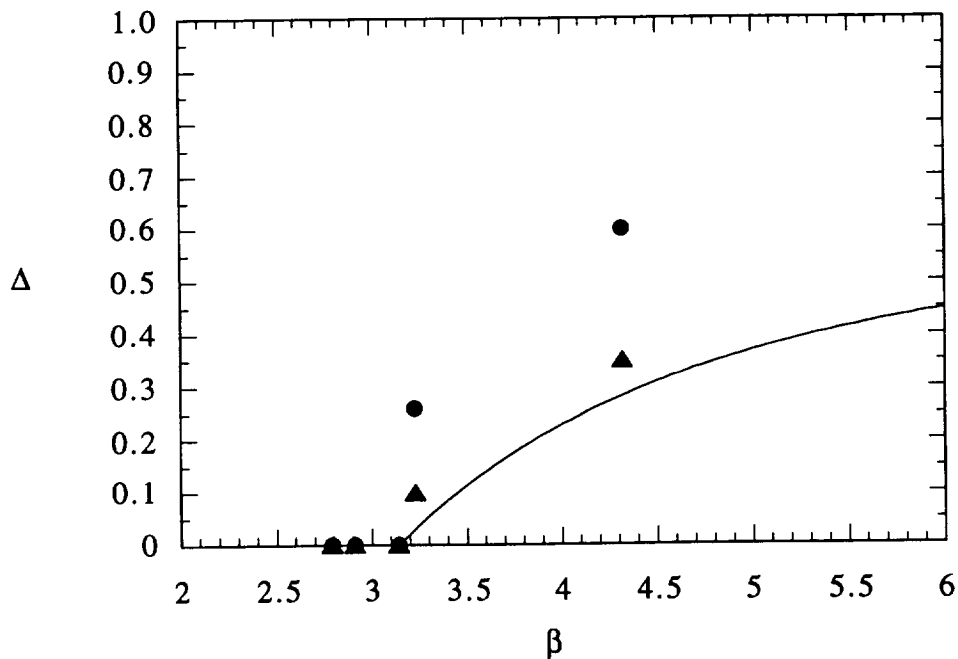


Figure 8. Comparison between theory⁶ and experiment for a castor oil bridge in an SF_6 environment. The solid line is a theoretical result for the stability of a liquid bridge subject to small perturbations. States above the line are stable; those below the line are unstable. The experimental points were obtained in experiments during the LMS mission - TC4A, cell 1: ● - cylinder-amphora transition; ▲ - amphora - drop transition ('pinch-off').

VI. SUMMARY & CONCLUSIONS

The ALEX apparatus performed as designed and produced a considerable amount of useful data. The primary goal, to test the leaky dielectric model in the liquid bridge configuration, was achieved. As with any successful scientific experiment, as many new questions and ideas were raised as were answered. Thus, the ability of the model to address issues of stability with a gas-liquid interface in DC fields was demonstrated. Theory and experiment appear in agreement, although some questions remain.

The situation with AC fields is less clear. According to the theory, leaky dielectric materials should behave as perfect dielectrics if the frequency is high enough. Thus, a bridge which can be stabilized by a DC field should be stable in a AC field, albeit at a higher field strength. This was not generally the case in our experiments. Accordingly, additional work with this aspect of the model is needed to elucidate the behavior of leaky dielectrics in AC fields.

VII. NON-TECHNICAL SUMMARY

Many aspects of modern technology involve miniaturization; witness the proliferation of computers and other micro-electronic devices. However, there is another class of problems which can be addressed if one can control minute flows of liquids - devices currently under development carry out a multitude of chemical reactions in tiny reactors lodged in silicon chip. Moving liquid to and from the reactors is done with electrohydrodynamic forces. The design of such devices as well as other applications relies, in part, on having a well-established theory which describes the performance of the pumps and fluid circuits. The theory behind the electrohydrodynamic pump is called the leaky dielectric model. ALEX, the experiment conducted on the LMS mission, was designed to provide data to test and improve the theory. The experiment itself involved studying the motion of a column of fluid in the presence of an electric field. It was very successful and showed where the theory is strong as well as identifying areas where improvement is needed.

VIII. BIBLIOGRAPHIC CITATIONS

1. C. L. Burcham & D. A. Saville 'Electrohydrodynamic Stability of Liquid Bridges' AICHE Annual Meeting, Chicago, November 96.

IX. BIBLIOGRAPHY

¹ D. A. Saville 1997 Electrohydrodynamics: The Taylor-Melcher leaky dielectric model *Annual Review of Fluid Mechanics* **29** 27-64.

² G. I. Taylor. 1966 Studies in electrohydrodynamics I. The circulation produced in a drop by an electric field. *Proc. Roy. Soc.* A291:159-66.

Final Technical Report - ALEX A Liquid Electrohydrodynamics EXperiment

³ O. Vizika & D. A. Saville 1992 The Electrohydrodynamic Deformation of Drops Suspended in Liquids in Steady and Oscillatory Electric Fields. *Journal of Fluid Mechanics* **239** 1-21.

⁴ S. Sankaran & D. A. Saville 1993 Experiments on the stability of a liquid bridge in axial electric field. *The Physics of Fluids A* **5** 1081-1083.

⁵ C. L. Burcham 1997 Ph.D. Thesis, Department of Chemical Engineering, Princeton University.

Bubble, Drop and Particle Unit (BDPU)

**Boiling on Small Plate Heaters under Microgravity and a
Comparison with Earth Gravity**

Principal Investigator:

Dr. Johannes Straub
Technical University Munich
Munich, Germany

BOILING ON SMALL PLATE HEATERS UNDER MICROGRAVITY AND A COMPARISON WITH EARTH GRAVITY

J. Straub, M. Steinbichler, G. Picker

Lehrstuhl A für Thermodynamik, TU München
Boltzmannstr. 15, 85748, Garching, Germany

M. Zell

DASA GmbH, Dornier
88039 Friedrichshafen

ABSTRACT

The boiling heat transfer on five miniature heaters of different size and shape has been measured under microgravity conditions during the LMS mission and under earth gravity after the mission in 1996. These experiments were conducted as basic studies of boiling heat transfer in microgravity and as simulations for the direct emerging cooling of small electronic devices by boiling heat transfer, which becomes more and more important due to high thermal loads of modern electronic components.

The boiling process was studied in the liquid FREON 123, which was considered as an alternative refrigerant which is not endangering the ozone layer. The boiling heat transfer was determined by a simultaneous measurement of the heat-flux and the temperature of the heater. The boiling process was observed in two perpendicular observation directions with different types of optical diagnostics, provided by the BDPU facility.

Several boiling modes, like cavitation and sparkling boiling, as well as the cavitation thermocapillary supported flow-mode, thermocapillary jet boiling and saturated boiling have been observed during the experiments, depending on the subcooled liquid state and the overall heat flux. Under microgravity surface tension driven convection plays an important role in the boiling heat transfer on the miniature heaters. The observations under earth gravity show significant differences especially in terms of bubble size, departure diameter and induced flow-pattern. Astonishingly a remarkable influence of the gravity level on the heat transfer could not be measured. That confirmed earlier observation that the evaporation in the liquid wedge between the solid heater and the bubble interface, the capillary force, the surface tension and the wetting condition play the most important role in the boiling process.

INTRODUCTION AND OBJECTIVES

During the LMS Spacelab mission of NASA in July 1996 pool boiling experiments under microgravity conditions were performed. These experiments are utilized five different small sized and shaped thermistors. These thermistors were used simultaneously as heating elements and as resistance thermometers. Three of these five heating elements were plate shaped with the diameters of 3, 1.5 and 1 mm, respectively. The other two heating elements were thermistor beads, with nearly spherical diameters respectively 1.4 and 0.4 mm. The experiment called BOIL „ A simulation for the cooling of small electronic devices“ /1/ was accomplished in the BDPU (Bubble, Drop and Particle Unit), which was a Spacelab multi-user

facility for fluid physics experiments, operated by the European Space Agency, ESA. This facility was already used during the IML-2 mission in 1994.

This boiling experiment was conducted together with a second experiment called NUBUC „Study of vapor bubble growth in a supersaturated liquid“ /2/, utilizing the same hardware, which was designed and build according to this purpose. The original planning foresaw an equal sharing of the available microgravity time for both of the experiments. However a major share of the available microgravity time was used for the boiling experiment, whose primary results will be discussed on the following pages. Thanks to the replanning efforts of the NASA team from the MSFC Operation Support Center in Huntsville, AL, additional time for both experiments was available. After disintegration from the Spacelab the experiment was repeated on ground with the flight hardware, the identical fluid, and the same

experimental sequences, in order to guarantee comparable boiling data both under microgravity as under earth gravity.

The scientific objectives of the boiling experiments were the following:

- a) A study of the primary mechanisms of pool boiling on five different sized and shaped microheaters under excellent microgravity conditions and a comparison of the microgravity data with reference data gained under comparable conditions under normal gravity.
- b) A observation typical dynamic processes as bubble formation, growth, departure, departure diameter, and coalescence, in order to determine the influence of the gravity level on these dynamic processes.
- c) The separation of gravity dependent and gravity independent mechanisms on the boiling process.
- d) The investigation of the heat transfer coefficients for very small plate shaped and hemispherical microheater under microgravity and normal earth gravity.
- e) The study of the influence of the size and shape of the heating element on the overall heat transfer coefficient under microgravity and normal earth gravity.
- f) The acquisition of a large data base of boiling data for the development of new correlations for the boiling heat transfer under microgravity.
- g) A comparison with the boiling data gained during IML-2.
- h) A study of the feasibility of boiling heat transfer, using this technique for the cooling of high powered microelectronic components directly immersed into a liquid and its application in space and on earth.

APPLICATION

The performance of integrated circuits and high powered electronical components was enhanced considerably during the last years. This increase was mostly combined with an decrease in size. This causes serious problems, because most of the electric power disperses into expense heat, which must safely be transferred from the electronic component, in order to protect from overheating and possible destruction. As protection from any critical overheating, an efficient and stable method of cooling must be found and applied. One of the most promising methods is boiling heat transfer in dielectric liquids. Several authors /3-6/ investigated boiling heat transfer on integrated circuit chips or simulated microheaters that were directly immersed into a pool of liquid. These liquid pools were normally environmentally safe refrigerants, with appropriate vapor pressure curves. These experiments were performed under earth conditions, where the buoyancy and the buoyancy induced convection supported the vapor and heat transport away from the heater.

Naturally our main interest lied still, in spite of possible future technical applications, mainly in the basic fundamentals of the boiling process and its mechanisms. Former experiments /1,8,11/ demonstrated that the applied correlations loosed their validity quickly, if they were extrapolated to higher or lower gravity level. Therefore it was justified to ask whether gravity

really should be considered the dominant mechanism of the boiling heat transfer process.

BACKGROUND

In contrast to existing theories and correlations e.g. /10/ former boiling experiments with various geometries under microgravity /8/ demonstrated clearly that the influence of gravity is much less as predicted. However, for these experiments large heating elements were used, therefore no information existed about very small heaters. For large heating elements it was obvious that the temperature and heat flux measured was only an integral value, which neglected local and spatial variations in temperature and heat flux due to bubble dynamics. Therefore the usage of small heating elements promised a considerably better information about the boiling phenomena encountered, because the measuring resolution is higher.

Other authors e.g. /12/ predicted that under the absence of gravity a small heating element should immediately be covered with vapor, leading to film boiling and corresponding with it to high heater temperatures, since buoyancy is the driving force of vapor removal from the heating surface. Hence the question arised, if the boiling process can still be a suitable mechanism for an efficient cooling of small electronic elements under microgravity? Future application of the boiling process for cooling of electronical components in space applications and on earth depended from a solution to this question.

EXPERIMENTAL EQUIPMENT

BDPU Facility

During the LMS Spacelab mission on STS 78 the experiment was conducted in the ESA multi-user facility BDPU (Bubble, Drop and Particle Unit), designed by ALENIA, Italy. Multi-user facility meant that it could be used for a wide variety of specific scientific needs. The BDPU provided the power supply, data acquisition and two perpendicular observation directions, with a wide variety of optical devices like background illumination, two different types of interferometers, a point diffraction and a wollaston interferometer and a light sheet for the study of flow fields with particle image velocimetry. Each observation path was recorded by a video camera or an extra 16 mm film camera. Furthermore the BDPU provided the interface to the Spacelab and the Shuttle system for the video and data link direct to the Operation Support Center at the NASA-MSFC in Huntsville. There, the principal investigators and their teams could observe the experimental runs during the mission in real time video and all important experimental data were directly available. The experiments in the BDPU were controlled by telecommanding from ground and the essential experimental parameters were adjusted depending on the observed data. This system ensured that a maximum of scientific results could be obtained.

Test Container

The test container was refurbished from the test container used during IML-2 according to the new requirements of the experiment by the companies Daimler Benz Aerospace, Dornier, Germany, in cooperation with Ferrari Engineering, Italy. The container was set in the facility and electrically connected by one of the astronauts. It had the size of 45x15x30 cm³. Because of safety reasons the container had a triple containment. It had to be ensured that in case of a leakage of the fluid system no gas of the evaporating liquid was released into the Spacelab environment. The liquid cell had an internal dimension of about 50 x 50 x 50 mm³ with a nearly spherical shape on the inside. It had four windows of sapphire with 40 mm optical diameter for the two perpendicular observation directions. To change the pressure of the liquid in the test cell and to compensate the vapor volume in order to keep the pressure constant during boiling a bellows was used with the counter pressure imposed by nitrogen. A small gas compressor supplied a small pressure vessel with the necessary compressed nitrogen, to guarantee the counter pressure on the liquid side of the bellows. By the means of two valves on the nitrogen side of the pressure system the pressure inside the fluid cell could be adapted to its appropriate value.

Two Peltier elements on the lateral walls of the fluid cell were used simultaneously for heating or cooling. The temperature could be controlled within ± 0.05 K. The Peltier elements dissipated the heat to the avionics air duct through two heat pipes. The test liquid in the fluid cell was FREON R123, which had replaced the environmental endangering FREON R11. Nine identical small sized thermistors were directly placed in the liquid to measure the liquid temperature distribution in the vicinity of the heating elements. Originally three plate heaters and three spot heaters were additionally placed inside the test cell. Unfortunately the smallest spot heater was already damaged beyond recovery during the first experiment run at the beginning of the mission. The plate heaters were circular with the diameters of 3, 1.5 and 1 mm. The remaining spot heaters of nearly spherical size had a bead diameter of 1.4 and 0.4 mm. As an example for one of the spot heaters see Fig. 1

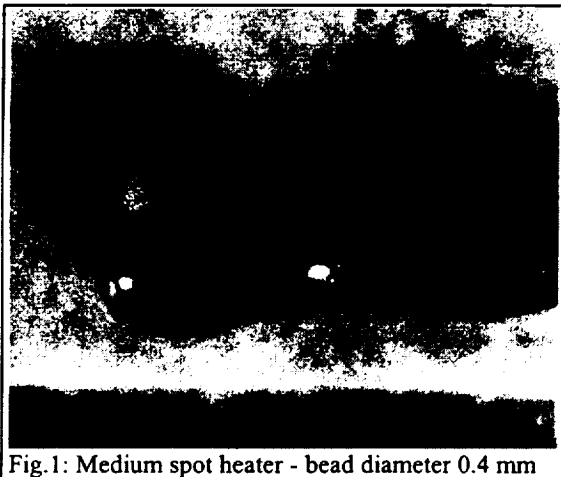


Fig. 1: Medium spot heater - bead diameter 0.4 mm

These thermistor used as heaters had a special temperature-resistance characteristic, which was determined well before the mission. The thermistors themselves were covered by a glass coating in order to protect the semi-conductor material, which provided the necessary resistance characteristic. The plate heaters were designed as circular copper plates with a thermistor glued into, with a special glue of high thermal conductivity. These copper plates were integrated in a basis material characterized by a high melting point and low thermal conductivity, in order to minimize loss of heating power due to conduction in the material. However, because of the glass coating the temperature measured was not equal to the wall temperature, which determined the nucleation temperature and the evaporation of the liquid. Therefore the real wall temperature had to be calculated from the power input and the measured inner temperature during the evaluation stage of the data.

The spot heaters and plate heaters could be controlled with constant temperature as well as constant power. Constant temperature meant that the heat flux adapted according to the physical circumstances of the boiling state with a constant superheat, whereas constant power meant that the wall temperature adapted to the physical circumstances with the power dissipation held constant. This adaptation was influenced by the pressure level, respectively the fluid state and the heat transfer coefficient of the boiling process. Each experiment run with different heat fluxes or temperatures was conducted at a constant fluid temperature and pressure level. Afterwards the boiling run was repeated at the same liquid state with another heater. Whenever five boiling curves for the available five heaters were acquired the fluid state was changed and the whole procedure started again.

During the evaluation stage the appropriate wall temperature T_w had to be calculated from a steady-state conduction equation. Since all thermistors were nearly spherical the heat conduction equation simplified to one-dimensional steady-state conduction. With the power input to the thermistor \dot{Q} , determined by the voltage and current at the heater and the inner temperature T_i of the heater according to its resistance characteristic the real wall temperature could be calculated according to following equation

$$\dot{Q} = \frac{T_i - T_l}{R_l + R_\alpha} \quad (1)$$

where T_i is the inner temperature of the thermistor, T_l is the bulk liquid temperature recorded in the cell, R_l is the thermal conductivity resistance of the thermistor coated with glass and could be determined, if the geometry was assumed spherical and the inner diameter r_i of the semi-conductor, and the outer diameter r_o of the glass coating were known

$$R_\lambda = \frac{(r_o - r_i)}{\lambda_g 4\pi r_i r_o} \quad (2)$$

This assumption is justified because in the case of pure heat conduction to the liquid at lower heater temperature a nearly spherical temperature field was observed in the interferometer.

The heat transfer resistance R_α to the liquid was given by

$$R_\alpha = \frac{1}{\alpha 4 \pi r^2} \quad (3)$$

With eq. (1) the total thermal resistance $R_\lambda + R_\alpha$ of the thermistor was determined, and respectively with eq. (3) the heat transfer coefficient α . The wall temperature on the outside of the glass coating of the thermistor T_w could be determined as:

$$T_w = T_i - \dot{Q} R_\lambda \quad (4)$$

The heat loss to the cylindrical not heated part of the thermistor was calculated as a fin and is proportional to $T_i - T_f$. The heat losses were considered in the calculation of the heat flux. These calculations were valid for all of the heaters as long as spherical or nearly spherical geometries were considered and the appropriate geometrical dimensions and thermal properties were used. Concerning the plate heaters, which were thermistors glued into copper plates further thermal resistance has to be considered. However since the thickness of the copper plate was very small and the thermal conductivity of copper was about 400 times higher than the thermal conductivity of the glass coating of the thermistor, the influence of the copper could be neglected within reasonable accuracy. Nevertheless heat losses due to dissipation into the basis material, the copper plates were integrated in, were considered in the calculations. These simplification were backed by the readings of a very tiny measuring thermistor (bead size 0.05 mm) which was assembled in the copper mantle of the large plate heater (3mm diameter), which showed good agreement between the calculated and measured wall temperatures.

EXPERIMENTAL PROCEDURE

The temperature of the fluid cell was set to the desired value, and while stirring the liquid in the test cell was heated up to the set temperature. After the set temperature was reached the pressure level was adapted according to the desired subcooling or saturation. Then the stirrer was switched off and the movement of the liquid calmed down within 2 minutes.

Then the chosen heater was either controlled in constant temperature or constant power. The heater inner temperature or power dissipation was slowly increased in 10 steps up to the maximum value. After the maximum level was reached the power/temperature was then slowly decreased in fifteen steps until the beginning state was reached again. The maximum power and inner temperature levels of each heater varied according to their sizes and resistance characteristics. Since for every experiment run the number of changed parameters was about 40 parameters a special software was developed, to simplify and to quicken the changing process.

The power dissipation \dot{Q} and the inner temperature T_i were measured during the whole experimental run. At each temperature / power level the boiling process was maintained for about 20 seconds. The measured data clearly showed that

this time interval was easily enough for steady state conditions at the heater surface, since the steady state conditions were reached after approximately two seconds.

All measurement data was recorded with a frequency of 8 Hz and linked down directly to the control center of MSFC in Huntsville.

The experiment controlling software consisted of three boiling runs, which were conducted with three different heaters. After completion of the three boiling runs, a new run with the other two heaters was completed. The pressure was raised up to 14 bar in order to condense any excess vapor. A new pressure/subcooling level was adjusted and again the five boiling runs were completed. After completion of all the desired pressure levels at one fluid state, a new fluid temperature value was set and everything started over again. The measured boiling curves normally started with pure conduction until the necessary nucleation wall temperature was reached, then the boiling process set in. Unfortunately almost at no fluid state the critical heat flux condition could be achieved. This fact is mainly due to the high thermal resistance of the glass coating of the heating elements. Therefore mostly only nucleate boiling curves could be measured.

PRELIMINARY RESULTS

Boiling Sequence

The experiments were carried out at constant bulk liquid temperatures $T_f = 30, 40, 50, 70, 80, 90, 100, 110$ °C and at various thermistor inner temperatures T_i and power levels \dot{Q} . The maximum achievable inner temperature T_i was averagely

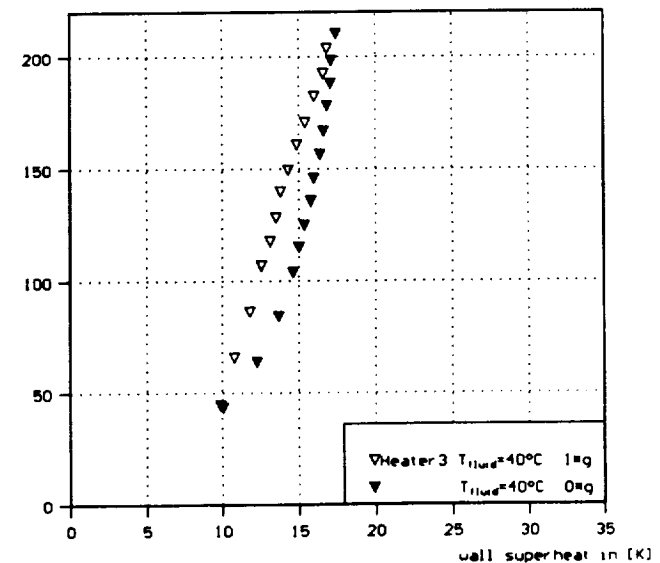


Fig. 2 a: Heat flux versus the superheat at the small plate heater

250 °C, depending on the resistance-temperature characteristic of the heater. The maximum power dissipation \dot{Q} of the heaters ranged from 0.8 W for the larger heaters and 0.3 W for the smaller ones.

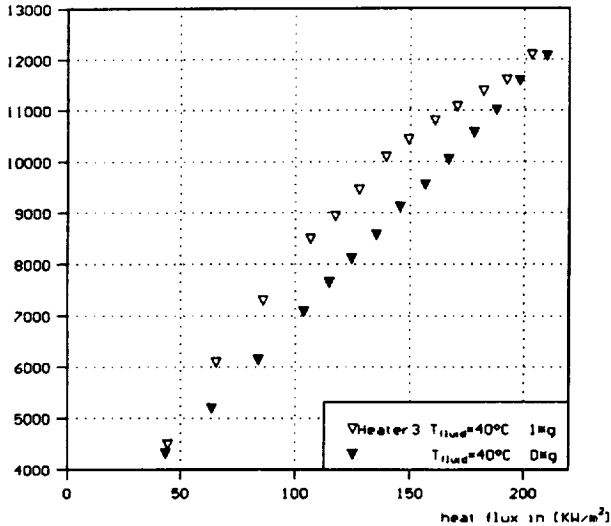


Fig. 2. b: Heat transfer coefficients versus the heat flux at the small plate heater

smaller ones.

During the course of one experimental sequence three boiling curves were done at one predefined fluid state and pressure level. One boiling curve consisted of 20 different temperature or power levels. Each temperature or power level was held constant for at least 20 seconds. The measured voltage and current at the heaters clearly show that this waiting time was more than enough for steady state conditions at the heaters. The steady state conditions were reached in a time interval of maximal two seconds.

In Fig. 2a and b the results of a conducted experimental sequence for one of the plate heaters at saturation pressure and fluid temperature of 40 °C are shown as an example. Fig. 2a shows the time averaged heat flux \dot{q} versus the wall superheat, respectively the difference of the wall temperature and the saturation temperature of the liquid ΔT_{sat} . Since the pressure level equaled the saturation pressure at a fluid temperature of 40 °C, the saturation temperature was 40 °C. Fig. 2b shows the averaged heat transfer coefficient α , defined with the temperature difference between wall and saturation temperature, versus the heat flux \dot{q} . Also included in Fig. 2a and b are the reference measurements conducted on earth. For the reference measurements the identical hardware and the same refrigerant had been used. Additionally the reference experiment runs were conducted with exactly the same heater temperature and power levels, in order to guarantee the reproducibility of the measured reference data.

It can be clearly seen, that a remarkable influence of the gravity level cannot be identified. The averaged microgravity data points are shown with closed symbols, whereas the averaged

reference data points are shown with open symbols. Considering the shape of the boiling curves it is easy to see that both the microgravity data and the reference data show the same qualitative tendency. This strongly indicates that even without the presence of gravity induced buoyancy still the same hydraulic and thermodynamic forces are responsible for the boiling process. Therefore considering the buoyancy a primary mechanism of the boiling process cannot be contained.

Heat Transfer

Saturated liquid state:

The heat transfer for saturated liquid conditions under microgravity (full symbols) at the fluid temperatures of 40°C, 60 °C and 80 °C is shown in Fig. 3. together with the

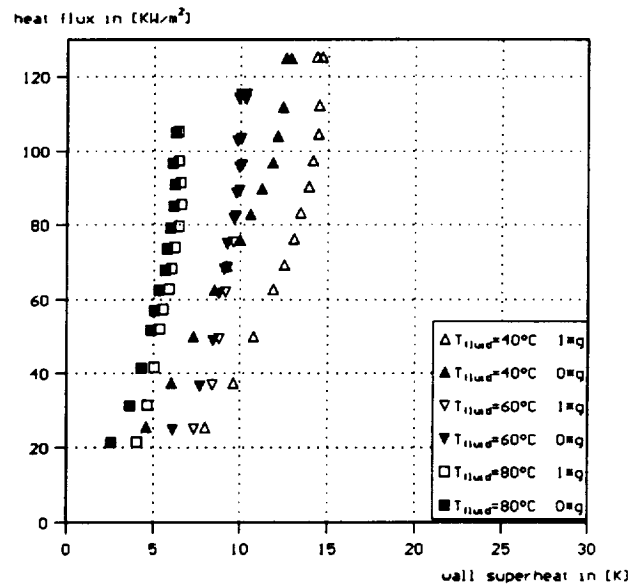


Fig. 3: Saturated Boiling on the Large Plate Heater

corresponding normal earth gravity data (open symbols) for the large plate heater.

The appropriate boiling curves shifted with increasing pressure level from 40°C to 80°C to lower superheating, averagely from 15 K to 8 K. This fact was in good agreement with the existing theories, which predicted lower necessary superheats with increasing system pressure. The comparison of the microgravity nucleate boiling curves and the normal gravity nucleate boiling curves yielded interesting results. At each fluid temperature of 60 °C and 80 °C the heat transfer under microgravity showed almost no difference to the heat transfer under normal gravity. At the saturation fluid state of 40 °C the heat transfer coefficients under microgravity were even up to 20-30 % higher compared to the reference heat transfer coefficients measured on earth. This indicated that the heat transfer under microgravity was more efficient. These observation confirmed our previous findings /8,11,13/ that the influence of the gravity level in the nucleate boiling regime is neglectable.

In any case it is obvious that the influence of the gravity level on the heat transfer is not correlated very well by equations developed for boiling heat transfer under earth gravity. The usage of the well known correlation from Rohsenow /9/ at the same fluid states, heater geometries and at same heater conditions yields the following influence of system acceleration, respectively the gravity level.

$$\frac{\dot{q}_{\mu g}}{\dot{q}_{1g}} = \left(\frac{a}{g}\right)^{\frac{1}{2}} \quad (5)$$

Measurements during the shuttle flight showed that the average residual gravity a/g is about 10^{-4} and lower. Equation (5) predicts that the heat flux therefore should decrease to 1 % of its normal gravity value. The boiling curves clearly show that this was not the case at all, even for the small geometries. Therefore it seemed that probably the interfacial tension and the wetting characteristics are the more dominant mechanisms than the gravity induced buoyancy and can replace the buoyancy induced convection easily. A more detailed discussion of these effects can be found in /8,11/. In case of the boiling curve at 40°C it also seems that the gravity hems the heat transfer process somehow. This could be explained with the following fact. Due to the absence of buoyancy induced convection the thermal boundary layer under microgravity at the heaters surface is thicker compared to earth gravity and the superheat higher. Therefore the boiling process under microgravity sets in at lower heat fluxes, since the excess heat has to be transported by pure conduction. Therefore while under earth gravity conditions the heat transfer is still managed by convection and conduction, under microgravity boiling is already established. This could explain why the heat transfer coefficient is higher under microgravity in the region of low heat fluxes. Concerning higher heat fluxes, where both under microgravity and earth gravity the boiling process is established, the better heat transfer can be explained by the heater area, the boiling process takes place on. Since under normal gravity the excess heating power is transferred to the surrounding liquid by evaporation and conduction, certain local surface areas are still not in the nucleate boiling regime. In contrast to this almost the complete surface area under microgravity is affected by the vigorous boiling process. Taking all this into account a slightly higher heat transfer coefficient at higher heat fluxes under microgravity could be explained.

Subcooled liquid state:

For the saturated liquid state at 70 °C the subcooled boiling heat transfer data has been evaluated for the large plate heater along the isobaric line of $p = 3.79$ bar (corresponding to 70 °C saturation state), Fig 4.

With increasing liquid subcooling the wall superheat $\Delta T_{s,at}$ was reduced, as predicted by theory. Again the heat transfer coefficient under microgravity and normal earth gravity showed no remarkable deviation. In contrast to the saturated liquid states the light sheet and the interferometric images showed that under microgravity with increasing subcooling of the liquid a strong thermocapillary flow developed, which supported the heat removal away from the surface of the heater, see Fig 5.

Therefore it seemed that under subcooled conditions other mechanisms on the boiling process besides the interfacial tension and the wetting characteristic became important. The

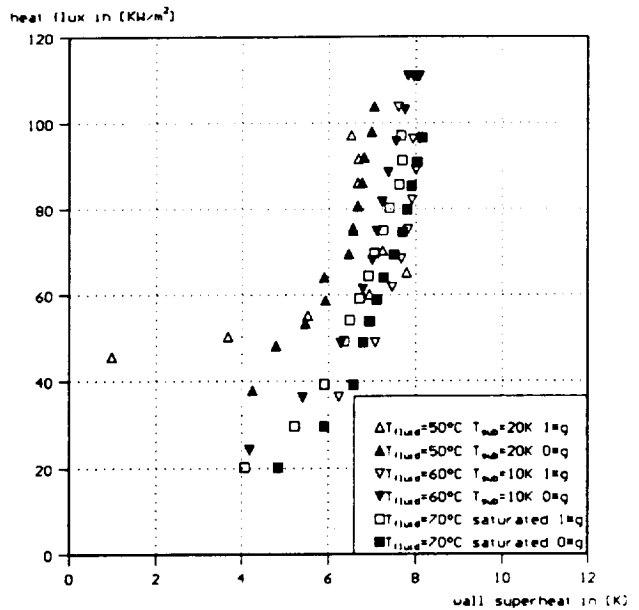


Fig.4: Subcooled boiling on the Large Plate Heater

development of this thermocapillary flow originated in surface tension gradients from the bubbles base to the bubble top, and was totally independent of gravity.

Resulting from the experiments it can be stated that the gravity induced buoyancy still is not the primary mechanism responsible for the boiling process. In subcooled liquid states this strong thermocapillary flow could be one of the reasons for the not predicted efficient heat transfer. Further evaluation of the particle image velocimetry, which are under evaluation right now should improve the understanding of the importance of this

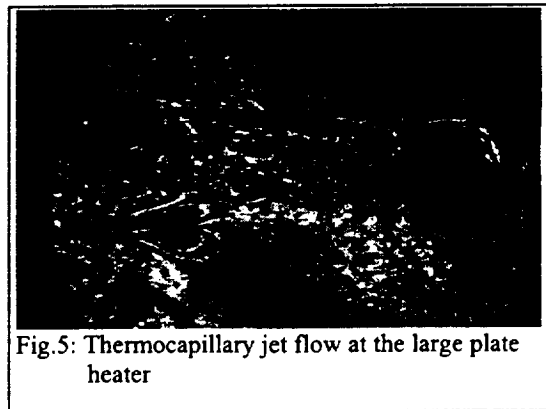


Fig.5: Thermocapillary jet flow at the large plate heater

thermocapillary flow.

CONCLUSIONS

From these boiling experiments at saturated and subcooled liquid conditions performed at small heaters under microgravity and earth gravity the following conclusions can be obtained.

- The boiling process seemed to be almost independent of the system acceleration, respectively the gravity level. This fact is consistent with earlier microgravity experiment.
- The gravity based buoyancy is deemed as a parameter of the boiling system with only small influence in the nucleate boiling region.
- Interfacial tension, capillary forces momentum of vapor generation, wetting behavior between solid surfaces and liquid and vapor, and in subcooled fluid states the thermocapillary jet are considered as the main mechanisms in the nucleate boiling regime.
- For the first time in boiling study the thermocapillary jet mode was observed for moderate subcooling states and the flow pattern could be studied by the utilization of differential interferometry and particle image velocimetry.
- Even under microgravity boiling is a very efficient process of heat transfer. Moreover the boiling process is self-stabilizing, since a strong increase in the heat flux only leads to a moderate increase of the wall temperature, as long as the boiling process is maintained in the nucleate boiling regime. Therefore the boiling process would allow a very fail-safe application for direct immersing cooling of high powered electronic microelements in all space systems. For these kind of applications the liquid conditions like fluid temperature and pressure level can easily be adapted.
- The final evaluation should allow more detailed statements of the boiling process, since during the mission a wide variety of fluid states with five different geometries could be studied.

This report describes only a few preliminary results from the LMS mission. The evaluation of the data is still going on. Detailed qualitative and quantitative correlations, which combine measured heat-flux, wall temperature and fluid state with the observed bubbles sizes and flow-patterns, will be generated.

FUTURE PLANS

The experimental work will be continued under earth gravity. The same hardware and refrigerant, which were used during the mission will be utilized for continued laboratory experiments, where the influence of the heater surface orientation in respect to the vector of the system acceleration on the boiling process will be investigated and finally compared with the results from the LMS mission.

NOMENCLATURE

a	acceleration
g	earth gravity
p	pressure
\dot{Q}	heat flux
r	radius
R	thermal resistance
T	temperature

Greek Symbols

α	heat transfer coefficient
λ	thermal conductivity
σ	surface tension
μg	microgravity

Subscripts

g	glass
i	center (inner core)
l	liquid
sat	saturation
sub	subcooled
w	wall
α	heat transfer
λ	heat conduction

LITERATURE

- /1/ Johannes Straub, Gerold Picker, Marcus Steinbichler, Josef Winter and Martin Zell; *Heat Transfer and Various Modes Of Bubble Dynamics On A Small Hemispherical Heater Under Microgravity and 1g Condition; Eurotherm Seminar No. 48, Ed. D.Gorenflo, D.B.R. Kenning, Ch. Marvillet, 1996, pp. 265-275*
- /2/ Johannes Straub; Gerold Picker; Martin Zell; *Study of Vapor Bubble Growth in supersaturated liquid; Proc. 30th Nat. Heat Conf. 1995 Portland USA, Vol. 3, pp. 29-37, Eds.: S.S. Sadhal et al*
- /3/ Kazuyoshi Fushinobu, Takao Nagasaki, Tadashi Saitoh, Atsushi Ui and Kunio Hijikata; *Boiling Heat Transfer Characteristics from very small heaters on a substrate; Heat Transfer 1994 Proc of the 10th Int. Heat Conf. Brighton U.K., Vol. 5, pp. 51-56, Ed. by J. Hewitt*
- /4/ Baker, E.; *Liquid Immersion Cooling of Small Electronic Devices; Microelectronics and Reliability, 1973, Vol. 12, pp. 163-173*
- /5/ Bar-Cohen, A.; *Fundamentals of Nucleate Pool Boiling of Highly-Wetting Dielectric Liquids; ASI Proceedings, Cooling of Electronic Systems, Izmir, Turkey, 1993, pp. 415-455, Ed. by S. Kakac*
- /6/ Bergles, A. E. & Bar-Cohen, A.; *Immersion Cooling of Digital Computers; ASI Proceedings, Cooling of Electronic Systems, Izmir, Turkey, 1993, pp. 539-621, Ed. by S. Kakac*
- /7/ Nagasaki, T., Hijikata, K., Fushinobu, K., & Saitoh, T.; *Boiling Heat Transfer from a Small Heating Element; 3, ASME Winter Annual Meeting, New Orleans*

- /8/ Straub, J., Zell, M., and Vogel, B.; *Pool Boiling in a Reduced Gravity Field*; Proc. Ninth Int. Heat Transfer Conf., Jerusalem, Israel, 1990, Ed. G. Hetsrony, Vol. 1, pp. 91-112, Hemisphere, New York 1990
- /9/ Forster, H. K., Zuber, N.; *Dynamics of Vapor Bubbles and Boiling Heat Transfer*; AICHE J., vol. 1, 1955, pp. 531 - 534
- /10/ Rohsenow, W. H.; *A Method of Correlating Heat Transfer Data for Surface Boiling of Liquids*; Trans. ASME Ser. C, J. Heat Transfer 74, pp. 969-976
- /11/ Straub, J.; *The Role of Surface Tension for Two-Phase Heat and Mass Transfer in the Absence of Gravity*; Experimental Thermal and Fluid Science 1994, 9, pp. 253-273
- /12/ Bakrhu, N., Lienhard, J. H.; *Boiling from small cylinders*; Int. J. Heat Mass Transfer 1972, vol. 5, pp. 2011-2025
- /13/ Johannes Straub, Stefan Micko; *Boiling On A Wire Under Microgravity Conditions - First Results From A Space Experiment Performed In May 1996*; Eurotherm Seminar No. 48, Ed. D.Gorenflo, D.B.R. Kenning, Ch. Marvillet, 1996, pp. 275-282

ACKNOWLEDGMENT

We like to express our appreciation to all, who made this research possible. Especially we are grateful to the Space Shuttle crew of STS 78, NASA headquarters, the mission manager, the mission scientist and the team of NASA Operation Support Center in Huntsville, AL, to ESA and ESA/ESTEC for providing the BDPU facility and the test container, the individuals of the industrial companies designing and building the facility and the test container of Alenia, Laben, Ferrari and Dornier. Furthermore we thank all individuals and teams supporting us during the mission and we gratefully acknowledge the support of the Germany Space Agency DARA in the contract 50 WM 9566.

Boiling on a miniature heater - A simulation for cooling of small electronic devices under microgravity

During the boiling experiment on six small heaters of different geometry about 300 single experiment cycles were conducted at 9 different fluid temperatures, ranging from 30°C to 120°C. At each fluid temperature a variety of fluid pressures (saturated and subcooled) were investigated with each of the available heaters. Besides the study of boiling phenomena we investigated the nucleation on small heating elements with low heat fluxes. Especially the optical images, combined with the electronical data showed surprising effects, which were not observed ever before. The real time particle image velocity processing confirmed these effects. The boiling heat transfer presented in common literature of heat transfer, used for the design of heat exchangers, predicts a strong influence of gravity on the heat transfer process. In contrast to the present state of art our findings showed, that under microgravity the boiling heat transfer is still as efficient as under normal earth gravity. In contrast to the existing theory our findings show that the influence of earth gravity is less than predicted, and the heat transfer in a microgravity environment is still as efficient, sometime seven more efficient than in the environment at normal gravity. A possible reason for this could be the strong stream flow which develops at certain fluid states around the heating elements. It was the first time that this strong stream flow could be observed and studied as functions of liquid parameters and heat fluxes. This stream flow causes a strong pumping effect without any mechanical parts carrying away the heat produced by our heating elements. Generally it can be stated, that these new results could lead to new theories, which describe the boiling process more accurately than existing theories, and will provide a further advance in the calculation and design of heat exchangers for application on earth and in space.

Bubble, Drop and Particle Unit (BDPU)

**Thermocapillary Migration and Interactions of Bubbles and
Drops**

Principal Investigator:

Dr. Shankar Subramanian
Clarkson University
Potsdam, New York

Thermocapillary Migration and Interactions of Bubbles and Drops

Principal Investigator: R. Shankar Subramanian, Clarkson University, U.S.A.
Co-Investigators: R. Balasubramaniam, NASA Lewis Research Center and
Günter Wozniak, Bergakademie Freiberg, Germany
Team Member: Peer H. Hadland, Clarkson University, U.S.A.

Summary

Experiments were performed aboard the LMS mission of the Space Shuttle in summer 1996 in the BDPU on isolated air bubbles and Fluorinert FC-75 drops as well as on interacting bubbles/drops migrating in a temperature gradient in a Dow-Corning DC-200 series silicone oil of nominal viscosity 10 centistokes. The data, recorded in the form of videotape images as well as cine images in selected runs, have been analyzed. Preliminary results are reported here. The behavior of the isolated objects is consistent with earlier observations made aboard the IML-2 mission while the range of Reynolds and Marangoni numbers has been extended substantially over that in the IML-2 experiments. Results on interacting drops and bubbles display interesting and unanticipated features. In some experiments, drops are found to follow a sinuous three-dimensional trajectory. In others, trailing drops and bubbles are found to move off the axis of the cell when migrating behind a leading drop or bubble which moves along the axis. In this type of run, if the trailing drop is sufficiently large, it is found to pass the leading drop. It is conjectured that this behavior of the trailing objects is influenced by the thermal wake behind the leading object. Also, since Fluorinert dissolves in silicone oil to some extent it is possible that the composition wake left by a drop, which takes a long time to dissipate, influences the motion of drops that are injected subsequently. Finally, behavior similar to that observed in IML-2, namely that a small leading drop slows the movement of a larger trailing drop moving along the cell axis, was observed as well.

1. Objectives

The objectives of this flight experiment were to conduct a detailed exploration of interactions between pairs of bubbles and pairs of drops, to determine velocity distributions by the use of tracer particles in the case of bubble motion, and finally to explore the motion of isolated bubbles and drops for parameter values beyond those which could be reached in prior IML-2 experiments.

2. Background

When a drop or bubble is introduced into a second fluid in which there exists a temperature gradient, the drop (or bubble is implied from hereon) will move (1). Such motion is a consequence of the variation of the interfacial tension along the interface

between the drop and the continuous phase. Reviews of the literature on this subject may be found in Wozniak *et al.* (2) and Subramanian (3). This movement is termed thermocapillary migration, and can be important in materials processing in space, and in separation processes used in long duration space excursions for recycling and on the surface of the moon.

The speed at which a drop migrates can be obtained by solving the governing continuity, Navier-Stokes, and energy equations along with the associated boundary conditions. When convective transport effects are important, the problems are nonlinear. The relative importance of convective transport of energy when compared to conduction can be judged from the magnitude of the Péclet number whereas a similar ratio for momentum transport is described by the Reynolds number, Re . When a velocity scale characteristic of thermocapillary migration is used, the Péclet number is known as the Marangoni number, Ma . The Capillary number also is another parameter that influences the shape of the drop. However, shape deformations were difficult to detect from the video and cine images from the LMS experiments. The definitions of the Reynolds and Marangoni numbers are given below.

$$Re = \frac{Rv_0}{\nu} \quad (1)$$

$$Ma = \frac{Rv_0}{\kappa} \quad (2)$$

Here, R is the radius of the drop, ν the kinematic viscosity of the continuous phase, and κ its thermal diffusivity. The reference velocity, v_0 , is defined below.

$$v_0 = \frac{|\sigma_T||\nabla T_\infty|R}{\mu} \quad (3)$$

In the above, μ is the dynamic viscosity of the continuous phase, σ_T is the rate of change of interfacial tension with temperature, and ∇T_∞ is the temperature gradient imposed in the continuous phase fluid.

In the linear limit when the Reynolds and Marangoni numbers are negligible, the contribution of thermocapillarity can be extracted from experiments on the ground. Therefore, experiments designed to explore thermocapillary migration on the ground are subject to this important limitation; some of this experimental work is discussed in references (2,3).

To better explore the parameter space in the Reynolds and Marangoni numbers than is possible on the ground, investigators have attempted to carry out experiments in reduced gravity conditions. The previous studies, as discussed by us in Balasubramanian *et al.* (4), were subject to many limitations which raise questions regarding the utility of the data. Therefore, in summer 1994, we performed thermocapillary migration experiments in reduced gravity under conditions closer to those assumed in theoretical models. We used air bubbles and Fluorinert FC-75 drops migrating in a Dow-Corning DC-200 series silicone oil of nominal viscosity 50

centistokes. The apparatus in which the experiments were performed was the Bubble, Drop, and Particle Unit (BDPU) built under the auspices of the European Space Agency. Our experiments, carried out aboard the IML-2 mission of the Space Shuttle, yielded good data on isolated drops up to a Reynolds number of 0.85 and a Marangoni number of 280, and on isolated bubbles up to a Reynolds number of 2.2 and a Marangoni number of 810. In the case of air bubbles, the data were found to be generally consistent with our predictions from a numerical solution of the governing equations as well as an asymptotic theoretical result obtained by Balasubramaniam and Subramanian (5). Also, we were able to perform preliminary experiments on pairs of drops injected one after the other along the long axis of the test cell. These drops migrated along the axis, and we made the remarkable observation that a relatively small leading drop can significantly slow down a larger trailing drop while itself moving as though it is unaffected by the large drop. We hypothesized that this was a consequence of the thermal wake behind the leading drop which is a region of weakened temperature gradient. The fluid in the wake will wrap around the trailing drop and can cause the driving force for the motion, which is the temperature variation over its surface, to be reduced.

In an attempt to explore further the interactions between pairs of drops and pairs of bubbles and to extend the range of values of Marangoni and Reynolds numbers, we performed follow-on flight experiments aboard the LMS mission of the Space Shuttle in summer 1996. The same fluids, air and Fluorinert FC-75, were used for the bubble and drop phases, respectively, and a silicone oil of nominal viscosity 10 centistokes was employed for the continuous phase. This choice was made so as to be able to extend the maximum Marangoni number by approximately a factor of 5, and the corresponding maximum Reynolds number by a factor of approximately 25. Also, tracer particles dispersed in the silicone oil were used in the air bubble migration experiments in order to track the flow in the continuous phase during the migration process. In addition, the Point Diffraction Interferometry (PDI) system used in IML-2 was refined by the European Space Agency to incorporate a Wollaston Prism with a divergence angle of 10 degrees, so that interferometry was able to provide quantitative information on temperature fields in the LMS experiments involving gentle temperature gradients. Except for these modifications, the procedures and the experiments were similar to those in IML-2, described in the final report for that flight experiment (6). A secondary objective of the LMS experiments was to gather data at small values of the Marangoni number; the IML-2 data on air bubbles showed significant departure from theoretical predictions in the range 5-40. However, this proved difficult to accomplish because of the reduced viscosity of the liquid and poor communication conditions with the Shuttle (resulting in frequent loss of Real Time TV coverage and commanding capabilities) during the low temperature gradient run in which this objective was to have been accomplished.

3. Methods of Data Acquisition and Analysis

The experiments were performed in the BDPU which was provided by the European Space Agency through a cooperative arrangement with the National Aeronautics and Space Administration. The apparatus consists of a "facility" which provided power, optical diagnostics and illumination, imaging facilities including a

video camera and a motion picture camera, and other sundry support services. Within this facility, a test cell that was specific to the experiment was inserted by the payload specialist on the Shuttle when needed.

Conceptually, the experiments were simple. Within a test cell mounted in the facility and filled with a suitable liquid, a temperature gradient was established, followed by the introduction of a bubble or a drop as desired. The subsequent motion of the object, in the direction of the applied temperature gradient, was recorded for later analysis on videotape on the ground as well as on cine film on board the Shuttle in selected experiments. When a bubble or drop reached the hot wall, it was extracted and another was introduced after a small waiting period.

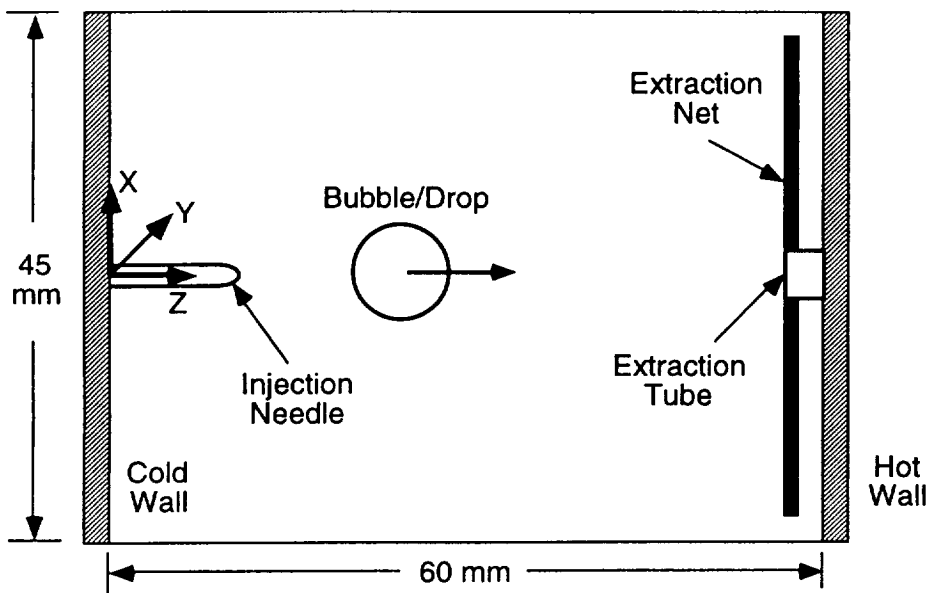


Figure 1. Schematic of Test Cell

The heart of the experimental apparatus is the test cell shown schematically in Figure 1. Two rectangular test cells were available. Both were of identical dimensions, measuring 60 x 45 x 45 mm in the interior. This cavity was filled with a Dow-Corning DC-200 series silicone oil of nominal viscosity 10 centistokes in both cells. As mentioned earlier, the silicone oil in the bubble cell contained a small concentration of tracer particles provided by Dornier GmbH from Germany. It was possible to maintain the two end walls (made of aluminum) in the long dimension of the cell at fixed known temperatures so that a temperature gradient could be established in the z-direction. Within the cavity, an injection needle was available when needed. When not in use, the tip was flush with the cold aluminum surface at its center. It was possible to introduce air bubbles in one test cell, and Fluorinert FC-75 drops in the other cell. The diameters of the bubbles varied from approximately 1.3 to 14.4 mm, and those of drops ranged from 2.1 to 14.3 mm. After a bubble or drop completed its traverse, it was possible to extract it from the hot wall using an extraction tube mounted at the center of a net.

The equipment provided red background illumination and the opportunity to capture images of the interior of the test cell on videotape on the ground. Also, a limited amount of cine film was available, and was used to capture images during selected runs at suitable framing rates.

In any given run, the procedure was first to establish the desired temperature gradient over a period of 2 hours. This period included approximately 30 minutes in which the liquid in the cell was stirred by back and forth movement of the net, followed by a quiescent period lasting approximately 90 minutes. This was followed by the injection, traverse, and subsequent extraction of bubbles or drops. At low temperature gradients, interferometry images received on the ground were used as a diagnostic tool to determine when the temperature field became steady.

At the end of the heating period, when real time TV and commanding capability were available, the experiment was initiated by sending a command to inject a bubble or drop of a specified size at a specified position along the long axis of the cell. The traverse of the object was followed on the ground while recording it. When the bubble reached the opposite wall, it was usually extracted using a small tube at the center of that wall. After the passage of a sufficient amount of time, judged from interferometry images where available, the next injection was initiated. This waiting period was usually of the order of 3 minutes. For a pair of bubbles or a pair of drops, suitable commands were packaged and sent up to the apparatus to perform the sequential double injection automatically. When a sufficient number of runs were made with one temperature gradient, another gradient was employed. The bubble cell and the drop cell were each used twice. Temperature gradients of 0.33 and 1 K/mm were used with bubbles, and 0.25 and 1 K/mm with the drops. A run with a temperature gradient of 0.067 K/mm with the bubble cell yielded no usable data due to poor communications between the orbiter and ground caused by the "safe" attitude of the orbiter.

A total of 64 bubble runs and 74 drop runs were recorded on videotape, and 35 bubble runs and 38 drop runs on cine film. Of these, 53 bubble runs and 67 drop runs were analyzed. The rest either contained objects too small to be measured precisely or presented other problems that precluded analysis. A sufficient number of runs were made on isolated drops and bubbles to extend the range of Reynolds and Marangoni numbers beyond those encountered in the IML-2 experiments. The remaining experiments focused on interacting drops and bubbles. While we introduced pairs of bubbles and pairs of drops deliberately in selected runs, sometimes a collection of two or more objects was introduced by the injection system even when the objective was to inject a single object.

4. Results and Discussion

4.1 Isolated Bubbles and Drops

One of the objectives in performing experiments on isolated drops and bubbles was to look for shape deformation. Deformation would be most likely to occur in the case of large bubbles and drops which moved very rapidly. The video and cine images

were analyzed using an automated computerized system developed by NASA Lewis Research Center. This worked by selecting single frames and tracking the boundary of the object involved. For rapidly moving objects, the image on a single frame was sufficiently blurred in the direction of motion that any deformation could not be measured due to the uncertainty in the measurement of the diameter in that direction. In cases where both diameters could be measured precisely, they were found to be equal to each other to within the uncertainty of the measurement.

Since the position of the objects was followed throughout the traverse it was possible to calculate the velocity at various locations in the cell. The velocity changed during the traverse because of the initial acceleration of the bubble or drop upon release from the injector as well as due to the change of physical properties (principally viscosity) with temperature. Therefore, the velocity was never truly steady for any given bubble or drop. In the case of bubbles, a quasi-steady velocity can be expected to be achieved after the bubble has moved a distance equal to its own diameter. We selected data near the center of the cell as being the best to present. In the case of drops, a quasi-steady state would be achieved only when a quasi-steady temperature gradient field is established within the drop. This restriction resulted in obtaining quasi-steady velocities of drops only up to approximately 6 mm in diameter. In the case of larger drops, the data must be considered transient throughout the run. For a drop of diameter 6 mm, it was necessary to obtain data a bit beyond the center of the cell in order to assure that a quasi-steady had been reached. In the isolated bubble runs, the Reynolds number varied from 0.8 to 87 while the corresponding Marangoni number ranged from 51 to 5800. In the case of the drops, the range of Reynolds number was 0.14 to approximately 10 and the corresponding range of Marangoni number was 14.6 to approximately 600.

In Figure 2, the velocity data on isolated air bubbles are plotted in scaled form and compared with available predictions. The velocity of a bubble is scaled using the velocity it would have in the limit of negligible values of the Reynolds number and the Marangoni number given in reference (1). The various physical properties are evaluated at the estimated temperature in the undisturbed fluid at the x-y plane containing the center of the bubble. Typical uncertainty estimates are shown in the figure. Also shown on the same drawing are data from IML-2 experiments. Note that the data are consistent with those obtained during the IML-2 mission while covering a wider range of values of the Marangoni number. Included in the drawing for comparison is a theoretical prediction obtained from a finite difference solution of the governing continuity, momentum, and energy equations for the quasi-steady velocity and temperature fields and bubble velocity (7). The model also assumes a spherical bubble in an infinite extent of fluid, and Newtonian and incompressible flow with constant physical properties, except for the interfacial tension which is assumed linear with temperature. Also included is our prediction in the asymptotic limit of large Marangoni number for negligible Reynolds number. It is evident from Figure 2 that the data support the qualitative trend predicted from the quasi-steady theory.

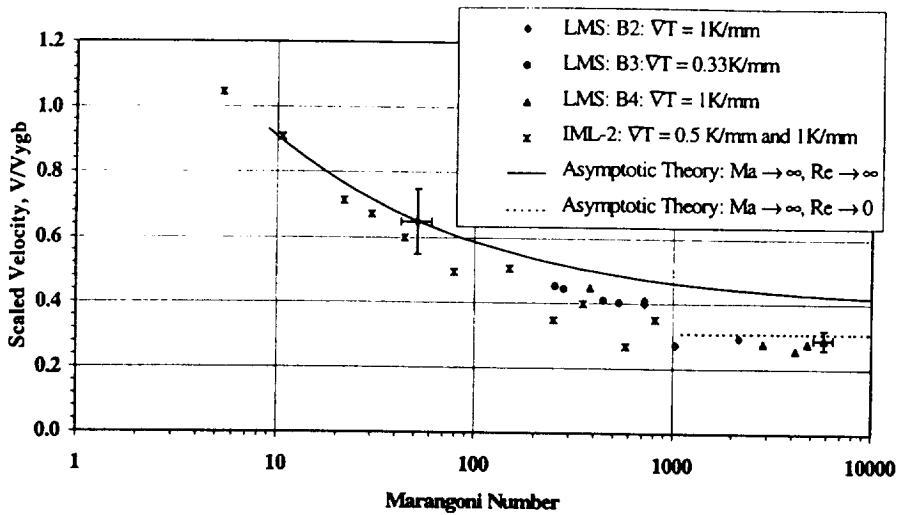


Figure 2. Scaled velocity of isolated bubbles plotted against the Marangoni number and compared with IML-2 data and results from two asymptotic theoretical predictions for large values of the Marangoni number. The reference velocity used for scaling is the value expected when convective transport effects are negligible.

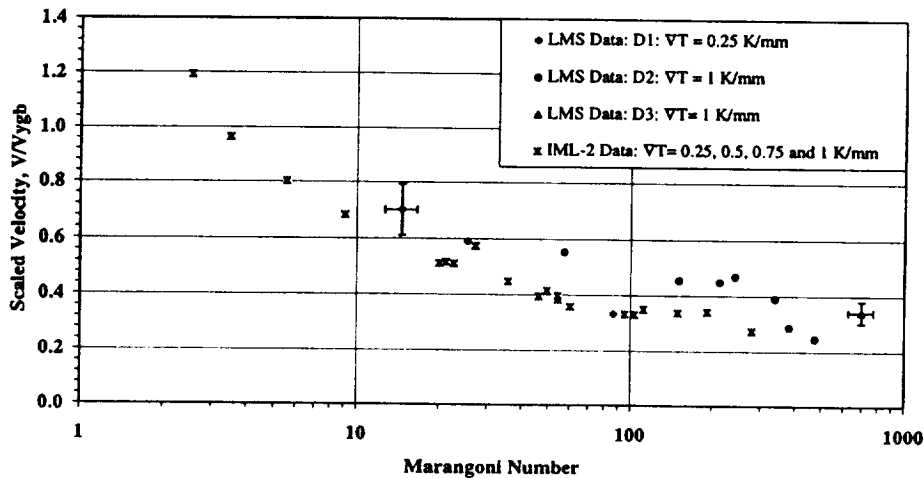


Figure 3. Scaled velocity of isolated drops plotted against the Marangoni number and compared with IML-2 data. The reference velocity used for scaling is the value expected when convective transport effects are negligible.

In Figure 3, we show a drawing similar to Figure 2, but for Fluorinert FC-75 drops. These data display a trend very similar to that shown by bubbles in Figure 2. The reference velocity is once again the predicted velocity at negligible values of Reynolds and Marangoni number from reference (1). Again, the IML-2 data are included for comparison purposes. At present, no theoretical predictions are available for comparison with these data.

4.2 Interacting Drops and Bubbles

One of the principal objectives of the LMS experiments was to explore interactions between pairs of bubbles and pairs of drops. Therefore, several runs were made in which such pairs were deliberately introduced. When a small bubble follows a large bubble, the leading large bubble moves away so rapidly that it is not possible to observe any significant interaction effects between the two objects; the same holds true for drops. Therefore, virtually all the usable interaction runs were of the type where a small leading drop/bubble was followed by a larger object.

While we indeed observed behavior similar to that in IML-2 experiments on pairs of drops as mentioned earlier, we shall focus here on some remarkable new observations. First, in several experiments we observed a leading bubble or drop moving straight along the axis of the cell while a trailing object released a small distance behind the leader moved away from the axis in the positive or negative x-direction in Figure 1. This movement was typically only by a few mm in that direction but was clearly measurable. We observed the same behavior on the part of bubbles as well as drops. In some other experiments on Fluorinert drops we found even more interesting behavior. In the very first drop run, when we attempted to inject a single drop, four drops were introduced instead by the injector. The first of these moved straight along the axis of the cell, deviating from that axis only by about 0.5 mm by the time it reached the hot wall. However, the second drop was found to execute a three dimensional trajectory which may be described as sinuous for lack of a better term. The movement of this object was principally in the direction of the applied temperature gradient. However, it was evident from the video image that the object moved back and forth in the x-direction as it moved along the z-axis. In addition, the interferometry view of this run revealed the object also moved back and forth in the y-direction in the same manner. However, this motion in the y-direction began initially in phase with that in the x-direction, but after about two oscillations, fell out of phase so that the trajectory can be visualized as evolving into a helix. The third object also began its movement in a manner similar to that of the second object, but its oscillations were larger in amplitude. The fourth drop was very small and exhibited somewhat similar behavior.

The above fascinating behavior on the part of interacting drops was not confined to the first run. With the same temperature gradient, we observed four experiments in which the pattern was observed. In two of these runs, even the leading drop exhibited sinuous motion.

Explaining the behavior of interacting drops is not trivial. Clearly the wake of the first object must play an important role in causing it. One can envision a thermal wake behind the leading object in the case of both the bubble and drop experiments.

This is a relatively thin region in which the temperature field is presumably axisymmetric and the temperature gradient is weaker than that in the undisturbed fluid. Whereas in IML-2, the trailing drop moved straight along the axis when influenced by this wake, in some LMS experiments, it appears that slight asymmetries in the positioning of the second object with respect to the wake caused the fluid in the wake to wrap around this object asymmetrically; in turn, this must have led to an asymmetry in the temperature gradient distribution on its surface which must have caused the resulting movement away from the axis of the cell. The more interesting sinuous behavior is also more difficult to explain because it involves a somewhat periodic return of the object to the axis and movement past the axis in the other direction. Since this was only observed in the drop runs, it also is possible that the dissolved Fluorinert FC-75 in the silicone oil is playing some role. If one assumes thermodynamic equilibrium corresponding to the prevailing temperature at each location on the drop surface, then dissolved FC-75 should not make any difference to the interfacial tension gradient on the drop surface and one must look beyond this for explanations. Another important difference is that thermal diffusion is much more rapid than species diffusion in the silicone oil; one can expect a difference of two orders of magnitude between the two diffusivities. This suggests that thermal wakes would dissipate relatively quickly and composition wakes would take much longer to do so. Since the sinuous paths were indeed noted even with a leading object in a run wherein there was a long wait after the previous run, thermal wakes are less likely to be the reason for the occurrence of these trajectories.

4.3 Diagnostics

In runs involving gentle temperature gradients, interferometry images using the PDI system with a Wollaston Prism were successfully received on the ground and recorded on videotape. The PDI system failed to provide any useful information in runs at the higher gradients. Also, in the drop experiments, the very first drop left a trail of dissolved Fluorinert FC-75 in its wake. The numerous fringes due to the refractive index gradients resulting from the composition variations made the interpretation of later interferometry images from the drop cell for temperature field information not possible. The best bubble run for interferometry was analyzed by G. Wozniak and his students at Bergakademie Freiberg and the resulting temperature field was found to be qualitatively consistent with that one would expect. Quantitative comparisons still need to be performed when predictions are made for this run. The best drop run was that involving the very first drop. Even this run shows problems in the interpretation behind the drop due to the wake of dissolved Fluorinert. However, in the forward portion of the domain in the direction of movement of the drop, the field is qualitatively as expected.

In some selected runs, tracer particles were illuminated using a laser light sheet and their movements recorded on videotape. These images need to be analyzed using an automatic system at NASA Lewis Research Center. We intend to perform this analysis as soon as proper training is received in the use of the analysis system.

5. Conclusions and Future Plans

This is a preliminary report based on observations made on isolated and interacting bubbles and drops moving in a temperature gradient under reduced gravity conditions in the LMS mission. The results for the migration velocity of isolated air bubbles qualitatively extend the range of values of the Marangoni number investigated in earlier IML-2 flight experiments. The data are consistent with those from IML-2 and with theoretical predictions. The data on isolated drops display similar trends even though theoretical predictions are not yet available for comparison. Experiments on multiple drops and bubbles show evidence of wake effects from a leading object. In some cases, the trailing bubble or drop moves off the axis of the cell; large trailing drops pass the leading drop in this way. In other experiments, trailing drops exhibit a sinuous three-dimensional trajectory. It is conjectured that these types of behavior, which imply non-axisymmetric fields, may be caused by a combination of factors arising from the thermal and compositional wakes from the leading drop working in conjunction with slight asymmetries. The data on runs involving tracer particles remain to be analyzed using the automatic analysis system at NASA Lewis Research Center.

6. Acknowledgments

The work described herein was supported by NASA's Microgravity Sciences and Application Division through NASA Grant NAG3-1122 from the Lewis Research Center to Clarkson University. Also, support by the German Space Agency (DARA) through DARA Grant 50WM9582-0 to G. Wozniak is gratefully acknowledged.

7. Bibliographic Citations of Articles/Presentations Resulting from the Flight

Articles in preparation

"Thermocapillary Migration of Isolated Bubbles and Drops at Relatively High Marangoni number in Reduced Gravity," by P.H. Hadland, R. Balasubramaniam, G. Wozniak, and R.S. Subramanian.

"Interactions among Drops and among Bubbles Undergoing Thermocapillary Migration," by R. Balasubramaniam, P.H. Hadland, G. Wozniak, and R.S. Subramanian.

"Temperature and Flow Fields around Bubbles Executing Thermocapillary Motion," by G. Wozniak, R. Balasubramaniam, P.H. Hadland, and R.S. Subramanian.

Presentation

"Thermocapillary Migration of Drops and Bubbles in Reduced Gravity – Preliminary Results from LMS Flight Experiments," P.H. Hadland, R. Balasubramaniam, G. Wozniak, and R.S. Subramanian, Poster Presentation at the Gordon Conference on Gravitational Effects in Physicochemical Systems, Henniker, NH, June 1997.

8. References Cited

1. N. O. Young, J. S. Goldstein, and M. J. Block: The motion of bubbles in a vertical temperature gradient, *J. Fluid Mech.*, Vol. 6, 1959, pp. 350-356.
2. G. Wozniak, J. Siekmann, and J. Srulijes: Thermocapillary Bubble and Drop Dynamics Under Reduced Gravity --- Survey and Prospects, *Z. Flugwiss. Weltraumforsch.*, Vol. 12, 1988, pp. 137-144.
3. R. S. Subramanian: The Motion of Bubbles and Drops in Reduced Gravity, in *Transport Processes in Bubbles, Drops, and Particles*, edited by R. Chhabra and D. De Kee, Hemisphere, New York, 1992, pp. 1-41.
4. R. Balasubramaniam, C.E. Lacy, G. Wozniak, and R.S. Subramanian: Thermocapillary Migration of Bubbles and Drops at Moderate Values of the Marangoni Number in Reduced Gravity, *Phys. Fluids*, Vol 8, No. 4, 1996, pp. 872-880.
5. R. Balasubramaniam and R.S. Subramanian: "Thermocapillary Bubble Migration -- Thermal Boundary Layers for Large Marangoni Numbers," *Int. J. Multiphase Flow*, Vol. 22, 1996, pp. 593-612.
6. R. S. Subramanian, R. Balasubramaniam, C.E. Lacy, and G. Wozniak: "IML-2 Final Science Report on Thermocapillary Migration and Interactions of Bubbles and Drops."
7. R. Balasubramaniam and J. E. Lavery: Numerical Simulation of Thermocapillary Bubble Migration Under Microgravity for Large Reynolds and Marangoni Numbers, *Num. Heat Transfer A*, Vol. 16, 1989, pp. 175-187.

Thermocapillary Migration and Interactions of Bubbles and Drops

Principal Investigator: R. Shankar Subramanian, Clarkson University, U.S.A.

Co-Investigators: R. Balasubramaniam, NASA Lewis Research Center and
Günter Wozniak, Bergakademie Freiberg, Germany

Team Member: Peer H. Hadland, Clarkson University, U.S.A.

Brief non-Technical Summary

Drops and bubbles will be encountered in various materials processing applications in reduced gravity as well as in the recycling of life-sustaining substances such as water and oxygen in long-duration space excursions. On the Earth, drops and bubbles move due to the action of gravity. In reduced gravity, other mechanisms will be developed for moving these objects when needed. For instance a temperature gradient can be used to move a drop. The variation of temperature around the periphery of the drop causes gradients of interfacial tension which act to move the fluid around the drop and by reaction the drop migrates typically toward warm fluid. This is known as thermocapillary motion.

Experiments were performed aboard the LMS mission of the Space Shuttle in summer 1996 in the BDPU on air bubbles and Fluorinert FC-75 drops migrating in a temperature gradient in a Dow-Corning DC-200 series silicone oil. The movement was recorded on videotape and cine film and analyzed frame-by-frame later on the ground. Also, interferometry images were recorded on video and analyzed for the temperature distribution around the moving bubbles. The results on the motion of single bubbles or drops are consistent with those from our earlier experiments on the IML-2 mission in summer 1994 and permit us to extend the range of the relevant parameters. These results also are in general agreement with available theoretical predictions. In the case of interacting bubbles or drops, we observed very interesting physical behavior which was not seen in our earlier flight experiments. It was found that a bubble will sometimes move away from the axis of the cell when trailing a small leading bubble. If it is sufficiently large, it will pass the leading bubble. The same behavior was observed in the case of drops. In addition, we found in some experiments that drops followed a three-dimensional trajectory which resembles a helix. These phenomena appear to be due to complex effects arising from the thermal and compositional wakes left by the leading object, and we are working on developing a good physical understanding of the observed behavior.

Bubble, Drop and Particle Unit (BDPU)

Nonlinear Surface Tension Driven Bubble Migration

Principal Investigator:

Dr. Antonio Viviani
Seconda Università di Napoli
Naples, Italy

BDPU on LMS TC#6

Non Linear Surface Tension Driven Bubble Migration

P.I. : Antonio Viviani
Seconda Università di Napoli
Aversa, Italy

The experiment has been the follow-up of the "Bubble Behavior under Low Gravity" experiment performed during the IML2 mission in 1994 which was a milestone in the field of thermocapillary (or Marangoni) bubble migration, i.e. the motion of bubbles in a liquid subjected to a thermal gradient due to the dependence on the temperature of the surface tension at the liquid-bubble interface. In fact, for the very first time, it was shown the existence of liquids where thermocapillary migration of bubbles occurs from hot liquid towards the colder one, opposed to the classical Marangoni migration where bubbles move from colder liquid to the hot one.

In particular, it was demonstrated that in some saturated aqueous solutions of long chain alcohols (such as normal-heptanol used in the experiment), due to the particular dependence on the temperature of the surface tension at the interface with air, the bubbles can migrate from the "hot" side to the "cold" one, the latter being now the pole of minimum surface tension. This is very relevant to applications of space material sciences since that behavior of the interface tension with respect to the temperature is the same of the one shown, at very higher (1000-1500 °C) temperatures, by a wide class of materials of high technological interest.

The diagram of the surface tension versus the temperature of normal heptyl alcohol shows a parabolic behavior with a minimum around 40°C, in the case of thermodynamic equilibrium, that is, each point of the diagram is obtained by measuring the surface tension at the interface between the solution and air with the solution saturated at the given temperature (static surface tension measurement).

In the experimental configuration, with a linear temperature distribution imposed along the Test Cell, that means in dynamic condition, the most relevant result is that the position of minimum of the surface tension is not at 40°C; in fact, the bubbles injected did not stop in the corresponding position in the cell; they moved toward the coldest temperature, even though, their non-linear velocity of approach to the cold wall seems to slow down to rest at a temperature around 10°C. Being the operative temperatures of the cell in the range 10-90°C, the possible stop of the bubble around the temperature of 10°C could have been disturbed by the distortion in the thermal field that occur in the surrounding of the wall and/or of the extraction net of the cell.

The LMS experiment fully confirmed the findings of the IML2; moreover by putting the temperature of the cold wall to 5°C it has been detected the stopping of the bubble around 8-10° C. So it remains open the puzzling problem (as defined by Prof. Manuel G. Velarde) of explaining why the surface tension minimum location in presence of flow does change with respect to the static value.

A detailed analysis of all data collected during the mission is unfortunately still missing and will be reported at International Conferences. It is also planned to submit a paper on the results of both the experiments (IML2 and LMS) to the Physics of Fluids Journal.